Master Thesis, Department of Geosciences

Crustal structure of the Eggvin Bank, west of Jan Mayen

Data processing, velocity modeling and interpretation of recordings from a marine wide-angle seismic survey

Sigurd Eide

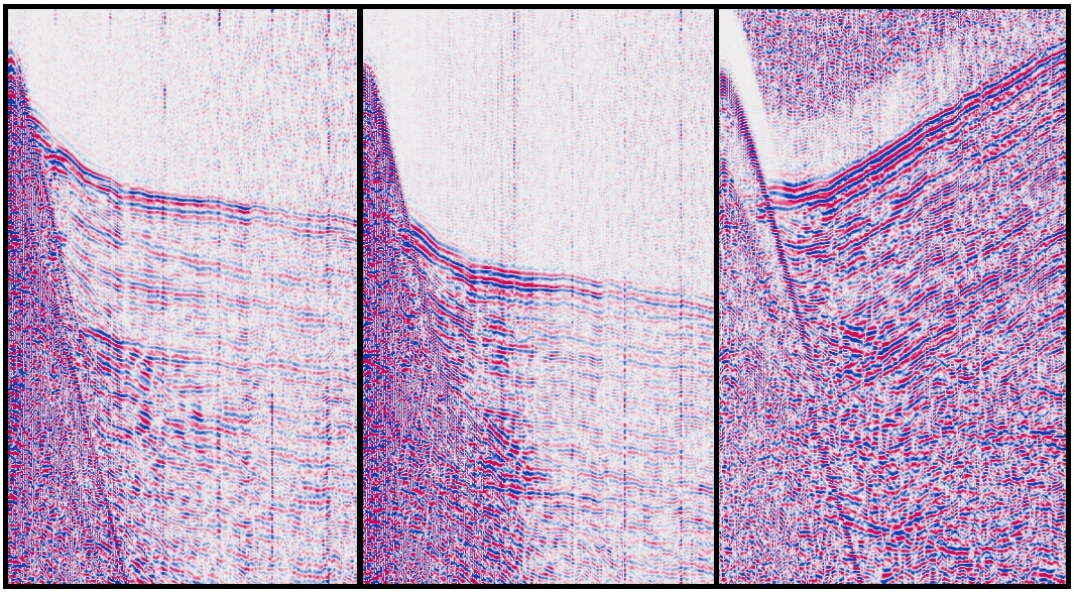

UNIVERSITY OF OSLO

FACULTY OF MATHEMATICS AND NATURAL SCIENCES

Crustal structure of the Eggvin Bank, west of Jan Mayen

Data processing, velocity modeling and interpretation of recordings from a marine wide-angle seismic survey

Sigurd Eide

Master Thesis in Geosciences

Discipline: Geophysics

Department of Geosciences

Faculty of Mathematics and Natural Sciences

University of Oslo

June, 2014

Supervisor: Asbjørn Breivk, Associate Professor at the Department of Geoscience, Faculty of Mathematics and Natural Science, University of Oslo.

This work is published digitally through DUO – Digitale Utgivelser ved UiO

http://www.duo.uio.no

It is also catalogued in BIBSYS (http://www.bibsys.no/english)

Acknowledgements

First of all, special thanks go to my supervisor Asbjørn Breivik for all the guidance I have received during this study. His scientific insight as well as support with the technical handcraft have been highly appreciated.

I would like to give credit to all participating institutions and everybody involved in the East Greenland 2011 Survey. Participating institutions were: University of Bergen, University of Oslo, University of Copenhagen, Hokkaido University and Institute of Marine Research (Norway). Especially would I like to thank the survey responsible for granting me permission to investigate the data sets.

Finally, I am very grateful for the good support I have got during the last 5 months. My appreciations goes out to my dear family, friends and fellow students at Blindern.

Sigurd Eide
May 30, 2014

Abstract

The Eggvin Bank is a shallow area located on the northern segment of Kolbeinsey Ridge. Its crustal structure was investigated along a 301 km long transect from the Greenland Basin to the Iceland Plateau, crossing over the Jan Mayen Fracture Zone and the Eggvin Bank. P- and S-wave velocities were obtained from forward and inverse modeling of three-component ocean bottom seismometer data.

Optimal results of modeling were obtained with a four layered model (I: Sediments. II-A: Upper crust. II-B: Middle crust. III: Lower crust) over a half-space (IV: Upper mantle). In Iceland Plateau and Eggvin Bank the sediments were estimated zero to 0.5 km thick with P-wave velocities between 1.8 and 2.3 km/s. Poisson's ratio in the sediments was estimated to be 0.39. Average P-wave velocities of the upper and middle crust, Layer II-A and II-B, were estimated to 3.45 - 4.60 km/s and 5.50 – 6.55 km/s, respectively. Poisson's ratios was estimated to be 0.35 for both layers. Relatively low P-wave velocity and high Poisson's ratio are ascribed to high porosity in extrusive and intrusive igneous rocks. Serpentinization is another possible cause. P-wave velocities in the lower crust, layer III, were estimated to 6.80 - 7.20 km/s, with a Poisson's ratio of 0.29. These velocities are typical for gabbros. Average upper mantle P-wave velocities were modeled to 7.83 km/s under the Eggvin Bank. Poisson's ratio was estimated to be 0.25, indicating normal preidotitic composition.

Iceland Plateau crust resembles structures to the south. The Eggvin Bank has a velocity profile similar to oceanic crust, in particularly as found in the Iceland Plateau. The velocity profile differs form continental crust in Jan Mayen Micro Continent as well as mapped structures beneath the Jan Mayen island. Eggvin Bank crustal thickness (8 – 11 km) is greater than average oceanic crust (7 km), as well as crust in the Iceland Plateau (9 km). Thicker crust locally underneath the major seamounts was interpreted to be directly related to their presence. In the center of the bank crustal thickness (8 – 9 km) compare with Iceland Plateau. Layer II-A and II-B are thicker in the Eggvin Bank compared to Iceland Plateau. This is interpreted to derive from extensive volcanic activity on the bank.

Crystalline structures in the Greenland Basin were poorly constrained because recordings could not be recovered from the deployed OBS in this part of the survey line. However, a substantial change in crustal thickness could be identified across the Jan Mayen Fracture Zone. Depth conversion estimated sediments to be 0.2 - 2.0 km thick in the Greenland Basin, and the crystalline thickness was modeled 4.0 $\pm$1.2 km. Fracture zone related serpentinization in upper mantle was not indicated by average P-wave velocity (8.0 km/s) and Poisson's ratio (0.25).

Contents

List of Figures

List of Tables

Part I

Introduction

Chapter 1

Objectives and Outline of Thesis

Geophysical surveying has contributed profoundly to present day knowledge about the oceanic crust. Through analysis and modeling of acquired data, structures within the deep unaccessible subsurface can be revealed. In 2011 a marine geophysical survey was conducted on the west side of Jan Mayen, targeting the anomalously shallow area of the Eggvin Bank. Geochemical studies have previously targeted the bank. Nevertheless, it is still a little studied frontier area. Acquisition was done along a line extending from the Greenland Basin in the NNE to the Iceland Plateau in the SSW, across the Jan Mayen Fracture Zone and the Eggvin Bank. The line was a part of the East Greenland 2011 Survey. It is the first modern investigation of its kind across the bank. Participating institutions were the University of Bergen, University of Oslo, University of Copenhagen and Hokkaido University. Wide-angle and reflection seismic were gathered during acquisition, as well as gravity and magnetic data. Wide-angle seismic was recorded with five three-component ocean bottom seismometers deployed on the sea floor. Reflection seismic was recorded with a single-channel streamer.

This study will evaluate the seismic data and the main objective is to present a two-dimensional velocity profile along the survey line, including distribution of both P- and S-wave velocities. Theory about signal processing, seismic wave propagation and modeling principles will be related to the results obtained at each step involved with construction of the model. The choice of model complexity is discussed with respect to seismic coverage and corresponding limitations of modeling. The thesis will document and evaluate how the model was constructed from the given amount of data, as well as assess the validity of the final results. The secondary objective is to relate the obtained velocity model to lithology, and compare the results with other crustal studies conducted nearby. Reflection seismic and regional geophysical data will also be evaluated and related to the model. A discussion will evaluate what the model can tell about the crustal structure of the Eggvin Bank, and how it relates to the geological development in the area.

This thesis is organized in four parts. Part I introduces the thesis and presents the investigated area and its tectonic setting. Part II covers the applied seismic data processing. Part III presents all steps involved with velocity modeling. Part IV presents the final crustal model and put the results in a geological context.

Chapter 2

The Eggvin Bank and its Surroundings

2.1 Area presentation

A bathymetric map over the investigated area is presented in Figure 2.1. The Eggvin Bank is located in the Greenland Sea, to the west of the Jan Mayen island and across the northern Kolbeinsey Ridge. It is an anomalous shallow feature on the seafloor, containing several submarine volcanic peaks. Seafloor depths increase to north and south of the bank, where they appear as normal for the Greenland Basin and the Iceland Plateau, respectively. The bank's northern boundary is the Jan Mayen Fracture Zone (JMFZ), which marks an abrupt change to the lithosphere of the Greenland Basin. The central part of the JMFZ is a transform on the mid Atlantic spreading ridge, connecting the Kolbeinsey Ridge to the west and the Mohns Ridge to the east. The lineament of the transform continues further to east and west as a fracture zone. On the south side the bank borders with the Iceland Plateau. The seafloor over the Iceland Plateau is shallower than in the Greenland Basin, At the other side of the JMFZ. The northernmost Kolbeinsey Ridge has an overlapping offset, referred to as the Eggvin Offset (latitude $\sim 71^0$N and longitude $\sim 14^0$W). The southern boundary of the Eggvin Bank is along a lineament perpendicular to this offset. On both sides of the Kolbeinsey Ridge shallow bathymetry extends within the southern and northern lineament, from about longitude 10^0 to 16^0W. An asymmetry is observed about the spreading axis.

The active volcanic island of Jan Mayen is located to the east of the bank. The island is created by the Beerenberg volcano, with its cone erected on the northern side of the island. To the north of JMFZ and opposite the island is the submarine Jan Mayen Plateau. It is a wide bank next to the southernmost segment of the Mohns Ridge. South of the Jan Mayen island lies the Jan Mayen Micro Continent (JMMC), a continental fragment that lies surrounded by oceanic crust (e.g., Eldholm and Talwani, 1982; Talwani and Eldholm, 1977). It consist of a ridge extending southwards with a basin lying on its western side, The Jan Mayen Ridge and the Jan Mayen Basin, respectively. The northern boundary of the micro continent is inferred to be the continuation of the northern lineament of the East JMFZ (Kandilarov et al., 2012). Ocean-continent transitions have been established on the east and west side (Breivik et al., 2012; Kodaira et al., 1998).

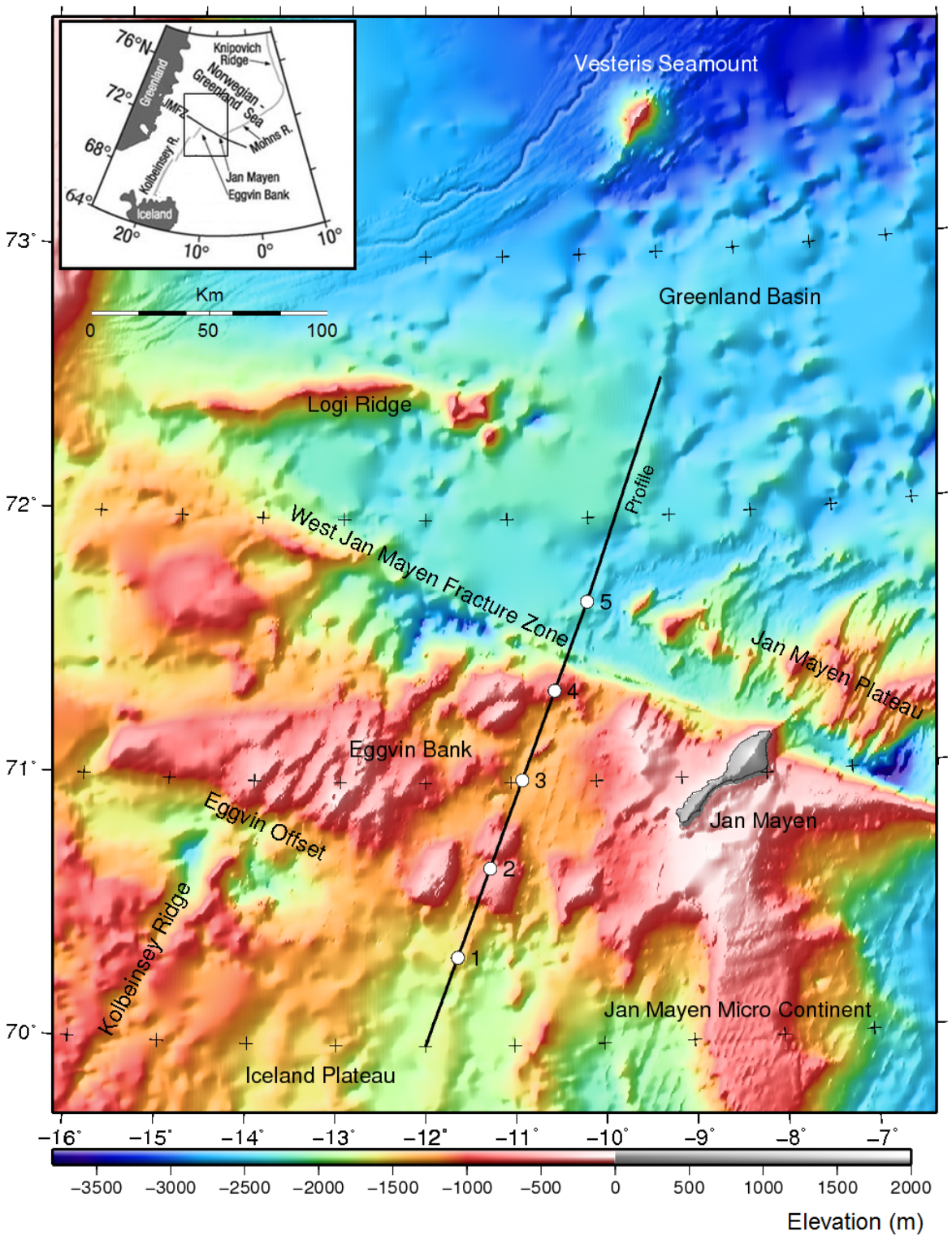

Figure 2.1: Bathymetric map over the Eggvin Bank. The map was generated with data from Jakobsson et al. (2012). Survey line and position of ocean bottom seismometers are indicated on the map. In the upper left corner a regional map indicates the area location in the Norwegian-Greenland Sea, modified from Mertz et al. (2004).

Northwest of the Eggvin bank lies the Logi Ridge, a narrow and possibly igneous ridge which extends for about 150 km in an east-west trend. An uplift of the seafloor is observed extending from the ridge's easternmost seamount. Further north, about 350 km north of the Eggvin Bank is the Vesteris Seamount. It is a single submarine volcanic peak on the seafloor (Cherkis et al., 1994; Haase and Devey, 1994).

2.2 Tectonic setting

There are two major tectonic events that describe the evolution in the North Atlantic. In Figure 2.2 a reconstruction of the plate motion is presented, displaying how the magnetic anomalies corresponds to the development. Figure 2.3 displays the geological time scale and an overview of the major events that took place. The first major event was the continental rifting between Norway and Greenland, and the subsequent breakup in Early Eocene. At magnetic anomaly 24 sea floor spreading had become established (e.g., Eldholm and Talwani, 1982; Talwani and Eldholm, 1977). This corresponds to about 55 Ma, according to the time scale of Cande and Kent (1995). During this period spreading also occurred in the Labrador Sea between North America and Greenland (e.g., Talwani and Eldholm, 1977; Tessensoh and Piepjohn, 2000). Continental separation between Norway and Greenland was accompanied by much magmatism which lead to thick oceanic crust along the North Atlantic margin (White and McKenzie, 1989). Sea floor spreading took place along Reykjanes, Aegir and Mohns Ridge until about 33 Ma, magnetic anomaly 13.

In early Oligocene the second major event took place when spreading in Labrador Sea ceased and a major change occurred in the relative plate motion between the Eurasian plate and Greenland (e.g., Gaina et al., 2009), changing from NW-SE to E-W. Spreading along the Aegir Ridge then gradually decreased until it completely stopped around 24 Ma, magnetic anomaly 7-6. JMMC was separated from Greenland (e.g., Eldholm and Talwani, 1982; Talwani and Eldholm, 1977) through passive non-volcanic rifting (Kodaira et al., 1998). At magnetic anomaly 5 the spreading was fully established along the Kolbeinsey Ridge (e.g., Gaina et al., 2009).

During the whole evolution of the North Atlantic the Mohns Ridge has been a spreading center. When shifting took place in early Oligocene, from Aegir to Kolbeinsey Ridge, the shift of spreading center created a new active transform. Between Aegir Ridge and Mohns Ridge the Eastern JMFZ was the active offset, while (Western) JMFZ is the active transform between the Kolbeinsey and the Mohns Ridge. Spreading rates generally slowed down from 2 cm/yr after initiation of sea-floor spreading in Early Eocene, to values around 0.5 cm/yr in Oligocene time (Mosar et al., 2002), Figure 2.4. Values are half spreading rates. A later increase to around 1 cm/yr coincided with the positioning of the Iceland Hotspot under the North Atlantic mid-ocean ridge, magnetic anomaly 6. Spreading along Mohns Ridge and Kolbeinsey Ridge continued at $\sim$1 cm/yr (e.g., Mosar et al., 2002; Gaina et al., 2009).

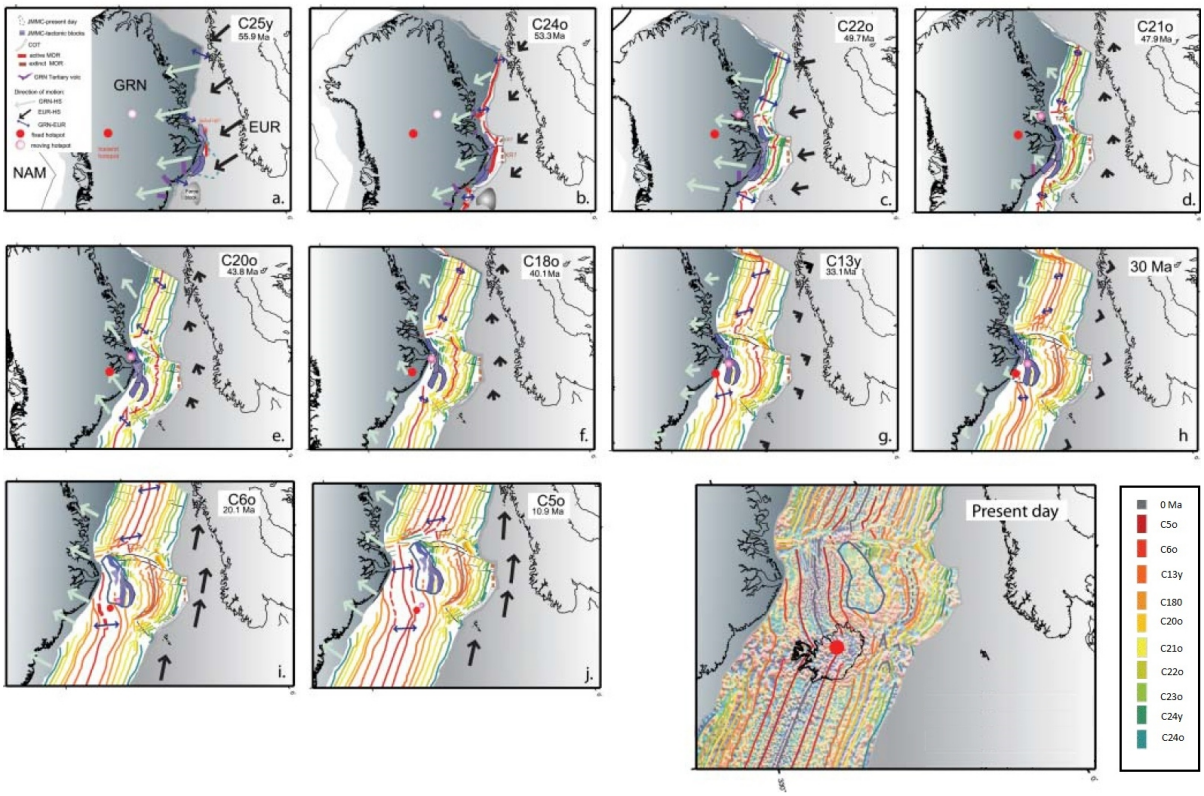

Figure 2.2: Evolution of NE Atlantic plate boundaries, modified from Gaina et al. (2009). Grey arrows marks direction of movement of Greenland while black marks the that of Europe. Colored lines marks the various magnetic anomalies. Red circle infers Iceland Hotspot location.

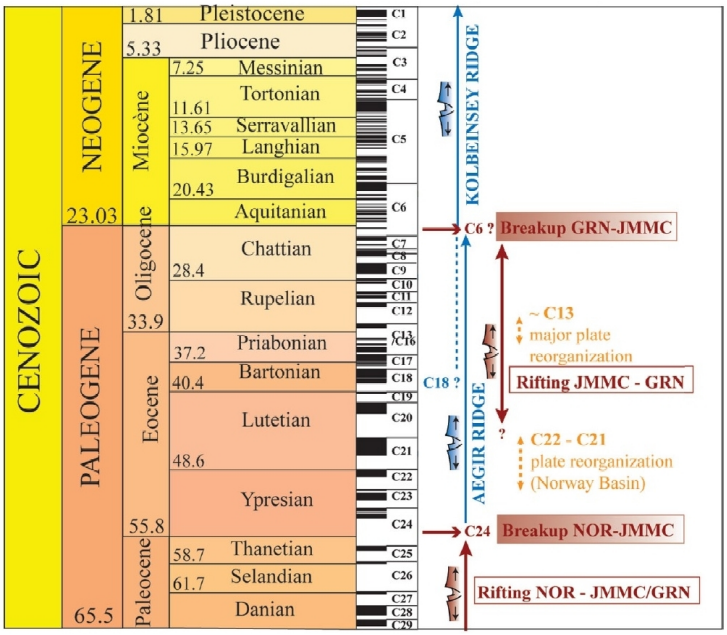

Figure 2.3: Geological timescale with the major tectonic and magmatic events, modified from Peron-Pinvidic et al. (2012) and references within. In the center the polarity chrons are listed.

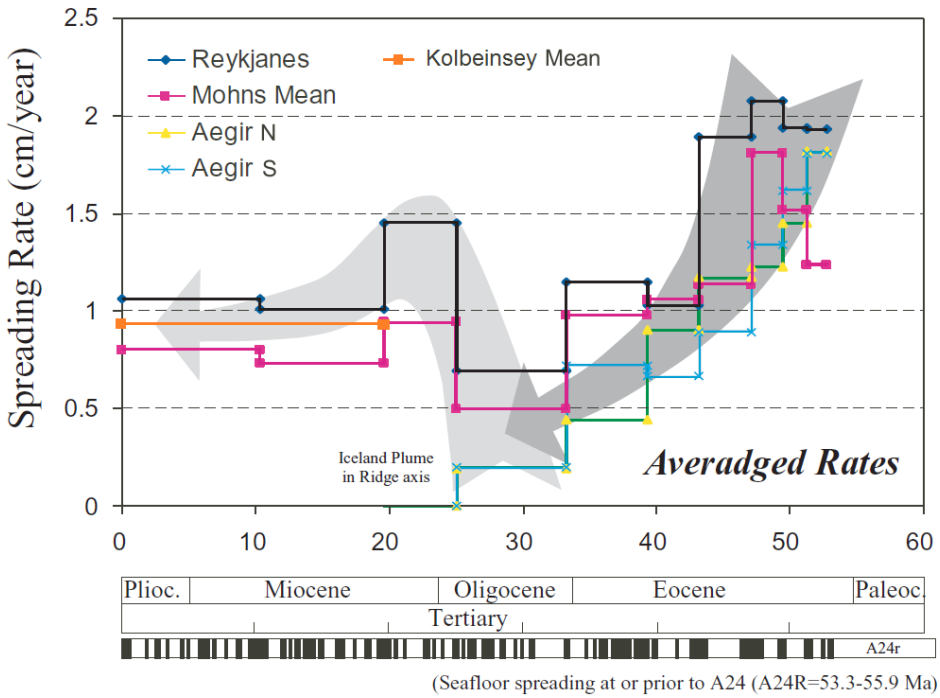

Figure 2.4: Spreading rates calculated from magnetic anomalies on the seafloor, modified from Mosar et al. (2002). Average values are presented for Mohns (magenta) and Kolbeinsey Ridge (orange). Reykjannes Ridge (dark blue / black) is located south of Iceland, and spreading rates are estimated form one profile. Two estimates are presented for the Aegir Ridge, from a northern (yellow / green) and southern (light blue) profile.

2.3 Review of previous investigations in the area

2.3.1 Crustal structure of the Eggvin Bank

The northern boundary of JMMC was investigated by Kandilarov et al. (2012) with two wide-angle seismic profiles. The boundary of the JMMC was interpreted to be along the continuation of the northern lineament of the East JMFZ. It was concluded that the crust between the micro continent and the JMFZ, i.e. underneath Jan Mayen island, is of very complex nature. It is partly similar to oceanic crust, in particular as found underneath Iceland. Alternatively it could be a thinned heavily intruded continental crust, a northward continuation of the JMMC. Velocities are similar to those documented on the western edge of the JMMC (Kodaira et al., 1998). However, they concluded that the crust in this zone is similar to oceanic type crust, supported by the ratios of upper to lower crustal thickness. This was furthermore supported by multi-channel seismic of the top crustal layers, where different signatures are observed along the JMMC and to the north of the micro continent. The total crustal thickness was mapped to range from about 20 km in the south, close to the ocean-continent boundary, to 10 km underneath the Jan Mayen island and towards the JMFZ.

Campsie et al. (1990) presented an early study of the Eggvin Bank, where geo-chemical analysis of dredged samples was evaluated together with a refraction profile (Sørnes and Navrestad,

1976) and a seismological study of surface wave trains (Evans and Sacks, 1979). Here it was concluded that the crust beneath Jan Mayen and the Eggvin Bank was a region of thickened crust, possibly of intruded continental crust extending from the JMMC. Based on early low resolution refraction seismic, Sørnes and Navrestad (1976) mapped a crustal thickness of about 16 km across the Jan Mayen island and along the Eggvin Bank. Evans and Sacks (1979) presented a model indicating a crust about 20 km thick. They concluded that the northern Iceland Plateau, including Jan Mayen and the Eggvin Bank, was underlain by intruded continental crust extending out from the JMMC. The conclusion was based on a seismological study of earthquakes in the JMFZ, recorded on Iceland. The ocean-continent boundary between the Iceland Plateau and the JMMC was later identified by Kodaira et al. (1998). Based on new wide-angle seismic Kodaira et al. disproved parts of the earlier ideas (Evans and Sacks, 1979; Campsie et al., 1990) about the extent of continental crust in the northern Iceland Plateau.

Haase et al. (2003) studied basalt petrology of the Eggvin Bank along the axis of Kolbeinsey Ridge. Incompatible element enriched basalts were identified, different from those in the central parts of the Kolbeinsey ridge. The shallow bathymetry of the Eggvin Bank was ascribed to a Fe-depleted and less dense mantle, compared to the surrounding mantle.

2.3.2 Nearby crustal structure

The structures of the crust around the Eggvin Bank is far better documented than the bank itself. Seismic refraction surveys have been conducted targeting the oceanic crust of the Greenland Basin (e.g., Voss and Jokat, 2007; Voss et al., 2009; Klingelhofer and Geli, 2000; Kandilarov et al., 2012) and the Island Plateau (e.g., Kodaira et al., 1997, 1998; Mjelde et al., 2002a, 2007). Similarly, the crust of JMMC is also well studied (e.g., Kodaira et al., 1998; Peron-Pinvidic et al., 2012; Mjelde et al., 2007; Breivik et al., 2012; Kandilarov et al., 2012).

2.3.3 Studies targeting the magmatism in the area

It is still an ongoing debate about the origin of the magmatism on Jan Mayen and in the Eggvin Bank, as well as the exact relationship between the two of them. The volcanic island of Jan Mayen is built entirely of volcanic rocks younger than 0.7 Ma which belongs to a potassic alkaline suite (e.g., Imsland, 1980; Trønnes et al., 1999). Until recently the Jan Mayen related volcanism was thought to reflect a mantle hot spot (Johnson and Campsie, 1976; Morgan, 1983; Schilling et al., 1983; Vink, 1984), with the Eggvin Bank representing the hot spot track (Morgan, 1981). Basalts from the central parts of the Kolbeinsey Ridge are typical mid-ocean ridge tholeiites, while north of the Eggvin Offset thoeliites are enriched with incompatible elements (Haase et al., 2003; Mertz et al., 2004). The Mohns Ridge basalts are more heterogeneous in composition, varying between alkali basalts and incompatible-element-depleted tholeiites (Schilling et al., 1983, 1999; Haase et al., 1996, 2003). The southern part of the Mohns Ridge contains basalts with increasing concentration of trace elements, as well as increasing Sr - isotope ratios and decreasing Nd- isotope ratios, towards Jan Mayen. This has been interpreted to relate to a mantle plume beneath Jan Mayen.

Bathymetry and earthquake epicenters in the Jan Mayen region do not support plume swell nor an anomalously hot mantle below the region (e.g., Imsland, 1980; Havskov and Atakan, 1991). In a Rayleigh wave tomography study in the North Atlantic Pilidou et al. (2005) concludes that low velocity in the upper mantle beneath Kolbeinsey Ridge may be an extension of hot plume material from Iceland. However, it could also be associated with a plume beneath Jan Mayen. Mertz et al. (2004) discovered that it was no indication of systematic age progression for the volcanic peaks located on the Eggvin Bank, thus providing data contradicting the hot spot track hypothesis. Furthermore, based on studies of Pb-isotopes Mertz et al. (2004) observed that no dispersion of enriched material was observed adjacent to the hypothetical Jan Mayen plume, neither to the north along Mohns Ridge nor to the south along Kolbeinsey Ridge. They conclude that trace element and isotope data do not show any evidence for interaction between mantle sources and hence makes the postulated local Jan Mayen Plume questionable.

Some authors (e.g., Havskov and Atakan, 1991; Gernigon et al., 2008; Kandilarov et al., 2012) suggest that the volcanism on Jan Mayen is caused by minor spreading -or leakage- along the JMFZ. Due to regional change in spreading in the Norwegian-Greenland Sea, stress reorganization could lead to trans-tension and magmatic activity along the pre-existing JMFZ. In such a scenario the magmatic activity is assigned the Iceland Plume, not a local plume beneath Jan Mayen. In a study of the 1985 eruption on Jan Mayen Imsland (1986) concluded that it was an eruption from a leaky transform rather than from the proper Jan Mayen magma system. Haase et al. (1996) suggest that Jan Mayen magmas are ascribed the unique position between a continental fragment, a fracture zone and a spreading ridge, where magma is generated by passively upwelling mantle mainly influenced by the Mohns Ridge. Trønnes et al. (1999) proposed that volcanism originates from low degree partial melts of enriched material, derived from remnants of the ancestral Iceland Plume. The plume head was emplaced in the NE Atlantic at about 60 Ma.

An early study of Pedersen et al. (1976) presented strontium ratio and trace elements from samples taken along the Jan Mayen Fracture Zone, i.e. along the northern Eggvin Bank and the Jan Mayen Platform. These compared well with those of the Jan Mayen Island, and it was concluded that the different studied areas are all part of the same volcanic province. Mertz et al. (2004) identified samples of dredged basalts from the Eggvin Bank as representing two main categories: (1) tholeiitic near-axis lavas geochemically similar to basalts from the neighboring Kolbeinsey Ridge, and (2) transitional-to-alkaline off-axis seamount lavas similar to other alkaline basalts found on the island of Jan Mayen and the Jan Mayen Platform. Their ages are estimated to be < 0.1 Ma and 0.6 - 0.7 Ma, for (1) and (2), respectively. Furthermore, different mantle source for (1) and (2) is supported by isotope ratios. Isotope ratios of (1) resemble those of the south-eastern volcanic zone of Iceland, Vestmannaeyjar. It is interpreted to be related to the emplaced ancestral Island Plume proposed by Trønnes et al. (1999). Isotope ratios of (2) matches with those of the Jan Mayen volcanism. Different source of (1) and (2) is also inferred by different incompatible element composition, Figure 2.5.

Vesteris Island is a submarine volcano of Quaternary age created on top of older oceanic crust (Cherkis et al., 1994; Haase and Devey, 1994). Geochemical analysis indicate a different man-

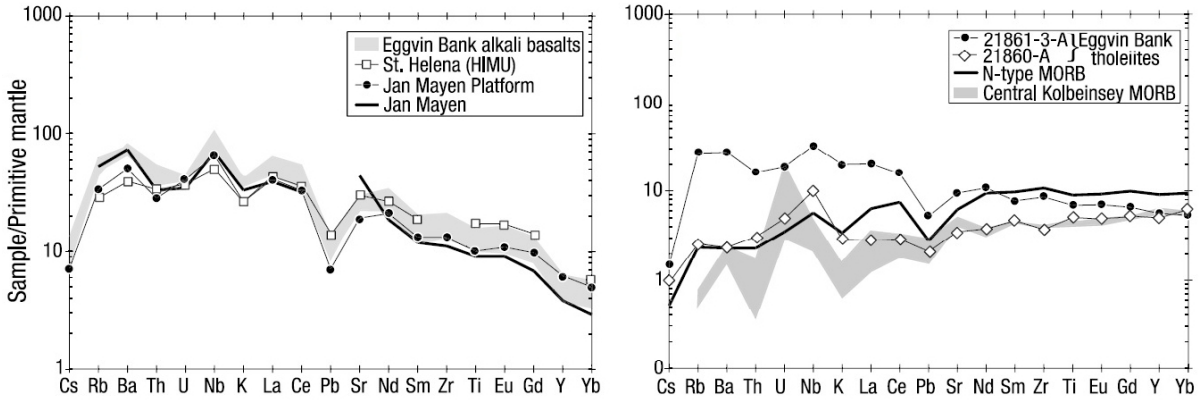

Figure 2.5: Incompatible element (primitive-mantle normalized) plot of Eggvin Bank tholeiites and alkali basalts, modified from Mertz et al. (2004) and references therein. Eggvin Bank basalts are compared to basalts from Jan Mayen Platform, Jan Mayen, central Kolbeinsey Ridge and St. Helena, as well as to normal mid ocean ridge basalts.

tle source than Jan Mayen volcanism (Haase and Devey, 1994). Furthermore, Haase and Devey suggests that the origin is possibly related to extensional stress caused by a combination of (1) reorientation of spreading along the Mohns Ridge and (2) an extension of the Kolbeinsey Ridge axis. Voss and Jokat (2007) published a crustal transect crossing the Logi Ridge, but studies targeting the magmatism directly has so far not been published.

Part II

Seismic Data Processing

Chapter 3

Preliminary Considerations

3.1 Theoretical background

Most of the theoretical background concerning seismic data processing is located separately in different sections, addressing the various applied processing techniques. However, a brief explanation of the frequency content of data is given below. This is fundamental in several of the sections presented in Part II.

3.1.1 Frequency content of data

A discrete Fourier transformation (DFT) can be used to transform a discrete sequence of data samples into a spectrum of its frequency content. That is, a finite list of equally spaced samples can be converted into the list of coefficients of a finite combination of complex sinusoids. Thus, periodicities in the input data, as well as their relative strengths, can be revealed. The inverse process, taking a frequency spectrum and transforming it into a sequence of data samples, can be done by an inverse DFT.

$$\text{DFT:} \qquad F_n = \sum_{k=0}^{N-1} f_k e^{-i2\pi nk/N} \tag{3.1a}$$

$$\text{Inverse DFT:} \qquad f_k = \tfrac{1}{N} \sum_{n=0}^{N-1} F_n e^{i2\pi kn/N} \tag{3.1b}$$

f_k: Function of discrete samples
F_n: Discrete frequency spectrum
N: Number of samples

For example, a seismic time pulse contains a wide range of frequencies which can be obtained through a DFT. In this study both temporal and spatial frequency content of data are evaluated. For a detailed description of the DFT in seismic processing I would refer to any textbook concerning the topic (e.g., Yilmaz, 1987; Stein and Wysession, 2003; Gelius and Johansen, 2010).

3.2 Aquisition and equipment specification

3.2.1 Seismic source

Information about the source was retrieved from the article "Acquisition, processing and analysis of densely sampled P- and S-wave OBS-data on the mid-Norwegian Margin, NE Atlantic" written by Mjelde et al. (2002b). They evaluated the same guns in the same array configuration as what was used during the East Greenland 2011 Survey. The source array was made up from four equally-sized Bolt 1500 C air-guns, giving a total volume of 4800 inch^3. The theoretically estimated far field source signature is displayed in Figure 3.1. The main frequency components lies in the range 5 to 40 Hz, and the main peaks are located at 6, 10 and 18 Hz. It is an high energy source designed for deep penetration and recording at far offsets. The primary peak has an amplitude of 9.8 barm and the peak-to-peak difference is 29.0 barm. The pulse length is about bout 350 milliseconds long. The signature contains considerable effects from the bubble pulses produced by the air guns. During acquisition the source was fired every 200 m along the survey line.

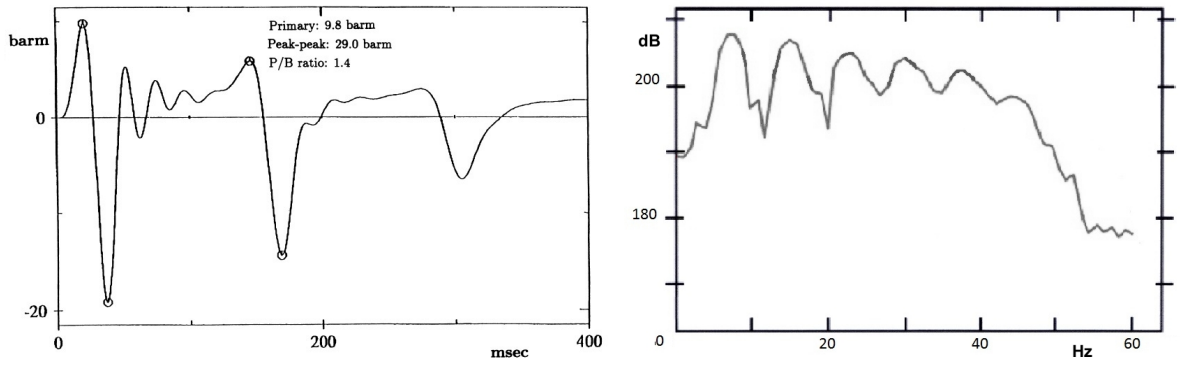

Figure 3.1: Theoretical far field source signature, modified from Mjelde et al. (2002b). Pulse in time domain is displayed to the left and to the right is its frequency content.

3.2.2 Seismic recording systems

Seismic data analyzed in this study is acquired with two different recording systems, a three component Japanese HOKKAIDO-type ocean bottom seismometer (OBS) and a Geometrics GEODE mini-streamer. The mini streamer only recorded on one single channel, so it will be referred to as a single-channel streamer (SCS). OBSs are deployed on the seafloor where they remain stationary during acquisition. The SCS on the other hand is towed behind the ship. The OBS record with three geophones pointing in orthogonal directions with respect to each other, one orientated vertically and the other two horizontally. The SCS makes one single recording, produced by one group of hydrophones, for each shot.

Sampling intervals for the two recording systems were read directly from the SEG-Y header in the two separate data sets. The Nyquist frequency is the theoretically highest possible frequency that can be recovered from a sampled signal (e.g., Yilmaz, 1987; Gelius and Johansen,

2010). If higher frequencies are recorded, these will be registered as lower ones. This is denoted aliasing.

$$\text{Nyquist frequency:} \qquad f_N = \frac{f_r}{2} = \frac{1}{2dt} \tag{3.2}$$

f_r: Recording frequency
dt: Sample interval

The OBS recorded at a sampling interval dt=0.003906 s. The SCS recorded at a sampling interval dt=0.002000 s. The corresponding Nyquist frequencies are 128 Hz and 250 Hz for the OBS and the SCS, respectively. In digital recording systems an anti-alias low-pass filter is routinely applied, eliminating aliasing. For the evaluated datasets aliasing in time domain should not be considered an issue.

3.2.3 Relocating OBSs

Before any processing was done, the OBSs had to be assigned their position along the survey line. This information together with the depth of each OBS were read directly from the navigation file. However, further relocation was needed. When deploying an OBS from a ship it can drift with ocean currents as it descends towards the sea bottom. In-line displacement can be detected from evaluating the hyperbolic shape of the direct arrival, i.e. the water pulse. OBS 3 was relocated 0.4 km. In Table 3.1 the final OBS positions are listed together with the its corresponding depth. Displacement along the survey line can be corrected for. On the other hand, cross-line displacement create errors that are inevitably incorporated into the model and can only be slightly adjusted for during velocity modeling (see also Section 8.2).

Table 3.1: OBS positions along survey line.

	Correct position (km)	Originally assigned position (km)	Depth (m)
OBS 1	260.9	-	1619
OBS 2	220.7	-	964
OBS 3	180.6	181.0	1382
OBS 4	140.5	-	736
OBS 5	100.6	-	2367

Chapter 4

Ocean Bottom Seismometers

Seismic processing of the OBS data involved several steps to improve the signal to noise ratio (S/N ratio) and enhance phases arrivals. In this study a sparse OBS dataset was evaluated, so sorting into central mid-point gathers was not possible. It was then necessary to rely solely on pre-stack filters and techniques for improving the ability of phase identification.

Linear coherent noise can be damped and partially removed through application of pre-stack filters. Non-linear coherent noise in the form of multiples and ghosts, however, are heavily present in all the data and not as easy to remove. Methods designed for such removal are most commonly valid for central mid-point gathers or for zero offset stacked sections, e.g. predictive deconvolution, F-K- and Radon filtering (Yilmaz, 1987; Stein and Wysession, 2003; Gelius and Johansen, 2010).

4.1 Quality of raw data

Of the five OBSs deployed on the sea floor, four of them contained recordings. No data at all was recovered from OBS 5, the one deployed at the northernmost position. OBS 1, 3 and 4 contain good quality recordings on all three channels. In the second horizontal component of OBS 2 the recording was too low to be of any use. Furthermore, in all its components gaps without recording are present in the shot record. These gaps were identified and assigned silent traces through an algorithm presented in Appendix A.1. In Figure 4.1 the raw data from the three component of OBS 1 is displayed. Difference in data quality is seen compared with the raw data of OBS 2, Figure 4.2.

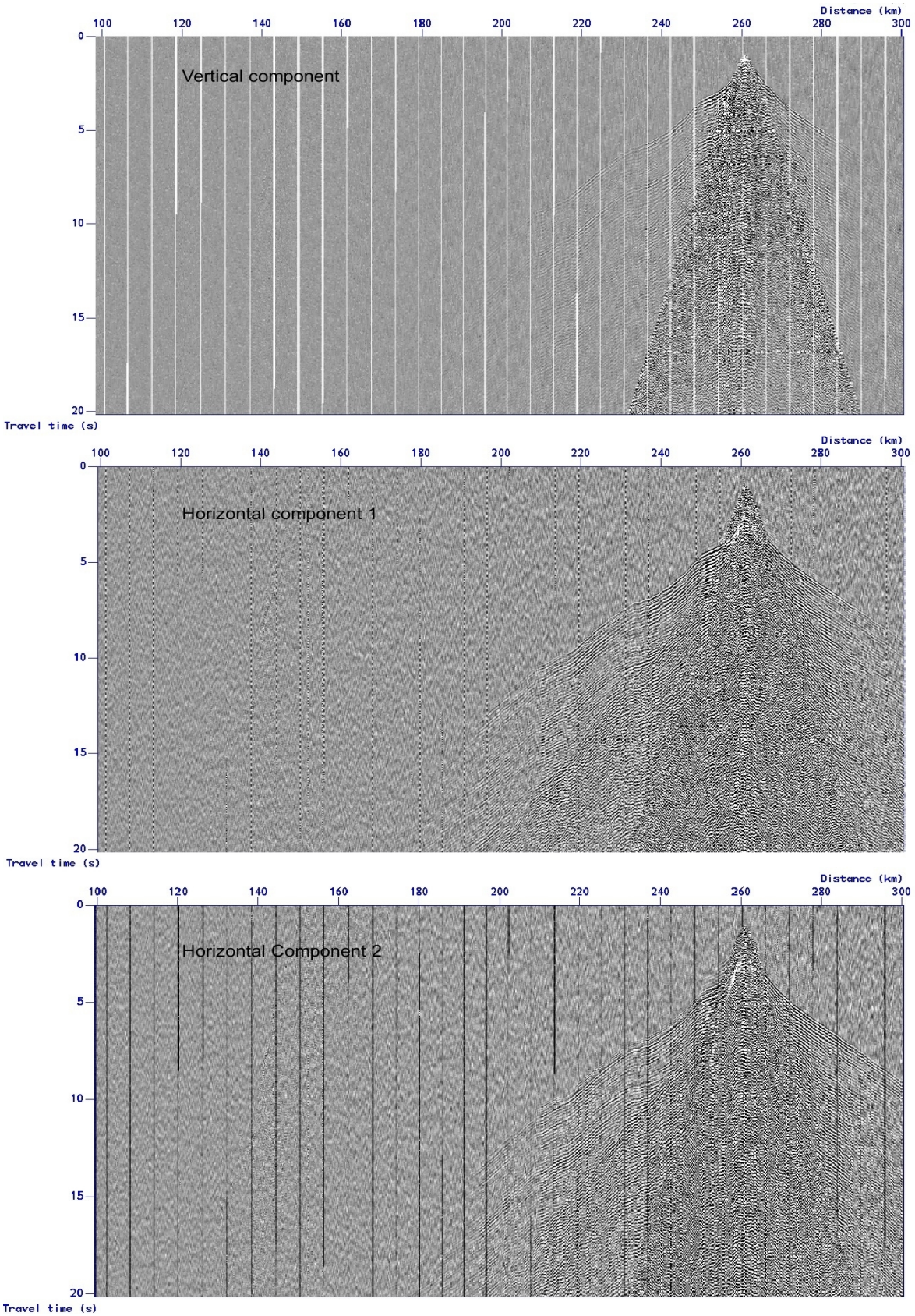

Figure 4.1: Unprocessed three-components data of OBS 1. Uppermost image is the vertical component. Below are horizontal component 1 and 2.

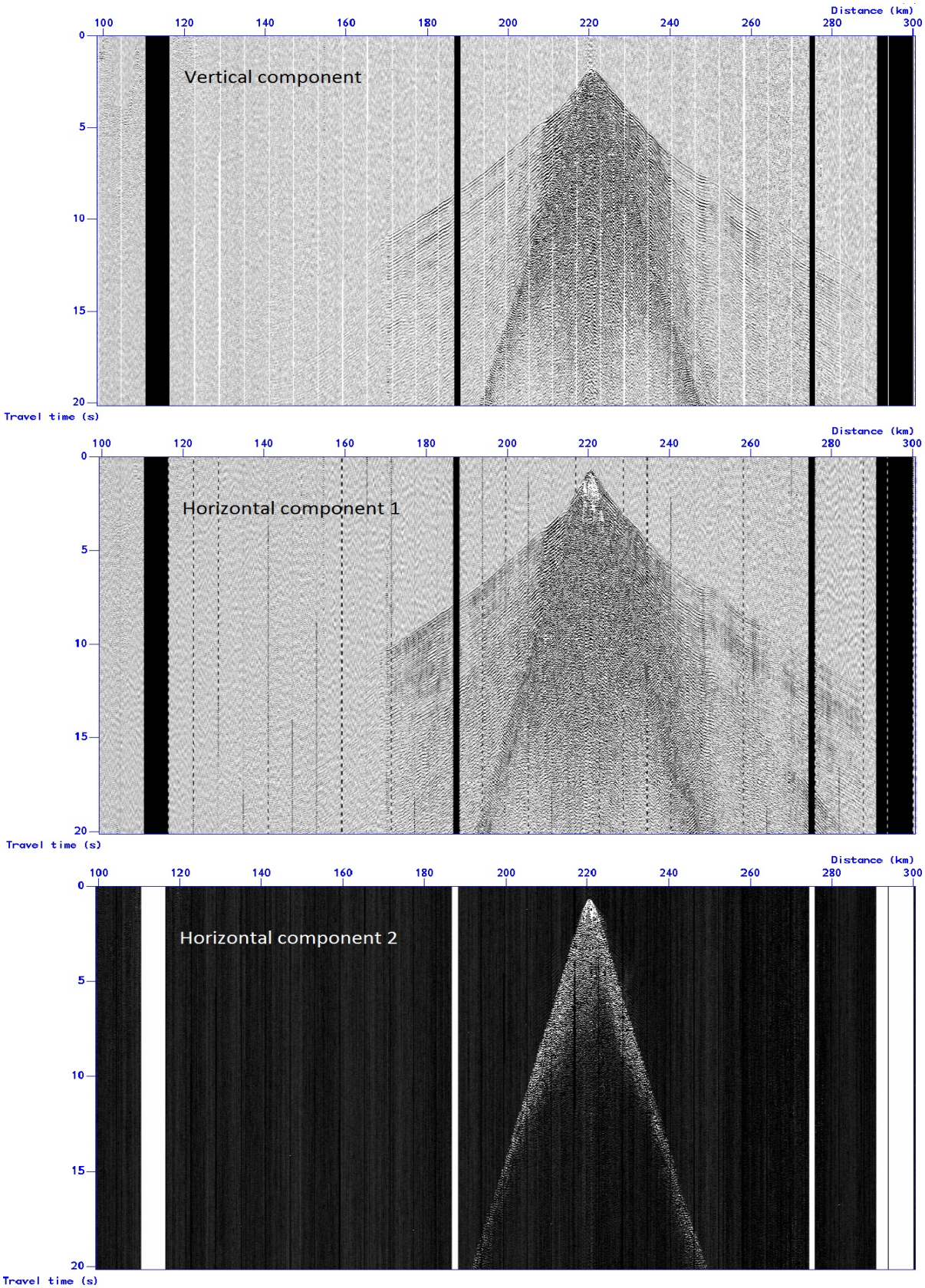

Figure 4.2: Unprocessed three-components data of OBS 2. Uppermost image is the vertical component. Below are horizontal component 1 and 2.

4.2 Vertical component

4.2.1 Work flow

Processing was done in Seismic Unix. Table 4.1 presents the work flow applied to the data.

Table 4.1: Seismic Unix work flow for OBS data.

```
$ cat unprocessed_data.su |  \
  sugain mbal=1 |  \                  # Trace balancing
  sureduce rv=8.0 |  \                # Velocity reduction
  supef maxlag=0.35 |  \              # Spiking deconvolution
  sufilter f=3,5,12,16 |  \           # Band-pass filter
  suweight key=offset |  \            # Trace weighting
  > processed_data.su
```

After applied work flow an improvement of S/N-ratio was achieved together with a remarkable enhancement of phase-arrivals. For example, some phases were present at offsets extending to 100 km and even more. The final processed vertical components are attached in Appendix B.1 together with the results from velocity modeling.

Trace balancing

To make an adjustment to the amplitude scale of traces, trace balancing is added to the work flow. One and one trace is balanced by subtracting the mean value. A better coherency between neighboring traces is obtained by doing this.

Velocity reduction

For the purpose of identifying phases and make the picking of them easier, it is convenient to reduce the dips in the OBS data. Another reason is to reduce the amount of space necessary for displaying the data. Instead of displaying the data in a plot with offset and travel time, it is rather displayed with offset and reduced time. That is; $t - x/v_{red}$, with "x" being offset and "v_{red}" being the reduced velocity. As often done in seismic crustal studies, the velocity of reduction was set equal to 8 km/s. This value is chosen as an approximation to the mantle velocity. Mantle refractions should then be seen as horizontal arrivals in the processed OBS data.

Spiking deconvolution

Spiking deconvolution will remove ringing parts in the seismogram that are produced by the source wavelet. It will transform the waveform into a spike and make it easier to identify the various arrivals in the receiver gather. The seismogram is a convolution between the wavelet and the phase arrival series, in addition to the non-coherent noise.

$$s(t) = w(t) \circ A(t) + n(t) \tag{4.1}$$

s(t): Seismogram
w(t): Wavelet
A(t): Phase arrival series
n(t): Noise

An inverse Wiener filter can be designed to transform the wavelet into a delta spike. Necessary assumptions are that the source is known and that its waveform is causal and minimum phase. The Wiener filter has the property that it calculates the inverse of an input waveform. The inverse is actually not an exact inverse, but rather a least squares estimate. White noise is added to the frequency components of the source to avoid division by zero. In the work flow a relative additive noise level was set to 0.001 (the default value in "supef"). If it is further assumed that no noise is present in the seismogram (n(t)=0), convolving the same filter with the seismogram will the yield the pulse arrival series.

$$w(t) \circ f(t) = \delta \rightarrow f(t) = w(t)^{-1} \tag{4.2}$$

$$f(t) \circ s(t) = f(t) \circ (w(t) \circ A(t)) = \delta \circ A(t) = A(t) \tag{4.3}$$

f(t): Filter
δ: Delta function (spike)

The statistical approach, where the wavelet is unknown, is based on the assumption that the pulse arrival series is random and has the property of white noise, i.e. the autocorrelation of the pulse arrival series yields a constant. The source wavelet can then be approximated through an autocorrelation of the seismogram.

$$w(t) \circ A(t) = s(t) \rightarrow U_w A_0 = U_s \tag{4.4}$$

U: Autocorrelation
A_0: Constant

The autocorrelation analysis consists of deciding two user specified time windows, the gap and operator length. In spiking deconvolution the gap length is by definition set to be equal the sampling interval (Yilmaz, 1987; Stockwell Jr. and Cohen, 2007). The operator length will approximate the source wavelength. It is chosen to be equal the width of the smallest autocorrelation waveform (Yilmaz, 1987; Stockwell Jr. and Cohen, 2007). At far offsets the seismic pulse evolves to become somewhat wider then what it is at near offsets, as a result of attenuation, dispersion etc. This should be taken into concern when choosing the waveform. That is, the autocorrelation should be evaluated at offsets the deconvolution should be successful. Autocorrelations of near offsets of OBS 1 are displayed in Figure 4.3. A great variety in waveforms is seen throughout the autocorrelation. However, a waveform identified for all traces is about 320 ms long. This was also true for offsets greater than what is displayed in the image. However, at far offsets (> 50 km) the autocorrelation became unclear. A length about 320 ms this size is supported by the theoretical far field signature (see Figure 3.1). The operator length was in the

end put equal 0.3500 seconds, the length that gave the best results. Figure 4.4 displays the OBS data before and after spiking deconvolution.

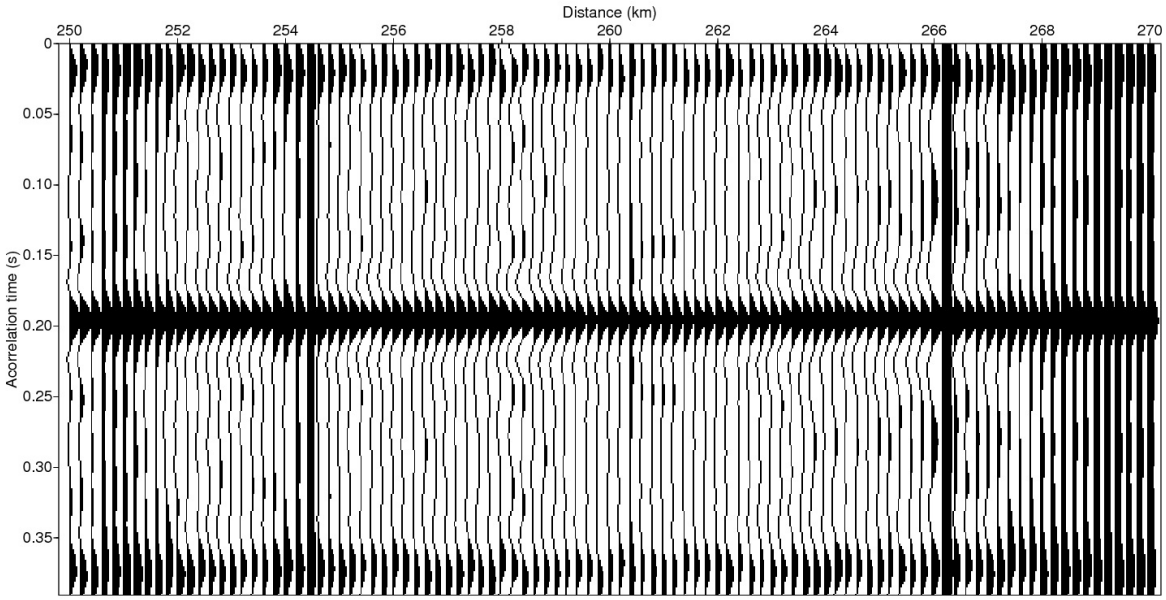

Figure 4.3: Autocorrelation of seismogram (OBS 1).

Bandpass filtering

A band-pass filter can be employed to remove non-coherent noise. It is a filter designed to remove low and high frequencies corresponding to disturbances not generated by the seismic, e.g. environmental noise and sounds coming from the survey machinery and the recording equipment itself. Furthermore, after deconvolution the frequency spectrum is altered because of a boost of both noise and signals (Yilmaz, 1987). It is then necessary to apply a bandpass filter afterwards to remove the unwanted frequencies. The boost effect is clearly visible in Figure 4.4.

Noise coming from water currents and micro-seismic generally is present in OBS recordings at around 0-3 Hz (Trevorrow et al., 1989; Webb and Cox, 1986). Noise from ground roll is also found at this range of low frequencies (Yilmaz, 1987). High frequency jitter from electrical equipment is often manifested at frequencies from and above 50 Hz (Yilmaz, 1987; Mjelde et al., 2002b). In general, arrivals from the deep crust and upper mantle are strongly attenuated at frequencies above 10 Hz (Mjelde et al., 2002b). In wide angle data processing, a band-pass filter in the range 5 to 20 Hz is commonly applied (e.g., Kandilarov et al., 2012; Kodaira et al., 1998; Mjelde et al., 2007; Voss et al., 2009; Breivik et al., 2012).

During truncation of the frequency spectrum, when cutting off unwanted lower and higher parts, the design of the filter plays and important role in avoiding distortions in time domain. The distortions from band-pass filtering, denoted Gibbs Phenomenon, is seen as ringing in time domain. A good design is such that the cut off is done through gradual transition so little ringing is created.

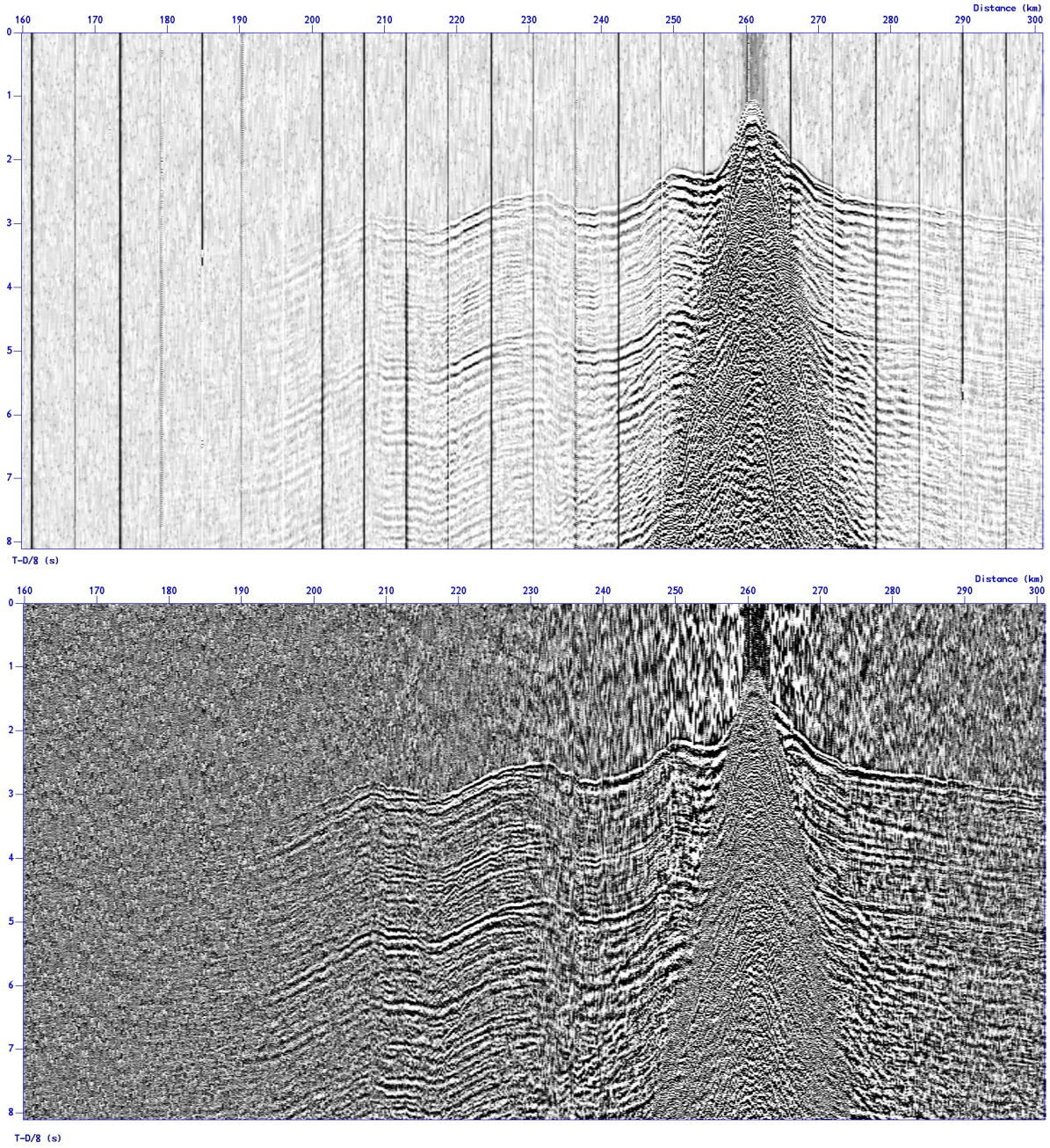

Figure 4.4: Receiver gather (OBS 1) before and after spiking deconvolution. Trace balancing and velocity reduction have been applied to the data in the top image. In the lower image spiking deconvolution has also been applied.

Figure 4.5 presents the frequency spectra of entire traces at zero offset, 50 km offset and 100 km offset. In the zero and 50 km offset peaks corresponds with the those in the theoretically derived spectrum, i.e. 6, 10 and 18 Hz (see Figure 3.1). It is observed how high frequencies are abundantly present at zero offset, but are attenuated at far offsets. At 100 km offset it is difficult to separate the frequency content of the source with the background ambient noise. Nevertheless, signals can still be identified in the OBS data at this distance. It merely show that the energy difference is minimal between the trace with the signal and the trace without signal.

Peaks at 6, 10 and 18 Hz contain the main source energy (Mjelde et al., 2002b), though 10 and 18 Hz also will attenuate at far offsets. To each of the four OBSs a band pass filter of 3/5/12/16 was chosen for low cut / low pass / high pass / high cut, respectively. Such a filter will then conserve the frequency source peaks at 6 Hz and 10 Hz, while the frequency bands heavily contaminated with noise will be muted. Figure 4.6 presents the result obtained after band-pass filtering.

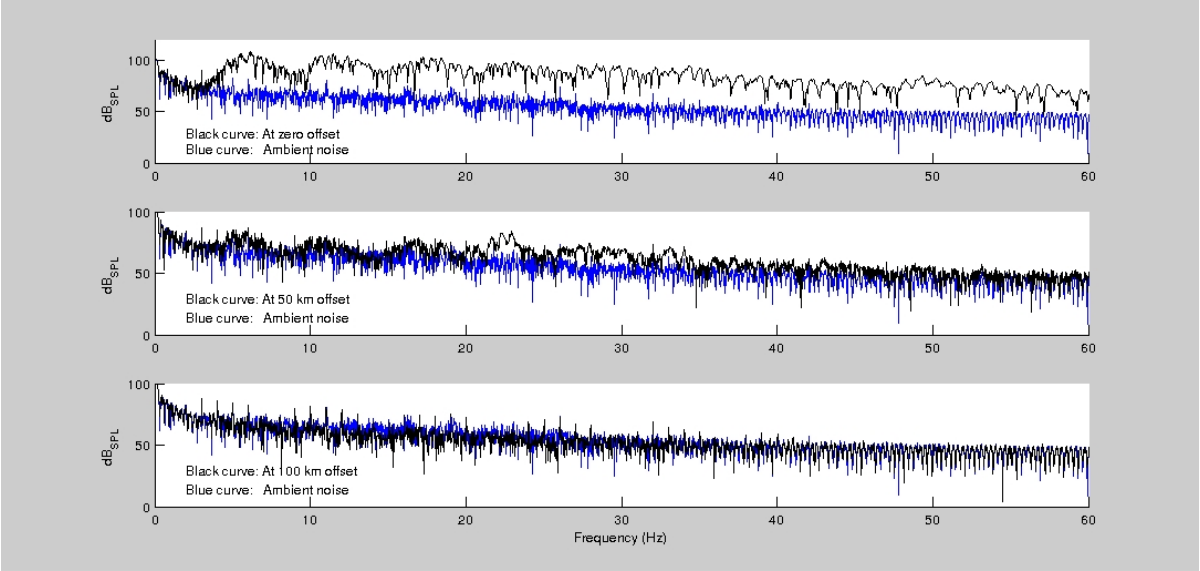

Figure 4.5: Frequency analysis of OBS 1 at zero, 50 and 100 km offset. Amplitudes were rescaled to decibel (20*log[A/A_0]). The underwater Sound Pressure Level (SPL) of 1 μPa was used as the reference amplitude "A_0". The frequency content at each distance is compared with an approximation to the ambient noise level (blue curve). The approximation is a recording made outside the reach of the seismic waves, at offsets greater than 200 km. At near offsets the frequency spectra contains more energy than the ambient frequencies. At 100 km the frequency spectra is difficult to separate from the ambient frequencies.

Trace weighting

Amplitude decays with propagation distance because of geometrical spreading, transmission losses and intrinsic attenuation. An amplitude correction can be added to the traces to enhance weak signals recorded at far offset traces, compared to more energy rich at shorter offset. This is done to enhance the weaker signals, but not to recover any kind of representation of true amplitude. Weighting is a method where traces are scaled proportionally with their offset alone. Corrections of the travel time within each single trace is not take into consideration. Figure 4.7 presents the final result obtained for OBS 1 after the whole work flow has been applied.

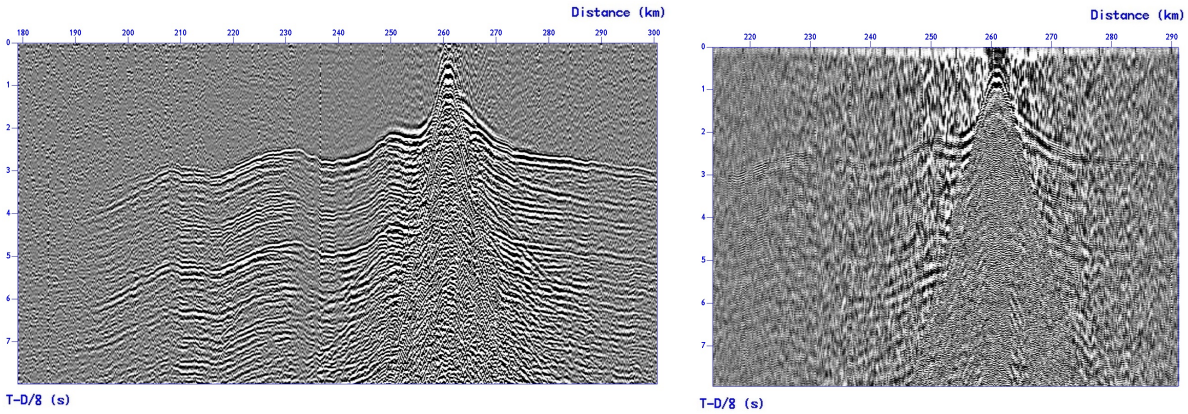

Figure 4.6: Band-pass filter (OBS 1), Low cut/low pass/high pass/ high cut = 3/5/12/16. Left: Residual. Right: Inverse filter.

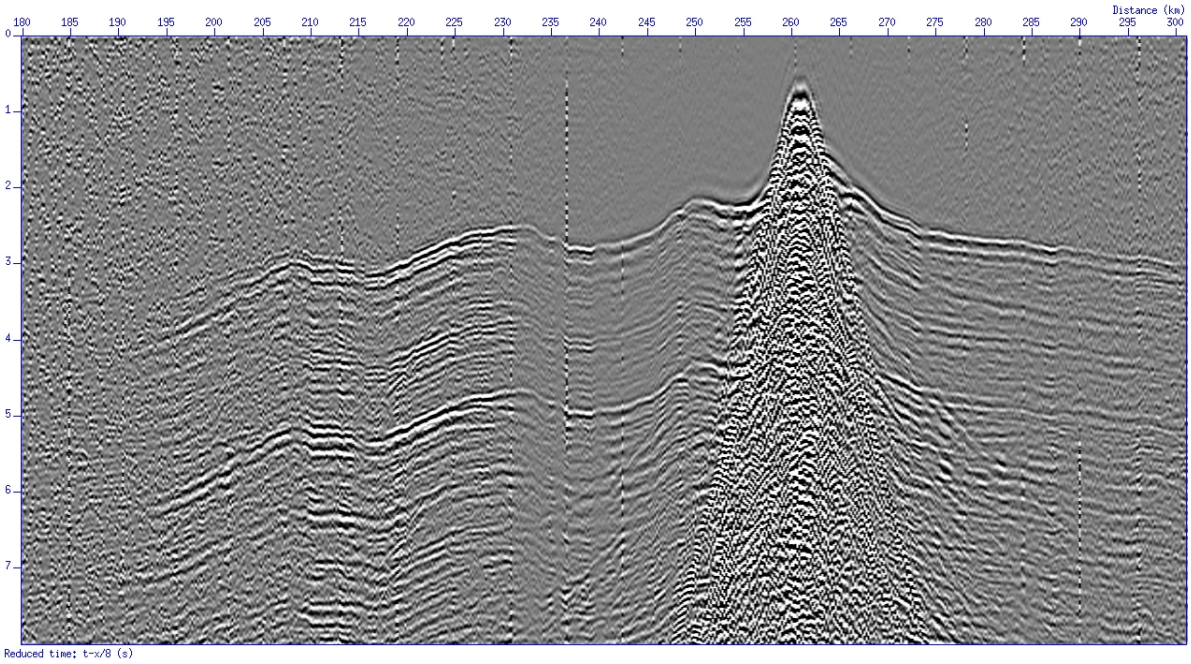

Figure 4.7: Vertical component of OBS 1 after applied work flow.

4.2.2 Additional processing attempts

FK-filter

A FK-filter was applied to the work flow, attempting to remove low velocity arrivals. In the end it proved little efficient because of high spatial aliasing, and it was not applied to the work flow. The data it actually removed was of low frequency, which anyway would be removed by the applied band-pass filter (3/5/12/16 Hz).

The apparent horizontal velocity can be related to the frequency and the horizontal wavenumber.

$$c_x = \frac{\alpha}{sin\, i} = \frac{f}{k_x} \tag{4.5}$$

c_x: Apparent horizontal velocity
α: Medium velocity
i: Angle of incidence
f: Frequency
k_x: Horizontal wavenumber

FK-filtering makes use of the relationship between the slopes of the arrivals in the OBS data and their corresponding position in F-K domain. This can help identify unwanted arrivals and remove them, i.e. mute a given range of apparent velocities. The mute lines are designed as smooth transitions to avoid ringing in x-t domain, the two dimensional equivalent of Gibbs Phenomenon.

Processing was done with the attempt to eliminate arrivals with low apparent velocities like direct waves, late arrivals and ground roll. The FK-spectrum before and after velocity filtering is displayed in Figure 4.8. The residual of the the FK-filtered data are also displayed. The same figure displays the inverse filter, showing which arrivals that actually are muted. Some linear noise parallel to the first breaks has been attenuated. This could have made it easier to detect shallow refractions and secondary arrivals. The filter was not very effective, though an amount of distortion is removed. The first arrivals, however, remain untouched by the filter.

The best results were achieved for setting the cut and pass lines in the FK spectrum equal $\pm$ 0.63 and $\pm$ 0.50, respectively. This corresponds to cutting all apparent horizontal velocities under $\pm$ 1.6 km/s and passing those above $\pm$ 2.0 km/s.

```
$ sudipfilt dx=0.2 dt=0.003906 slopes=-.63,-.50,.50,.63 < unprocessed_data.su \
  > data_with_applied_FK_filter.su
```

Spatial aliasing can clearly be seen in the FK-spectrum in Figure 4.8. It happens at the Nyquist wavenumber.

$$k_{Nyquist} = \frac{1}{2dx} = 2.5\, km^{-1} \quad , \qquad \text{for dx=200m} \tag{4.6}$$

For an arrival with an incidence angle "i", aliasing occurs at a specific frequency:

$$f = \frac{c}{2\ dx\ sin(i)}. \tag{4.7}$$

In the FK spectrum around 5 – 10 Hz, different slopes are spatially aliased at different frequencies. For a more densely sampled line, the FK filter would be more efficient.

Trace mixing

To aid identification and picking of weak far offset arrivals from the mantle, trace mixing can be applied to the data (Samson et al., 1995). Horizontal arrivals will be enhanced at the expense of dipping ones. Horizontal arrivals are those with velocities corresponding to the reduction velocity, i.e. that of the mantle. When mixing traces, a number of traces are weighted in a specific

way, added together and normalized. An attempt was given in put together traces in groups of five with weighting 1, 2, 3, 2 and 1, respectively.

```
$ sumix mix=1,2,3,2,1 < processed_data.su > processed_data_with_trace_mixing.su
```

Mixing does not give any new information, but it can be used to assure the interpretor when picking unclear arrivals at very far offsets. In Figure 4.9 a mixed data from OBS 4 is compared with an unmixed. Over the whole profile, and especially at far offsets, a slightly enhancement of horizontal arrivals is observed.

Automatic gain control

In OBS 2 and 4 there were certain offset ranges with very low amplitudes. This made the identification of phases more difficult. Automatic gain control (AGC) was then added to the work flow instead of weighting to help boost the signal at these offsets. In AGC a window is moved over the trace, recalculating values by comparing with neighboring values that lies within the window. This seemed to be very efficient to enhance first phases, as seen in Figure 4.9. The window length was chosen to be 2.0 seconds.

```
$ sugain < input.su > output_with_AGC.su agc=1 wagc=2
```

Amplitude clipping

Amplitude cutting can make it is possible to enhance weaker signals. Percentile is used to determine how amplitudes outside a specified range should be clipped. Percentile contains the values that fall below a given percentage. Cutting away the high amplitudes, weaker signal can be enhanced. S/N ratio drops dramatically as noise also get boosted. However, consulting a data set with a high cut was found to be a handy tool to aid interpretation. Figure 4.9 displays OBS 4 after amplitude clipping. Implementation in Seismic Unix of an amplitude cut of the highest 40% is presented below.

```
$ suximage < processed_data.su perc=60
```

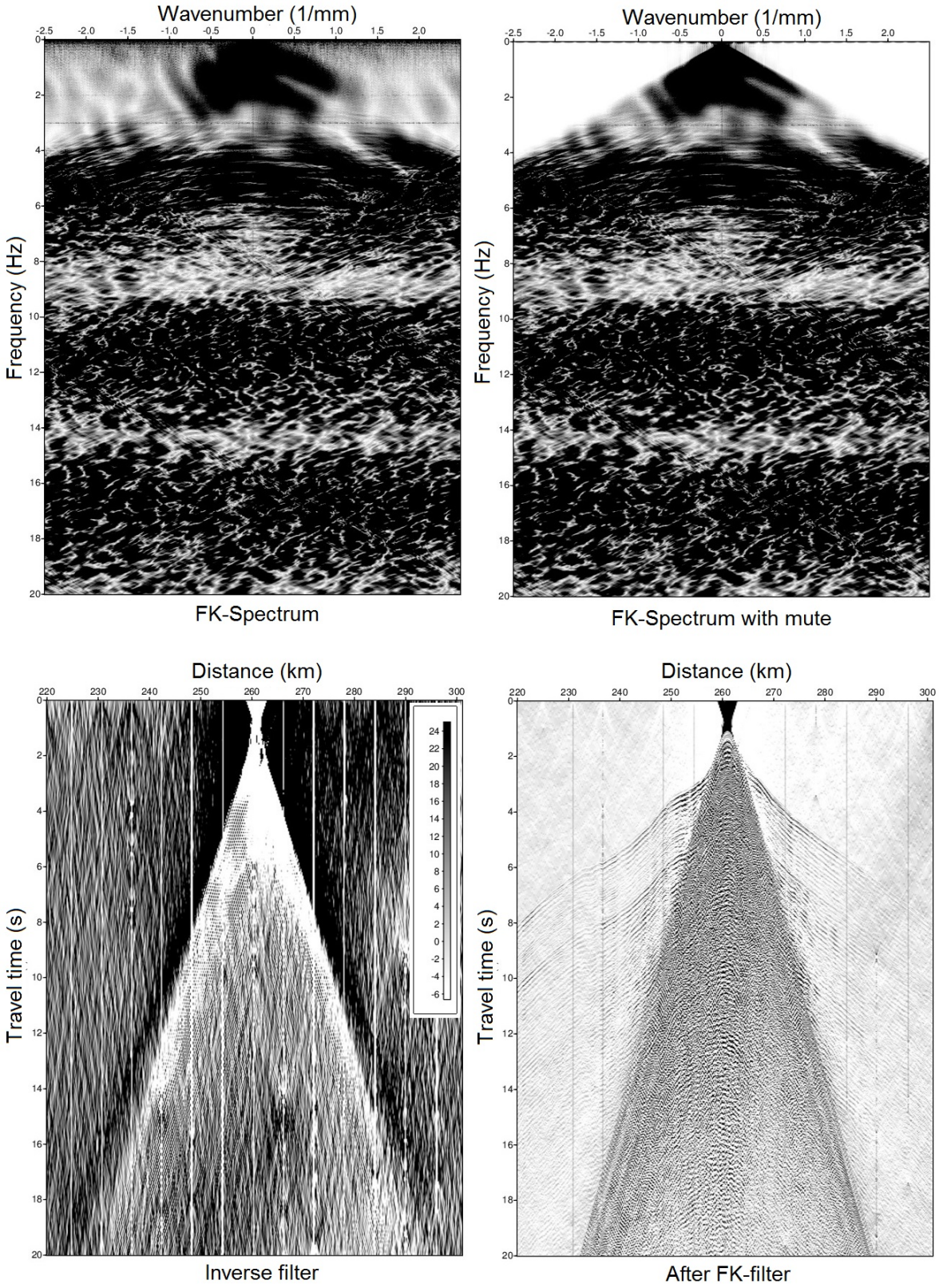

Figure 4.8: F-K filter -0.63/-0.50/0.50/0.63 (OBS 1). Top left: Unfiltered F-K spectrum. Top right: F-K spectrum after applied filter. In the FK-spectrum white color represents zero value while black color represents amplitude value. Bottom left: Inverse filter. Bottom right: Residual. No other processing had been applied to the data. In the OBS data normal coloring is used, with a relative amplitude scale between positive and negative, respectively black and white.

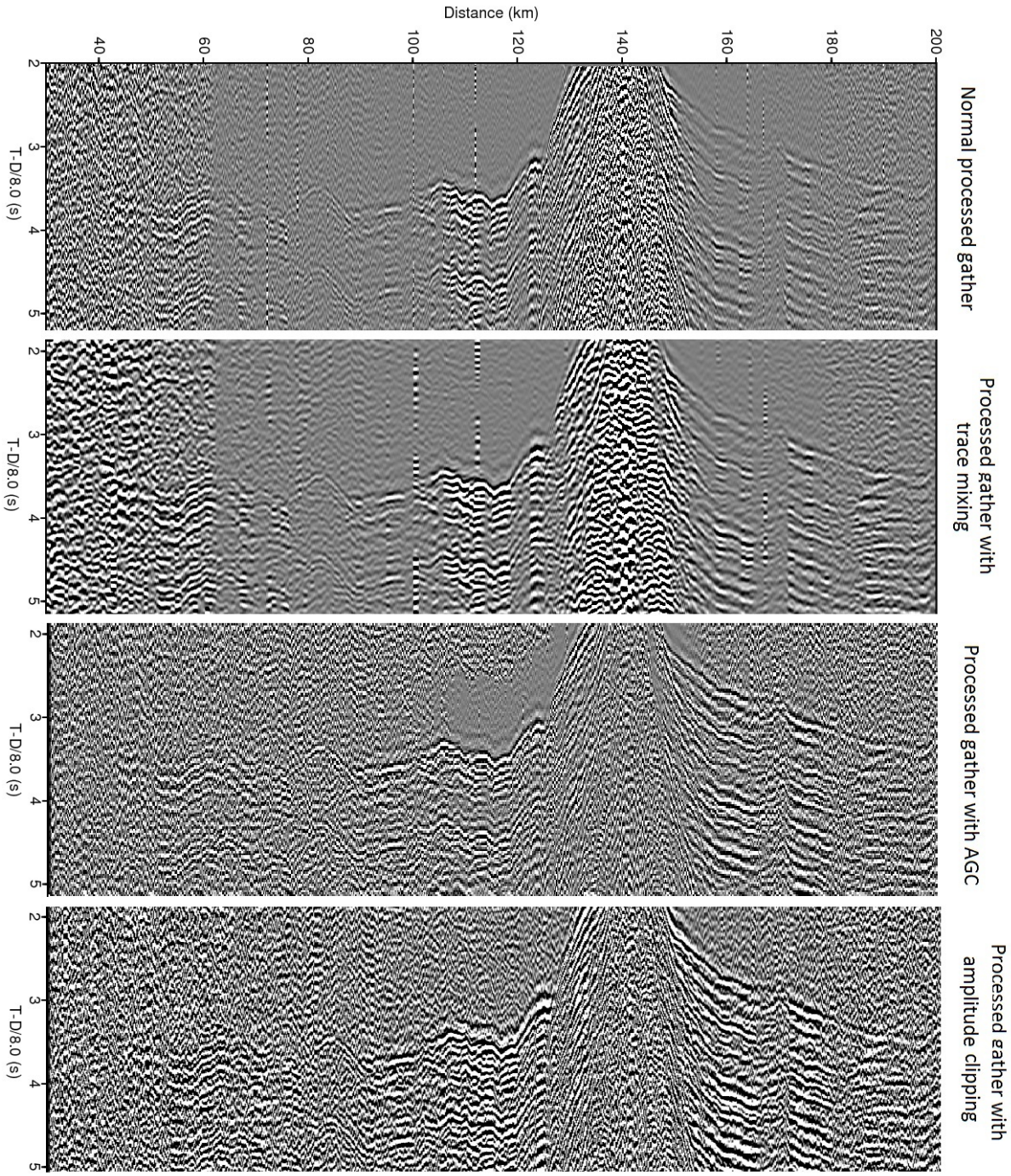

Figure 4.9: OBS 4 with normal processing, applied trace mixing, AGC and amplitude cutting, from top to bottom respectively.

4.3 Horizontal components

4.3.1 Polarization analysis

When an OBS is deployed from a ship, the horizontal components lies in an unknown orientated with respect to the survey line. However, the vertical component points in the vertical direction. A simplification is made in assuming that the p-wave motion is fully contained within the vertical component and that the s-wave motion is contained in both horizontal components. Horizontal components for each OBS are separately rotated into radial and transverse direction. When properly rotated the S-wave energy will be contained in the radial in-line direction alone. The transversal cross-line direction should not contain energy coming from converted S-waves, unless there are anisotropy effects. When looking at real world data, both radial and transversal components contains seismic arrivals, but the radial direction should nevertheless contain more energy than the transversal. For a right-handed system the radial component points along the survey direction, towards the end of the line.

From a three dimensional polarization analysis of three component data it is possible deduce the orientation in the horizontal plane (Maercklin, 2007). That is, a three dimensional analysis will be carried out to find the two dimensional orientation of the horizontal components.

Three orthogonal and mono-frequent oscillations leads to the formation of a polarization ellipsoid. Its spacial orientation depends on the phase difference between the oscillations. Seismic signals, on the other hand, consist of a wide frequency band and display more complex trajectories than an ellipsoid. Nevertheless, for a discrete time window the complex trajectory can be fit to an ellipsoid in a least-squares sense by means of a covariance analysis (Cliet and Dubesset, 1988).

$$M = \begin{pmatrix} var(X) & cov(X,Y) & cov(X,Z) \\ cov(X,Y) & var(Y) & cov(Y,Z) \\ cov(Z,X) & cov(Z,Y) & var(Z) \end{pmatrix} \tag{4.8a}$$

$$cov(X,Y) = \frac{1}{N} \sum_{k=-L/2}^{L/2} [X_k(t) - \mu_x][Y_k(t) - \mu_y] \tag{4.8b}$$

$$var(X) = cov(X,X) \tag{4.8c}$$

Z,Y,X:	Vertical and the two horizontal components
N:	Number of samples in window
L:	Window length
μ:	Mean value of each time sequence within the analyzed window.

An eigenvalue analysis of the covariation matrix M will give the principal axis V_i of the ellipsoid. The eigenvalues λ_i are the axis lengths.

$$MV_i = \lambda_i V_i \tag{4.9}$$

V_1 gives the direction of propagation, corresponding to the true p-wave motion. The azimuth angle can then be found from the horizontal components of the major principal axis. The orientation of ϕ has an ambiguity of 180^0 (Maercklin, 2007).

$$\phi = arctan\frac{y}{x} \qquad \text{where } V_1 = (z, y, x) \tag{4.10}$$

Seismic Unix was used for implementating of the analysis.

```
$ supolar <input_3components_clipped.su wl=0.25 phi=3 angle=rad rl=2 rlq=1
```

The input file is sorted three component data that consist of a cut out time window around the direct water pulse. Maercklin (2007) explains more into detail the necessary format of the three component input data. Furthermore, a complete shell script example is given in Appendix A.2. "wl=0.25" defines the length of the correlation window, which was put equal the trace length in the input file. The command "phi = 3" will print to file the horizontal azimuth of principal axis. The result of this operation will thus yield the difference between the arbitrary orientations of the horizontal components as they were during recording, and the preferred radial-transversal orientation.

Rectilinearity "RL" is a measure of the degree of linear polarization of an event (Kanasewich, 1981). It is commonly referred to as the quality of polarization because it displays to what extent the recorded waves are polarized. RL = 1 means it is a perfect linear polarization, while a value of RL = 0 indicates an undetermined direction of polarization. Several variants of rectilinearity are available. In this study the definition presented by Jurkevics (1988) has been employed. This evaluates the rectilinearity on the basis of all three eigenvalues λ_i. The contrast factor "Q" determines the sensitivity for certain degrees of polarization. Usually it is set equal or less than 1 (Maercklin, 2007). In this analysis it was put equal 1.

$$RL = 1 - \left(\frac{\lambda_2 + \lambda_3}{2\lambda_1}\right)^Q \tag{4.11}$$

Table 4.2 lists the result from the analysis for all OBSs. The analysis could not be done on OBS 2, as it only contained one horizontal component with useful recording. Figure 4.10 presents the detailed results from polarization analysis of OBS 1. Angles with opposite polarity are shifted. Radial direction is defined to point away from the start point towards the end of the survey line. Amplitudes of the direct pulse had to be evaluated to decide the polarity. The average of the calculated azimuth values is the angle used for rotation of the horizontal components.

Table 4.2: Results of polarization analysis. Numbers are average values.

	OBS1	OBS2	OBS3	OBS4
Azimuth:	305^0	-	202^0	179^0
Rectilinearity:	0.87	-	0.82	0.81

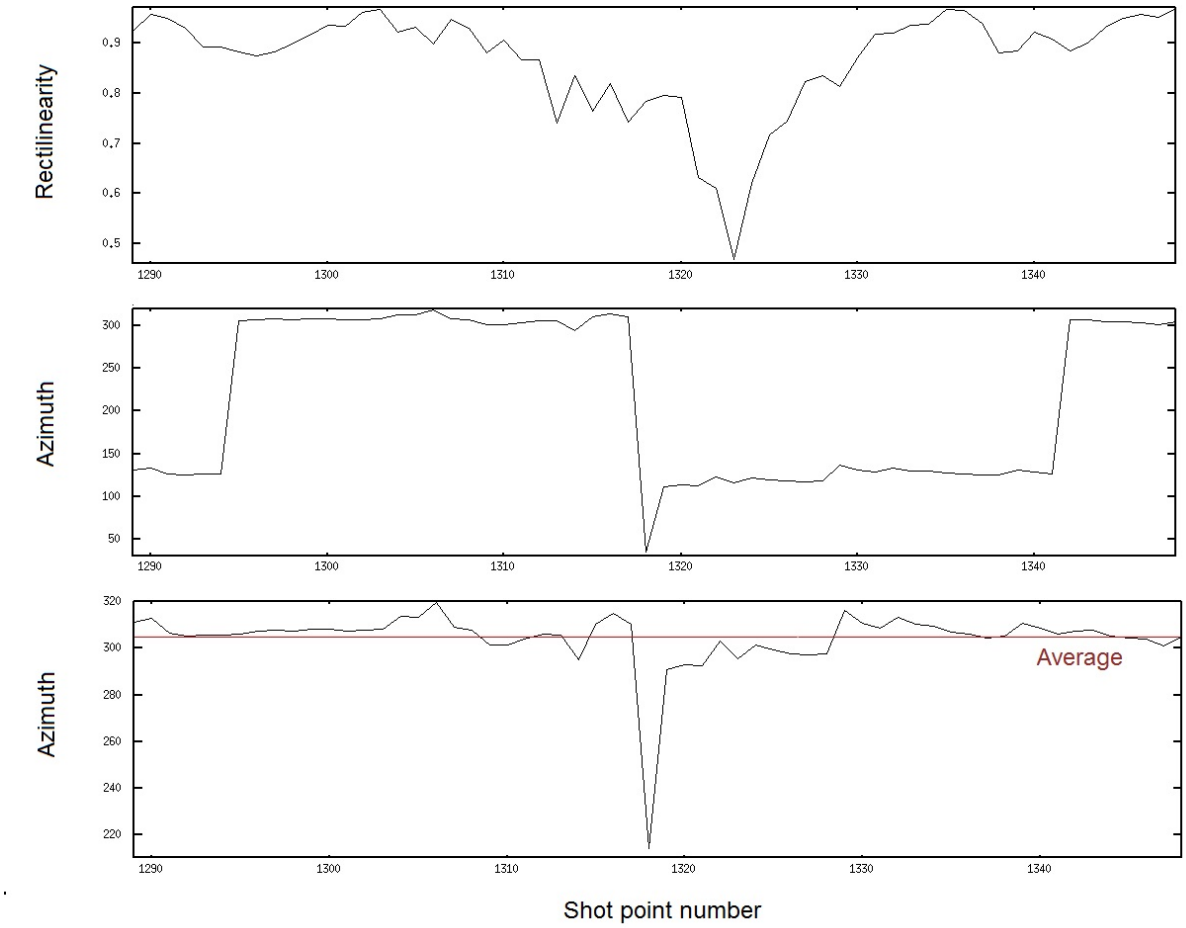

Figure 4.10: Polarization analysis of OBS 1. Top image shows the rectilinearity analysis. The image in the middle display the calculated azimuth angles. In the lowermost image the 180^0 ambiguity is corrected for. The average azimuth angle is marked with a red colored line, $\phi_{average} \approx 305^0$. The azimuth angle at OBS location was excluded when estimating the average value.

4.3.2 Rotation of components

Rotation of the horizontal components was done through a change of coordinate system, from (Z,Y,X) to (Z,R,T):

$$\begin{pmatrix} Z \\ R \\ T \end{pmatrix} = \begin{pmatrix} 1 & 0 & 0 \\ 0 & cos\phi & sin\phi \\ 0 & -sin\phi & cos\phi \end{pmatrix} \begin{pmatrix} Z \\ Y \\ X \end{pmatrix} \tag{4.12}$$

Z: Vertical component
R: Radial component
T: Transversal component
X,Y: Horizontal components
ϕ: Azimuth angle.

The numerical calculation of the rotation was carried out in Seismic Unix. Below, "$Angle" is a variable representing the rotation angle. The data is sorted with trid=12,13,14 for the vertical, first horizontal and second horizontal direction, respectively. The input format is the same as used in the polarization analysis, see Appendix A.2 or examples provided by Maercklin (2007).

```
$ suhrot <input_3components.su > rotated_3components.su \
  a=0,$Angle,$Angle key=trid x=12,13,14 angle=deg
```

Figure 4.11 shows a comparison of the non rotated and the rotated horizontal components of OBS 3. It was rotated 202^0. This OBS is chosen as an example because it shows quite clearly how the polarization analysis yields a radial component with more energy over the first break than what the transversal component has. The radial and transversal components look similar to the original horizontal ones, despite a rotation of $180^0 + 22^0$. However, minor differences were observed when zooming in on the traces, confirming that a trivial solution had not been caused by any errors.

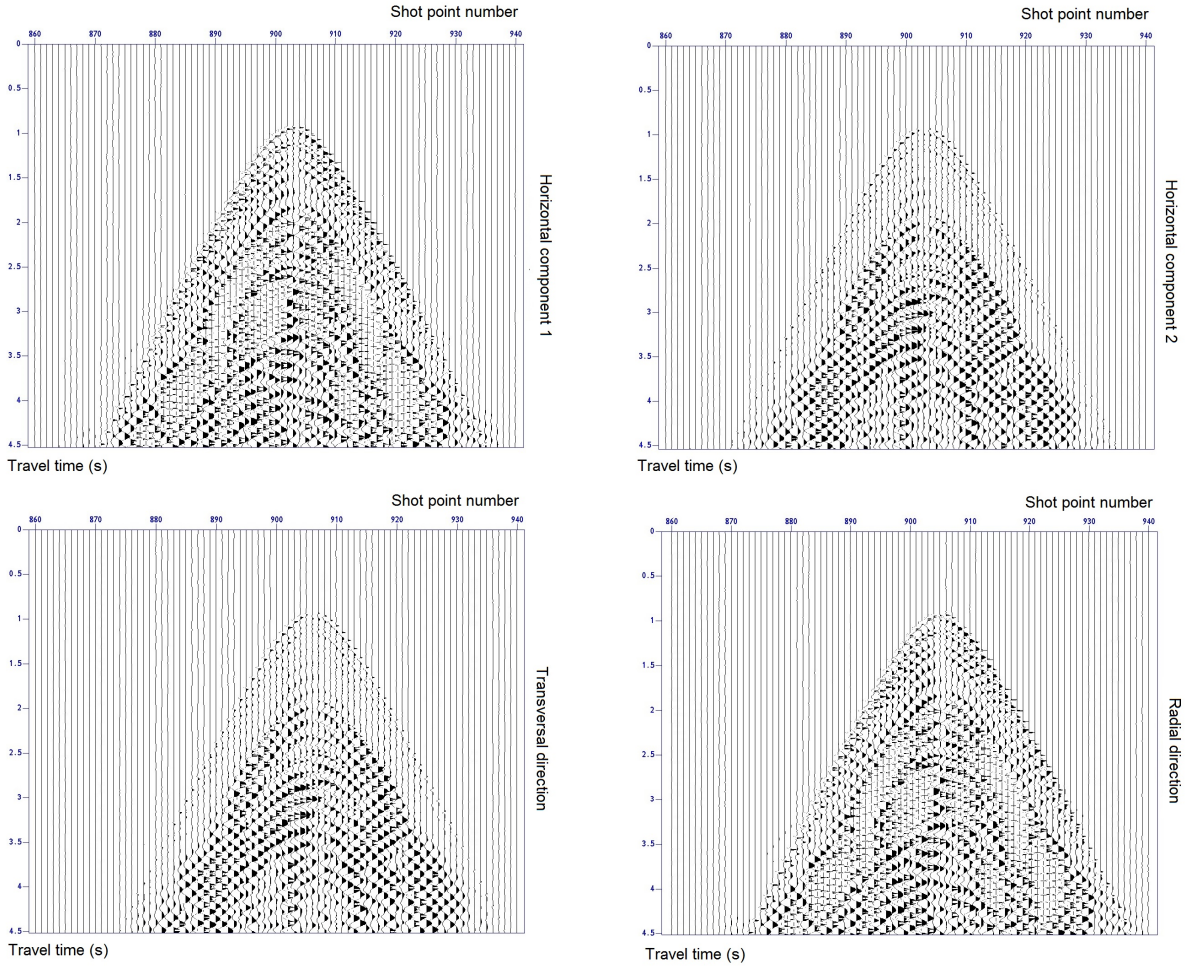

Figure 4.11: Rotation of horizontal components (OBS 3). Upper receiver gathers are horizontal component one and two. The lower two gathers are rotated with an angle of 203^0, with the transversal direction on the left side and the radial direction on the right side.

4.3.3 Work flow - Radial component

The radial component was processed in much the same way as the vertical component. However two versions was made of each radial component, one with velocity reduction equal 8.0 km/s and one with 4.6 km/s. 4.6 km/s should approximate the S-wave velocity in the upper mantle, and it should be a convenient way to present arrivals of PSS-waves. These are refractions that convert on the way downwards and turn as S-waves. PPS-waves, waves that turn as P-waves and convert on the way up, should best be identified with a 8.0 km/s velocity reduction. The results of processing OBS 1 with both 8.0 km/s and 4.6 km/s velocity reduction are displayed in Figure 4.12. In Appendix B.2 processed radial components are displayed together with results from velocity modeling.

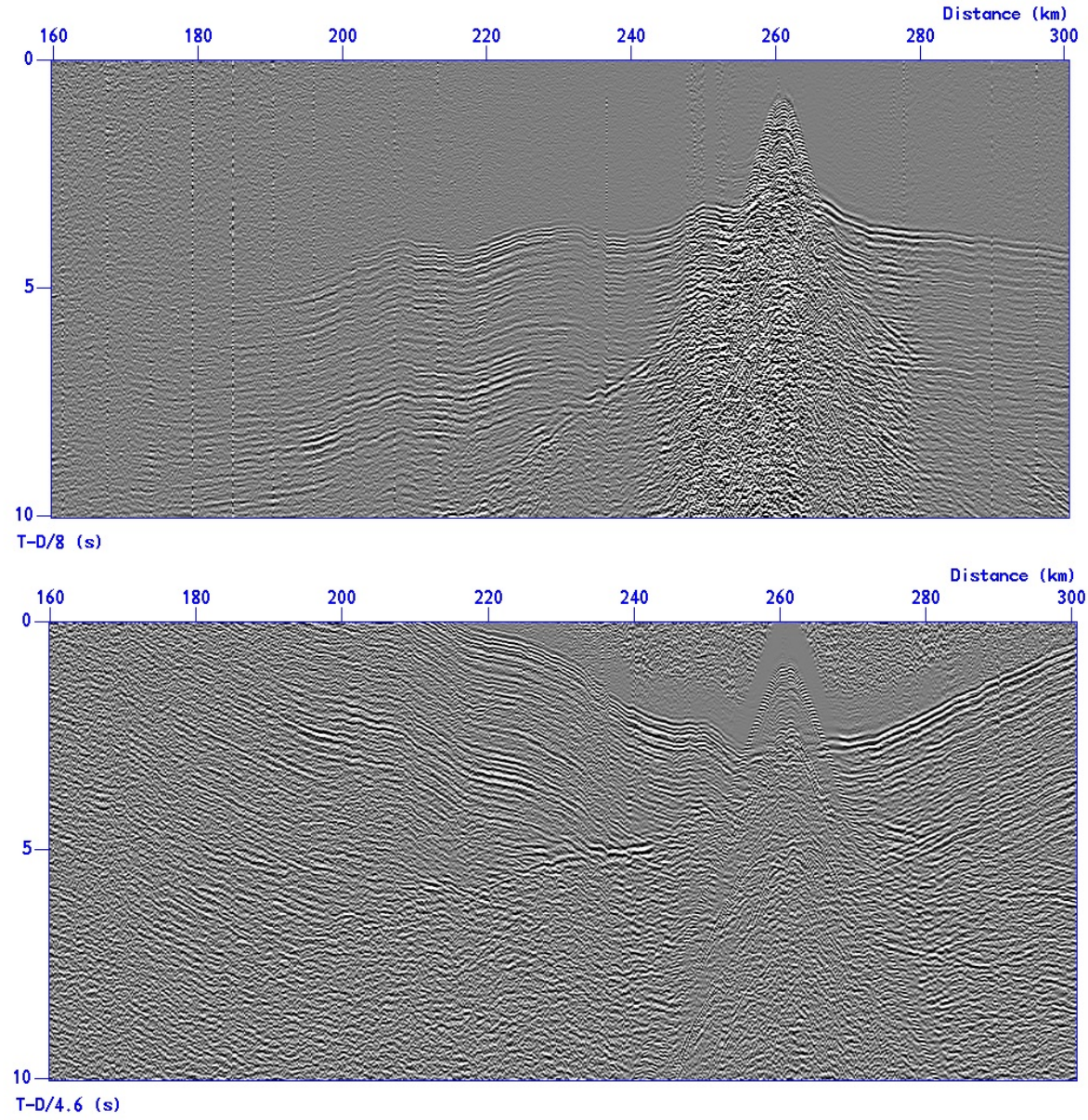

Figure 4.12: Radial component of OBS 1 after applied work flow. Data in upper image has a velocity reduction of 8.0 km/s and is used for identifying PPS-arrivals. Data in the lower image has a velocity reduction of 4.6 km/s and is used for identifying PSS-arrivals.

Chapter 5

Single-Channel Streamer

297 km of recording was available from the single-channel streamer (SCS). A few pre-stack filters were included into the work-flow for enhancing the S/N ratio and removing source reverberation. Only one zero-offset trace is acquired for each shot. Advanced processing requiring central mid point sorting, is prevented by the simple nature of the data set. The work flow applied in Seismic Unix is presented in Table 5.1. The final result is presented in Figure 5.1.

Table 5.1: Seismic Unix work flow for SCS data.

```
$ cat unprocessed_data.su | \
  sugain mbal=1 | \                 # Gain
  supef maxlag=0.35 | \             # Spiking deconvolution
  sufilter f=5,20,40,60 | \         # Band-pass filter
  sugain tpow=1.2 | \               # Amplitude corrections
  > processed_data.su
```

Gain is applied two separate times, in the very beginning and at the end. First it is applied for balancing traces by subtraction of the mean. The second time it is applied for data independent amplitude corrections, which is done by multiplication with a factor $t^{1.2}$. "t" equals the two way travel time. The exponential factor "1.2" is chosen empirically, or simply through trail and error. It corrects for amplitude loss as a result of attenuation.

Reverberation and ringing seen in the dataset was removed by compressing the pulse with spiking deconvolution. The gap length was set equal the sampling interval (supef-default: minlag=dt). The system wavelength was approximated with 350 microseconds (maxlag=0.35). A relative additive noise level was added (supef-default: pnoise=0.001). The same reasoning was used as during processing of the OBS data (see also Section 4.2.1).

A band pass filter was applied, with 5/20/40/60 Hz representing the low cut / low pass / high pass / high cut frequencies, respectively. This filter should eliminate high and low frequency noise. As discussed during processing of the OBS data (see also Section 4.2.1), seismic disturbance is commonly found in the range 0-3 Hz while equipment noise is found above 50 Hz. Such a band-pass filter should be able to preserve the interesting parts of the source's frequency

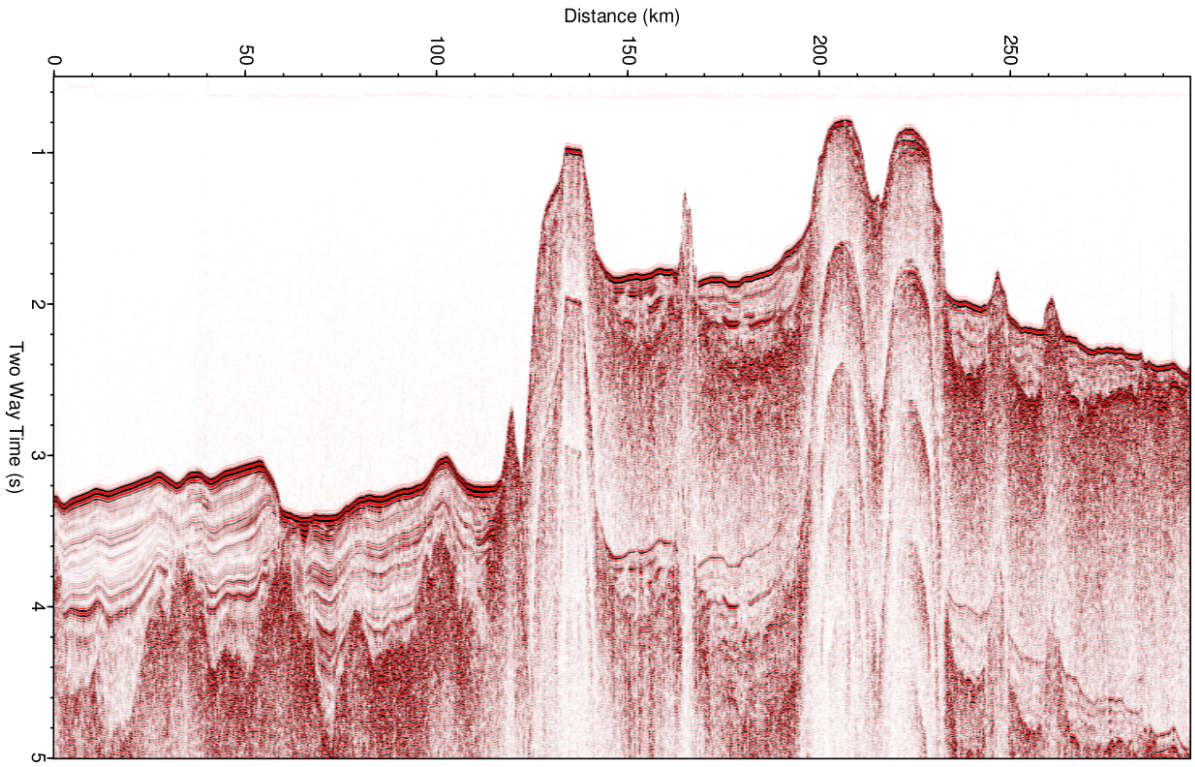

Figure 5.1: Single-channel streamer profile. Processed with gain, spiking deconvolution, band-pass filter and amplitude corrections. A clearly visible contrast is obtained between the sedimentary layers and the basement.

content, as discussed and presented in Figure 3.1 in Section 3.2. In comparison with the band-pass filter applied to the OBS data, here much higher high pass and high cut frequencies are chosen. This is because only zero-offset arrivals will be evaluated in the SCS data, i.e. only waves that have undergone much less attenuation compared to the far offset phases in the OBS data.

A prominent and clear contrast is obtained between the sedimentary layers and the basement. Furthermore, layering within the sedimentary unit can be observed. Clearly visible sea bottom multiples are present in the profile. These can not be removed. However, they do not cause any complications as they arrive later than the interface between the sedimentary unit and the top basement.

Part III

Velocity Modeling

Chapter 6

Theoretical Backgroud

6.1 Seismic body waves

6.1.1 Displacement and velocity

Sound waves propagating within a medium are called body waves. If the medium is linearly elastic, homogeneous and isotropic, wave motion can be idealized as a plane wave. This is an approximation often assumed for seismic waves, which then can be separated into two categories defined from their particle displacement relative to the direction of propagation; pressure- and shear waves. When written more compactly they are referred to as P- and S-waves. P-waves has displacement in the same direction as the propagation while s-waves has displacement perpendicular to this. Their velocities, "v_p" and "v_s", can be described from two medium characteristic elastic modulus and the density of the medium "ρ". The elastic bulk and shear modulus are written as "k" and "μ", respectively.

$$v_p = \sqrt{\frac{k + \frac{4\mu}{3}}{\rho}} \qquad v_s = \sqrt{\frac{\mu}{\rho}} \tag{6.1}$$

6.1.2 Kinematic ray theory

An high frequency approximation to the solution of the wave equation can be used to achieve a ray tracing approach to wave propagation (Virieux, 1996). With high frequency it is assumed that the travel time "T" is much greater than the time length of the seismic pulse "t", i.e. the wavelength of the propagating signal is much smaller than any spatial features associated with heterogeneities.

High frequency approximation: T/t » 1

Huygens' principle states that the evolution of a wavefront can be geometrically constructed through superposition of secondary wavelets, which can be obtained through sampling of the whole medium. If one instead focuses on trajectories orthogonal to the wavefronts at each point, the necessity of sampling the whole medium can be avoided. The ability to focus solely on a single ray, is the advantage of the high frequency approximation to the wave equation solution.

Kinematic ray theory can be expressed in terms of a system of first-order differential equations.

$$\frac{d\mathbf{x}}{ds} = c(\mathbf{x})\,\mathbf{p} \qquad \frac{d\mathbf{p}}{ds} = \nabla\frac{1}{c(\mathbf{x})} \tag{6.2}$$

Under the following constraint: |p| = 1/c

$\mathbf{x}$: Position vector

$\mathbf{p}$: Slowness vector

s: Ray path

$c(\mathbf{x})$: Isotropic propagation velocity

Some wave types can are not included in the kinematic ray theory approximations, e.g. caustics, diffraction and interference head waves. Special considerations is needed if such waves are to be included.

6.1.3 Conversion of waves

At the interface between two elastic medium, coupling exists between P- and S-waves, i.e. wave energy of the one type can be converted into wave energy of the other type. In the general case, polarization of S-wave displacement can be in any direction perpendicular to the propagation. However, during conversion at an interface, only waves polarized in vertical and radial direction are generated. This comes from the components of the traction across the interface which are restricted in these direction. S-waves that are vertically polarized are commonly denoted SV-waves. These will be orientated in a radial direction when converted at an interface between a source and a receiver. In this study SV-waves will for simplicity be referred to as S-waves. SH-waves are horizontally polarized and will nor be generated by conversion at an interface, as they would be orientated in the transversal direction. This is an assumption based on strictly in-line propagation in a medium uniform in the cross-line direction. Real world examples would of course be more complex.

The nature of conversion depends on the acoustic impedance contrast across the interface, as well as the incidence angle and type of incident wave. Figure 6.1 displays the amplitude variation as a function of incidence angle for a down going P-wave. The interface approximates the Moho between lower oceanic crust and upper mantle. Calculations are based on Zoeppritz' equations (Zoeppritz, 1919).

6.1.4 Snell's law

Across velocity discontinuities paths of reflected and transmitted waves are bent according to Snell's law. The ray parameter, i.e. the apparent horizontal velocity, is constant along a ray path. This is true for non-converted as well as converted waves. The geometry of ray paths across an interface is displayed in Figure 6.2. "i" and "j" gives the deviation in degrees from the vertical for the P- and S-waves, respectively. "α" and "β" are the P- and S-wave velocities.

Index indicate layer. "p" is the ray parameter and "c_x" is the apparent horizontal velocity.

$$p = \frac{1}{c_x} = \frac{sin\, i_1}{\alpha_1} = \frac{sin\, i_2}{\alpha_2} = \frac{sin\, j_1}{\beta_1} = \frac{sin\, j_2}{\beta_2} \tag{6.3}$$

6.1.5 Travel time curves

Waves follow paths that depend on the velocity structure of the media in which it travels. If "S" is the wave path made up of small segments "s", the travel time "t(s)" along the path can be written as the line integral of the velocity "v(s)" along the path.

$$t(s) = \int_S \frac{1}{v(s)}\, \mathrm{d}s \tag{6.4}$$

Solving the equations of kinematic ray theory for layers of constant velocities, rectilinear propagation within each layer is obtained. For simple geometries like an horizontally layered subsurface, equations describing the different wave paths can be deduced. Only non-converted waves are presented in this section. Reflected waves are hyperbolas while direct and head waves are linear. The slope of the linear curves will be equal the reciprocal of the internal layer velocity. In Figure 6.3 the travel times as a function of offset, "t(x)", for these three wave types are presented for an idealized two laye over an half-space model. The equations describing the curves, i.e. phases, are presented below for one layer over an half-space. "h_0" is the thickness of the top layer.

$$t_{Direct} = \frac{x}{v_0} \tag{6.5a}$$

$$t^2_{Reflected} = \frac{x^2}{{v_0}^2} + 4\frac{{h_0}^2}{{v_0}^2} \tag{6.5b}$$

$$t_{Head} = \frac{x}{v_1} + \tau_1 \qquad \text{where } \tau_1 = 2h_0\sqrt{\tfrac{1}{{v_0}^2} - \tfrac{1}{{v_1}^2}} \tag{6.5c}$$

"τ_1" is the intercept time, an extrapolation of the head wave curve giving its imaginary zero-offset time. The head wave actually first appears on the plot at the critical distance "$x_c = 2h_0 tan(i_c)$", where "$i_c = arcsin(v_0/v_1)$" is the critical angle. Another important distance is the cross over distance where the direct and the first head wave arrive at the same time, "$x_d = 2h_0\sqrt{(v_1 + v_0)/(v_1 - v_0)}$".

In a situation as simple as the one described above, the inverse problem of finding the velocity structure with depth can be achieved from looking at the arrivals in the travel time plot. Analytical solutions are also possible in simple geometries, for example planar dipping horizons (e.g., Stein and Wysession, 2003), as well as in certain non-constant velocity structures (e.g., Virieux, 1996). However, when analyzing more complex structures numerical calculation is necessary.

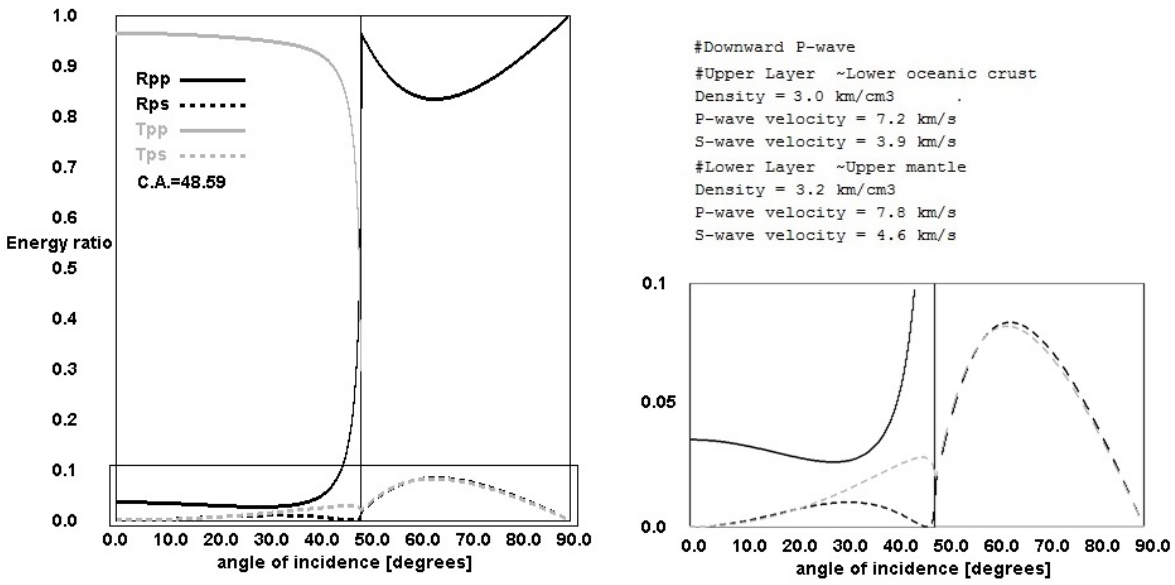

Figure 6.1: Variation in reflected and transmitted wave energy for converted and non-converted waves. The interface approximates the Moho, between the lower oceanic crust and the upper mantle. Calculations are for a down going P-wave, based on Zoeppritz (1919). Plotting was done with CREWES (2005). A zoom window of energy ratio 0 – 0.1 is enlarged on the right side. Rpp: Reflected P-wave. Rps: Reflected S-wave. Tpp: Transmitted P-wave. Tps: Transmitted S-wave. Vertical line at 48.6^0 marks the critical angle. At angles higher than the critical, no P-wave energy is transmitted.

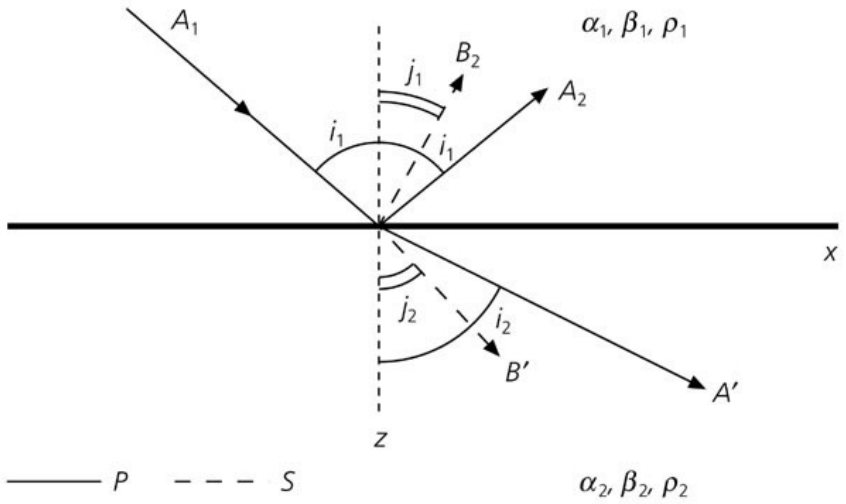

Figure 6.2: Reflection and transmission angles at interface. Image is from Stein and Wysession (2003)

Nevertheless, identification of phases is still done manually through geometrical evaluation of their arrival in the travel time plot. The geometry of the phases, as presented for homogeneous velocities and flat layers is used as reference during identification of wave-arrivals.

In a velocity structure with linear gradients, a refracted wave will appear with a similar travel time curve as an head wave. A reflected wave will still display an hyperbolic shape.

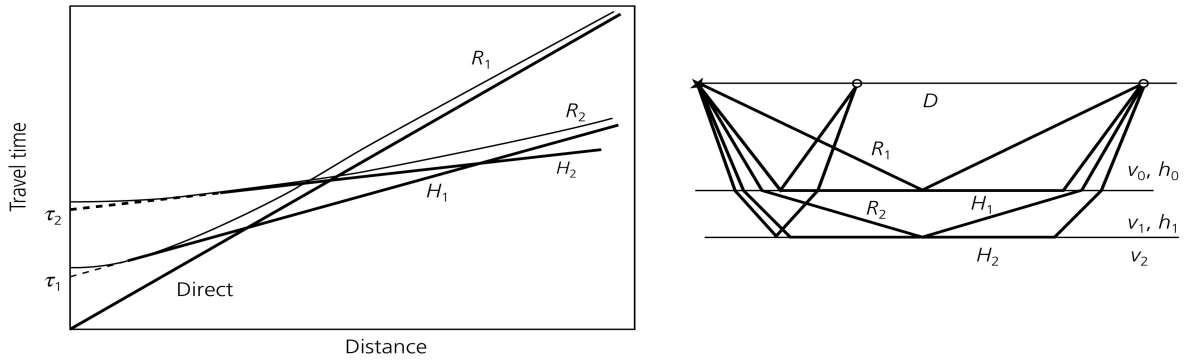

Figure 6.3: Travel time plot of direct (D), reflected (R) and head (H) waves in constant velocity layers. Image from Stein and Wysession (2003).

6.1.6 Amplitudes

The amplitude of a wave decays as a function of distance from the source. This is a result of intrinsic attenuation and geometrical spreading, as well as transmission losses at interfaces. The nature of seismic propagation is such that higher frequencies get more easily attenuated than lower ones. Gelius and Johansen (2010) presents an estimate to the amplitude decay of a body wave as a result from geometrical spreading and intrinsic attenuation:

$$\frac{A}{A_0} = \frac{r_0}{r} e^{-\alpha(r-r_0)} \qquad \text{where } \alpha = \frac{\pi f_0}{Qv} \tag{6.6}$$

A,r: Amplitude and distance of wavefront
A_0, r_0: Amplitude and distance of reference wavefront
f_0: Center frequency of seismic pulse
Q: Lithology dependent quality factor
v: Medium velocity

At long distances the amplitude of a refracted wave will be greater than that of an head wave (e.g., pp 153 in Fowler, 2005). At distances much greater than the critical distance, the amplitude of an head wave will decay with "r^{-2}", while a refracted wave will decay normally as a body wave, proportional to "r^{-1}". Hence, in velocity modeling of wide angle seismic, refracted waves are commonly preferable over head waves.

6.2 Basis for interpretating seismic velocities

6.2.1 Poisson's ratio and lithology considerations

The Poisson's ratio is an elastic modulus describing the characteristics of volumetric change in a medium under applied stress. It is defined as the negative ratio of transverse to axial strain, which relates directly to the elastic properties of a medium. In a linear elastic and isotropic medium, Poisson's ratio can be expressed as a function of the medium velocities alone.

$$\nu = -\frac{e_{trans}}{e_{axial}} = \frac{1}{2}\left(1 - \frac{1}{(v_p/v_s)^2 - 1}\right) \tag{6.7}$$

Theoretically Poisson's ratio varies between -1 and 0.5 (Gercek, 2007), but among rocks in nature it typically varies in between 0 and 0.5. Materials with negative values, denoted auxetic materials, are rare among rocks in nature as such rocks undergoes contraction in its transversal directions during compression along it's longitudinal axis. Nevertheless, it has been observed for some single crystals during compression and extension in certain directions (Christensen, 1996). Fluids without rigidity, $\mu = 0$, have a Poisson's ratio of 0.5.

It is possible to use Poisson's ratio to identify lithology in crustal studies (Au and Clowes, 1984; Christensen, 1996, 2004). Christensen (1996) argue how the Poisson's ratio of rocks at considerable high pressure, sufficient high to eliminate porosity effects, is related to the volume percentages of its mineral content. Christensen (1996) states further that Poisson's ratio should be consistent for lithologies over a wide range of crustal depth. For compacted non porous rocks, change in pressure and temperature does not affect the Poisson's ratio significantly.

Figure 6.4 display some of the major of Poisson's ratios for a selection of lithologies. Based on Christensen (1996) a few general trends will be mentioned. Quartz rich and felsic rocks have a generally low Poisson's ratio, e.g. quartzite has a value of 0.10. Mafic rocks generally have normal to high values, in between 0.25 and 0.30. Continental and oceanic crust should to a certain degree display different ratios, with average values having been estimated to 0.265 and 0.30, respectively. Anisotropy is not accounted for in the deduction of Equation 6.7. Anisotropy caused by mineral orientation, aligned fracturing or little compacted shallow units, could yield varying results of Poisson's ratio. For extrusive volcanic rocks with a great amount of porosity, voids, glass etc., Poisson's ratio should be used with care. On the other hand, for plutonic igneous rocks the Poisson's ratio is generally consistent and can be used to indicate lithology. Poisson's ratio increases as Fe is substituted for Mg in olivine and pyroxene. Serpentinization gives a high value of Poisson's ratio. This metamorphic facies is often present at fractured and rifted oceanic crust, e.g. especially in fracture zones.

6.2.2 Velocity distribution in normal oceanic crust

Normal oceanic crust has a very typical composition, made form basaltic magma upwelling at mid ocean ridges. This has been determined from seismic exploration and ocean drilling, as well as studies of on-land exposed ophiolites. A brief review of the main layering in the ocean-

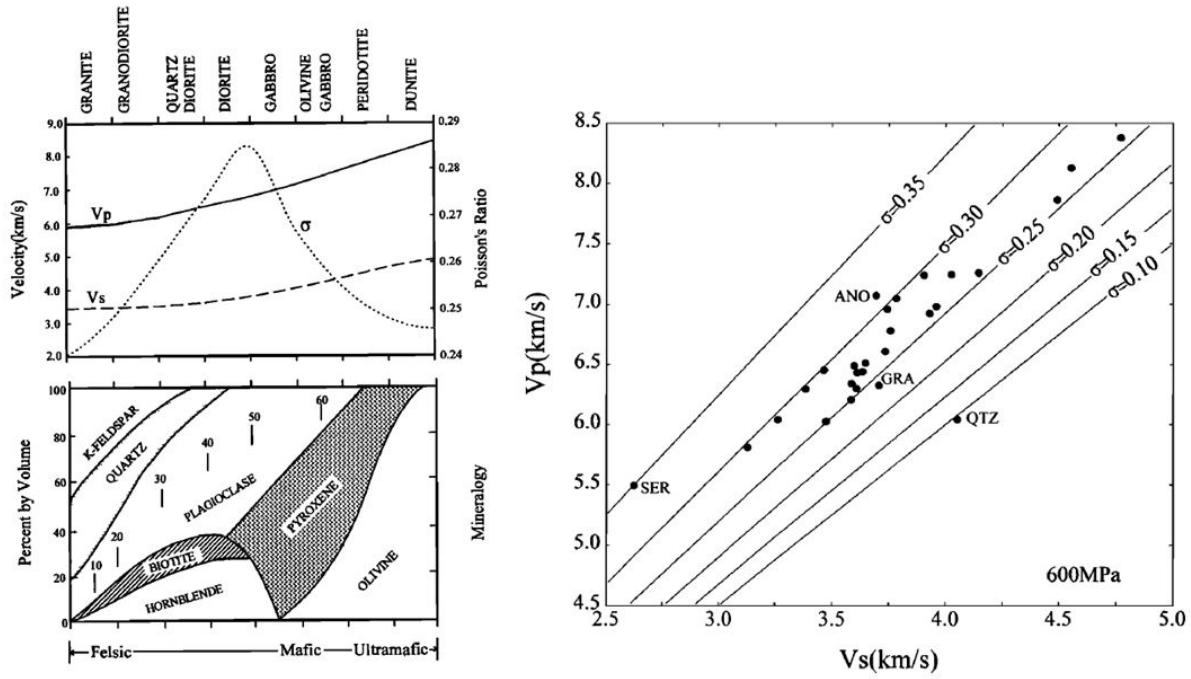

Figure 6.4: Left: Variation in Poisson's ratio as a function of mineralogic content for felsic to ultramafic intrusive rocks. Right: Distribution of Poisson's ratio for common rocks. Anomalous values outside 0.25 and 0.30 are observed for serpentinite (SER), anorthosite (ANO), granite-granodiorite (GRA), and quartzite (QTZ)). Figures are from Christensen (1996).

tic crust, with corresponding thickness and velocity (e.g., Fowler, 2005; Stein and Wysession, 2003), is given in this section. Table 6.1 lists average values from White (1992).

Table 6.1: Average velocity distribution in oceanic crust (White, 1992).

	Thickness (km)	Velocity (km/s)
Sedimentary layer	0.5	2.0
Volcanic layer	1.6-2.6	2.5 - 6.6
Oceanic layer	4.0 - 5.9	6.6 - 7.6
Upper mantle		7.9 - 8.1

Typically, the oceanic crust can be divided into four main layers. The uppermost layer is the sedimentary layer, with an average thickness of 0.5 km. Typical velocity is 2.0 km/s. Layer number two is the volcanic layer which in turn can be subdivided into two parts, layer 2A and 2B. 2A, the upper layer, is of extrusive nature made up of volcanic material commonly referred to as pillow lavas. The lower part, 2B, is made up of intrusive volcanic rocks, and the layer consists of a sheeted dike complex. The extrusive rocks are variable with regards to velocity, with a high velocity gradient. On the very top of the layer velocities can be around 3 km/s while at the bottom they increased to about 5 km/s. The sheeted dike complex typically has velocities about 5 - 6 km/s. The total thickness of both layer 2A and 2B is 2 – 3 km thick. The third

layer consists of Gabbros. Average thickness is 5 km and average velocity is 7 km/s. The seismic boundary between the crust and the mantle is marked by the Mohorovicic discontinuity, an abrupt increase in velocity to around 8 km/s. The uppermost mantle is typically made up from ultramafic rocks dominated by peridotites.

Chapter 7

Modeling Specifications

7.1 Modeling strategy

The desired results of modeling wide-angle seismic is a velocity model that predicts the observed travel times. Zelt (1999) argues how there's no single approach of how to best model ocean bottom seismometer (OBS) data. Different considerations are necessary depending on the OBS coverage, the data quality, amount of prior information which can be incorporated into the model, the geometry of the earth structure, etc. Various inversion methods are available for creating a minimum-structure model, that is a tomographic approach. For big data sets with dense coverage, inversion would yield the simplest model that best fit all the data. In this study, however, a small data set with sparse OBS coverage along the profile was analyzed. A forward modeling approach was chosen, to facilitate trial-and-error phase identification. In Figure 7.1 an outline of the modeling procedure is presented.

First of all a starting model was made. It included prior information from the uppermost part of the crust, i.e. the seabed depth, an estimate of the velocities within the sedimentary unit and the depth to the top basement horizon. Then the subsurface layers below were developed through a top to bottom, layer by layer, approach. That is, seismic phases was used to first constrain shallow structures, before progressively continuing into deeper layers. Following this procedure from top to bottom, the model was in the end constrained into a few layers with distinct seismic properties, which may or may not correspond to geological boundaries.

Modeling of wide-angle seismic contain non-unique solutions. That is, a particular dataset is covered by a range of models. A final model has to be chosen according to certain criteria. It should be possible to trace rays to as many as possible of the observed travel time picks. The travel time residual, the fit between the observed and calculated travel times, should be minimized. An heuristic approach based on geological intuition was considered important when deducing the model structures. At the same time, a minimum model should be preferred. Following the principle of Occam's razor, the model containing fewest assumptions should be selected. More complicated models may ultimately prove correct, but -in the absence of certainty of any additional complexity- a less complicated model is preferred. To address the problem of non-uniqueness and model complexity, two independent models were derived simultaneously,

Figure 7.1: Chosen procedure of making velocity model. The two-way arrow tells that despite identification and picking of phases was done first, adjustments was again made after having modeled with Rayinvr. The two steps were repeated numerous times.

where one of the model contained one extra layer.

In the OBS data it can be difficult to separate true phase arrivals from patterns caused by noise, both ambient and coherent noise. Especially at far offsets and among not-first arrivals identification of phases can be difficult. It was believed that a restrained approach of phase picking would yield the most correct results. That is, if an unsure phase would require more complex structures, it was assumed that it would be more correct to present a simpler model. Phases that could not be incorporated with certainty, e.g. unsure phases with very poor fit, were not incorporated into the model.

After completion of forward modeling, phase picks were re-sampled into 0.2 km intervals.

This was done to normalize the weight each phase would contain in quantitative evaluations. A damped least-square inversion routine (Zelt and Smith, 1992) was then applied to the model. Inversion was done to further adjust the velocity structure to the observed data, but maintaining the gross structures of the obtained model. Small-scale changes of boundary depths and velocity values were done to better fit the model's predicted travel times with the observed travel times in the data.

The S-wave velocities were fitted into the structures of the P-wave model, assigning one value of Poisson's ratio to each layer. In each layer the S-wave velocity is directly related to the P-wave velocity. No additional adjustment for lateral or vertical velocity variation was done, nor was any inversion routine applied. This do not necessarily give an exact S-wave velocity structure, but it nevertheless approximates one value of Poisson's ratio for each layer. A less restrained approach was used for including S-waves, as including a a wrong S-wave would only affect the data fit and possibly the value of Poisson's ratio. But the model framework, previously determined by the P-waves, would not change.

Two separate models were modeled independently to evaluate what structure was indeed predicted by the data. To compare these two, statistics of data fit (see Section 7.2.4) as well as heuristic considerations were evaluated.

A few quantitative measurements were used to address the quality of the final model. In addition to statistics of data fit, the ray coverage was assessed to evaluate how well different parts of the model had been resolved (see Section 7.2.5). Parameter perturbation was done to test uncertainties of model features, as layer boundaries and bulk layer velocity (see Section 8.5).

7.2 Rayinvr software

Modeling of the data was done with the software package Rayinvr, a ray tracing routine developed by Zelt and Ellis (1988). An inversion method later added by Zelt and Smith (1992). It is a collection of programs that can be used for 2-D travel time analysis. In this section program specifications related to forward modeling and the damped least-square inversion routine are reviewed.

7.2.1 Parameterization

A 2D velocity model is composed of a sequence of layers. Each layer boundary is defined by an arbitrary number of boundary nodes connected by linear interpolation. An arbitrary number of velocity nodes define the upper and lower velocity inside each layer. Velocity varies linearly between velocity points located on layer boundaries. To achieve interpolation in both horizontal and vertical direction, each layer is divided laterally into an irregular network of trapezoidal blocks separated by vertical boundaries. These are included automatically wherever there is an upper or lower layer boundary or velocity node. This way, the velocity field varies linearly with position along the four sides of a trapezoid, Figure 7.2.

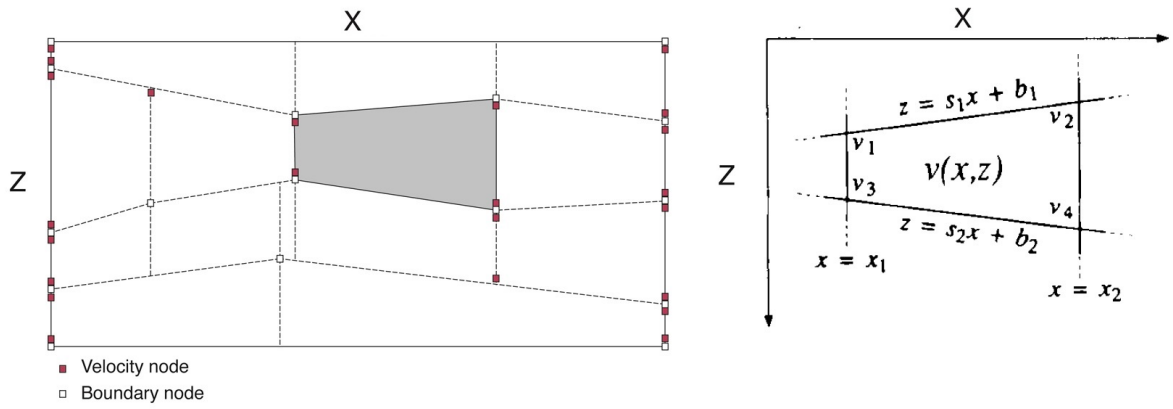

Figure 7.2: Model parametrization. To the left is a visualization of the irregular network of trapezoids, defined by velocity and boundary nodes, making up the 2D model. To the right is a image showing linear interpolation of velocity in a trapezoid. Images are from Zelt and Smith (1992).

A trapezoid with four boundaries in the x-z plane is defined by:

$$x = x_1\,,\ x = x_2\,,\ z_1 = s_1 x + b_1\,,\ z_2 = s_2 x + b_2\,, \tag{7.1}$$

Defined by the four corner velocities v_1, v_2, v_3 and v_4, the velocity $v(x, z)$ within the trapezoid is:

$$v(x,z) = \frac{c_1 x + c_2 x^2 + c_3 z + c_4 xz + c_5}{c_6 x + c_7} \tag{7.2}$$

Where c_i are linear combinations of the corner velocities.

$$\begin{aligned}
c_1 &= s_2(x_2 v_1 - x_1 v_2) + b_2(v_2 - v_1) - s_1(x_2 v_3 - x_1 v_4) - b_1(v_4 - v_3) \\
c_2 &= s_2(v_2 - v_1) - s_1(v_4 - v_3) \\
c_3 &= x_1 v_2 - x_2 v_1 + x_2 v_3 - x_1 v_4 \\
c_4 &= v_1 - v_2 + v_4 - v_3 \\
c_5 &= b_2(x_2 v_1 - x_1 v_2) - b_1(x_2 v_3 - x_1 v_4) \\
c_6 &= (s_2 - s_1)(x_2 - x_1) \\
c_7 &= (b_2 - b_1)(x_2 - x_1)
\end{aligned}$$

The parameterization also allows for layer pinch-outs and isolated bodies to be included in the model. When a layer is reduced to zero thickness, the adjacent trapezoids will be reduced to a three-sided block, with its velocity field defined by three corner velocities instead of four.

7.2.2 Ray tracing

Using the high frequency approximation as described in Section 6.1.2, travel times and ray paths through a velocity model can be calculated by solving the ray tracing equations numerically.

The 2-D ray tracing equations are a pair of first-order differential equations.

$$\frac{dz}{dx} = cotan\,\theta\ , \qquad \frac{d\theta}{dx} = \frac{\frac{\partial v}{\partial z} - \frac{\partial v}{\partial x}\ cotan\,\theta}{v} \tag{7.3a}$$

$$\frac{dx}{dz} = tan\,\theta\ , \qquad \frac{d\theta}{dz} = \frac{\frac{\partial v}{\partial z}\ tan\,\theta - \frac{\partial v}{\partial x}}{v} \tag{7.3b}$$

with initial conditions $x = x_0$, $z = z_0$ and $\theta = \theta_0$.

The source location is at (x_0, z_0). θ_0 is the ray take off angle. Equations 7.3a are solved with x as an integration variable when ray path is nearly-horizontal and Equations 7.3b with z when nearly-vertical. The system is solved by a Runga-Kutta method with error control.

A ray step length Δ, used in solving Equations 7.3a and b, is an increment for the ray in either the x or z direction. It is adjusted at each point along the ray path according to the change in horizontal and vertical velocity to avoid unnecessary small or inaccurate large steps.

$$\Delta = \frac{\alpha v}{|\frac{\partial v}{\partial x}| + |\frac{\partial v}{\partial z}|} \tag{7.4}$$

α = 0.05: User specified constant.

A ray group is as a set of rays that have turning or reflection points in the same layer. When rays are traced through the specified model, only specific types of wave groups are considered. Figure 7.3 shows examples of the different groups considered in Rayinvr. The most important for this study are refracted and reflected. However, when determining S-wave velocities converted wave groups are modeled. Diffractions, caustics and interference head waves are not incorporated into the high frequency ray theory, and can not be modeled. Floating reflectors can be put into the model, giving a reflector without the need of a layer boundary with a velocity difference across. The software can handle multiples and zero offset-reflections, though such waves were not evaluated in this study.

7.2.3 Damped least-squares inversion routine

The software package contains an inversion routine which can adjust a set of selected velocity and/or boundary nodes.

The travel time "t" along "n" sets of ray path segments "s_i" with corresponding velocities "v_i" can be written as:

$$t = \sum_{i=1}^{n} \frac{s_i}{v_i} \tag{7.5}$$

Inversion of travel time is a non-linear problem. A solution will be approximated by linearizing the above equation using a Taylor series about a starting model, while disregarding higher order

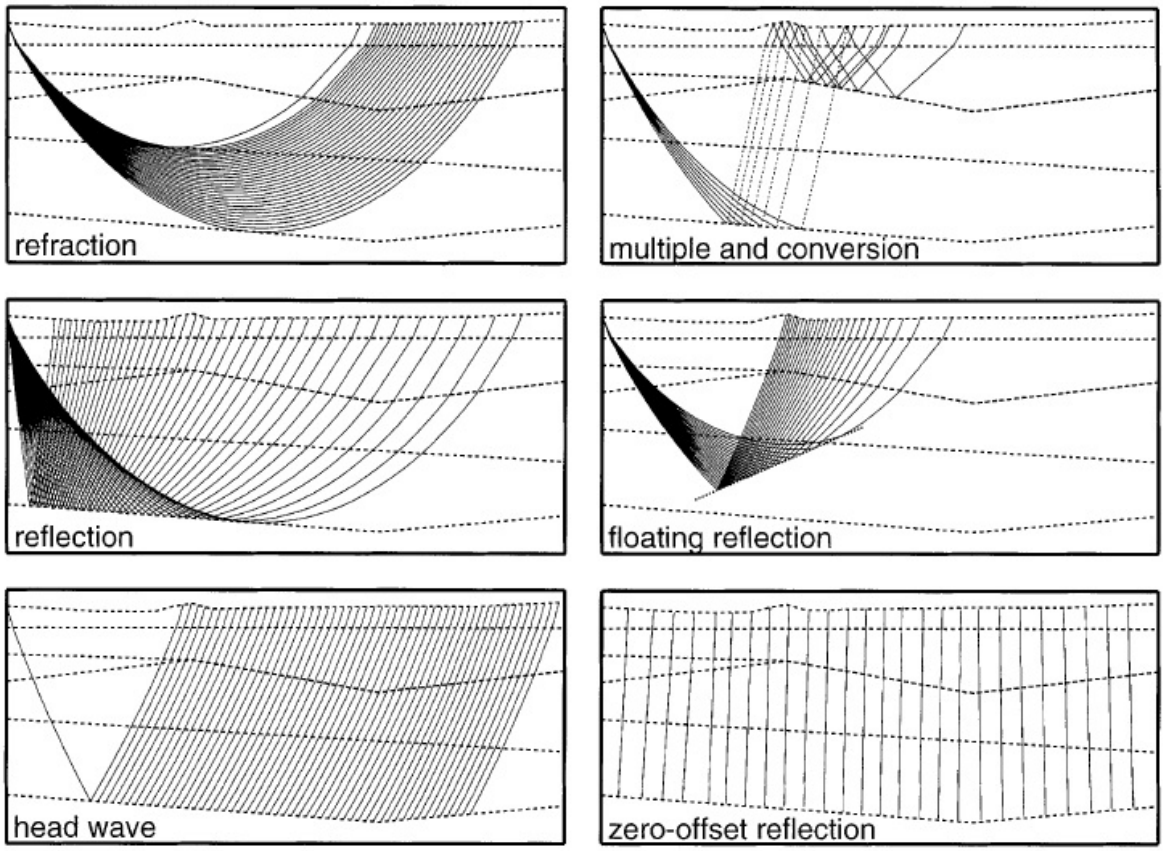

Figure 7.3: Examples of ray groups considered in Rayinvr. Image is from Zelt (1999).

terms.

$$\Delta t_i = A_{ij} \Delta m_j \tag{7.6}$$

Δt_i: Travel time residual vector
Δm_j: Model perturbation vector
$A_{ij} = \frac{\partial t_i}{\partial m_j}$: Partial derivative matrix

Generally there are more ray paths than unknown model parameters, which makes the systems of equations overdetermined. The equations are solved through a weighted damped least-square solution:

$$\Delta m_i = (A_{ji} W_t^{-1} A_{ij} + D W_m^{-1})^{-1} A_{ji} W_t^{-1} \Delta t_i \tag{7.7}$$

The equation is weighted by W_t and W_m, which are identity matrices with diagonal components "$\sigma_{t,i}^2$" and "$\sigma_{m,j}^2$", respectively. That is, the diagonal components of the weighting matrices are squared estimates of uncertainties in the travel time picks and model parameters. The data with the smallest uncertainties will in this way have the greatest effect on the solution. The factor "D" is the empirical user specified damping factor, which determines the trade-off between resolution and the amount of adjustments to the model parameters, as well as the model parameters

uncertainties. D=0 gives the best fit solution. D > 0 damp -or reduce- the change in the model perturbation parameters, while compromising with a poorer fit to the data.

During ray tracing through forward modeling, both Δt_i and A_{ij} are calculated. The inversion routine then estimates Δm_j and applies it to the current model. Rays are then traced through the updated model to estimate the improved resolution.

7.2.4 Accuracy and goodness of fit

Estimates of how well the calculated travel time corresponds with the data is quantified by the root mean square (RMS) travel time residual and the chi-squared model parameter, χ^2.

Root mean square travel time residual:

$$\Delta t_{RMS} = \sqrt{\frac{\sum (y_i^{data} - y_i^{calc})^2}{n}} \tag{7.8}$$

Chi-squared value[1]:

$$\chi^2 = \frac{s^2}{< \sigma_i^2 >} = \frac{1}{\nu} \sum \left(\frac{y_i^{data} - y_i^{calc}}{\sigma_i} \right)^2 \tag{7.9a}$$

$$\text{Sample variance: } s^2 = \frac{1}{\nu} \sum \left(\frac{1/\sigma_i^2}{1/n \sum 1/\sigma_i^2} \right) \left(y_i^{data} - y_i^{calc} \right)^2 \tag{7.9b}$$

$$\text{Weighted average of data variance: } < \sigma_i^2 >= \left[\frac{1}{n} \sum \frac{1}{\sigma_i^2} \right]^{-1} \tag{7.9c}$$

y_i^{data}:	Travel time from data
y_i^{calc}:	Calculated travel time
σ_i:	Uncertainty of i-th pick
$\nu = n - k$:	Degrees of freedom
n:	Number of data ponts, i.e. number of traced rays
k:	Number of estimated data parameters: k=1

The variance of the samples is an estimate of the variance of the data. Division by degrees of freedom "ν" rather than number of data points "n" in Equation 7.9b, accounts for the number of parameters determined form the data. In forward modeling in Rayinvr the number of estimated data parameters is equal one. The single estimated parameter is time. χ^2 is the ratio of the sample variance to the weighted average of data variance. Hence χ^2 estimates how well these two

[1]Chi-squared is efficiently the reduced chi-squared as defined in some textbooks (e.g., pp 440 in Stein and Wysession (2003) and pp 194-195 in Bevington and Robinson (2003)), but in Rayinvr modeling it is commonly referred to as simply the chi-squared.

correlates. In Rayinvr, χ^2 is an estimate of how the residuals between the calculated and true travel times compares to the uncertainties of the phase picks, i.e. the data. While the variance of the data is characteristic of the spread of the data, the sample variance account for the accuracy of the fit as well the spread. χ^2 is a measurement describing the goodness of fit (Bevington and Robinson, 2003).

Ideally, a χ^2 value of unity is the desired result (Bevington and Robinson, 2003). A value higher than unity indicate a bad fit of the data, while a value lower than unity indicate over-fitting of the data. For example, if high uncertainties have been assigned to the phase picks with good fit, i.e. low RMS travel time residual, χ^2 gets an over-fitted value lower than unity.

Both of Δt_{RMS} and χ^2, as well as the number of traced rays, are calculated during forward modeling in Rayinvr. Values are calculated separately for each phase, which enables separate evaluation of the different phases. Whole model estimates are also estimated. The normalized chi-squared (χ^2_N) is the average between χ^2 of all phases, weighted with respect to number of rays per phase.

7.2.5 Resolution of model parameters

Model parameters are constrained by the ray coverage. A ray density plot will yield the spatial extent of sampled parameters. Furthermore, model parameters sampled by rays from different angles will be better constrained. The resolution matrix "R_{ij}" can be used as a measurement of the amount of constrain the ray geometry have on the model parameters.

$$R_{ij} = (A_{ji} W_t^{-1} A_{ij} + D W_m^{-1})^{-1} A_{ji} W_t^{-1} A_{ij} \tag{7.10}$$

The relationship between the true (although unknown) perturbation of model parameters "$\Delta m_i^{(true)}$" and the perturbation obtained from an inversion "$\Delta m_j^{(inv)}$" are given by:

$$\Delta m_i^{(inv)} = R_{ij}\, \Delta m_j^{(true)} \tag{7.11}$$

The elements in the resolution matrix range between zero and one, and indicate the degree of linear dependence of each model parameter. That is, how well an inverse problem could have been solved for perfect noise free data. In effect, the matrix indicate how well a certain model parameter is constrained by the ray geometry. When diagonal values of R are greater than or equal 0.5, they are in general regarded as well resolved and reliable (Zelt and Smith, 1992).

Chapter 8

Modeling Steps

8.1 Starting model

A starting model was made from integrating the sea floor topography and the interface between the sedimentary unit and the top basement. Sea floor depth was obtained from a echo-sounder recording, which was read directly from the survey navigation file. It was registered one depth reading for each shot. To be able to compare this information with the seismic data, the depth "Z" was converted to two-way travel time "t_{twt}".

$$t_{twt} = \frac{2Z}{\alpha_{water}} \ , \qquad \alpha_{water} = 1,483 m/s \tag{8.1}$$

One average water velocity of 1.483 km/s was assumed to be valid at all depths over the whole profile. To account for regional differences in sea water velocities and depth variations, an average value was calculated from Del Grosso's equation (Del Grosso, 1974). Averaging was done over the velocity profile until a depth of 2.5 km. Required input parameters as surface temperature and salinity were set to 2.0^0C and 35.0 ppt, respectively (National Oceanographic Data Center, 2013). A good fit was achieved between the survey depth reading and the seabed in the seismic profile.

The basement was identified in the single-channel streamer (SCS) data and a horizon was manually picked in Seismic Unix. The boundary between the sedimentary unit and the basement shows clearly two distinct seismic facies, see Figure 5.1 in Section 5, Part II. It was not given any attempts to correct for geometrical errors along the horizon in the SCS seismic. Within the sedimentary unit there are horizontal and layered reflectors, while the top basement has a granular look made up from high energy reflections. The SCS had recorded for shot number 32 – 1517 while the navigation file contain data for shot point number 1 – 1517. The basement was extrapolated 4 km from shot point 1 to 32, by simply using the same depth as at shot point 32.

Assumptions about velocity within the sedimentary unit is needed to convert the two way travel time to depth, as it was not possible to extract any information about this from the SCS data. In this study, sedimentary units on the Iceland Plateau, on top of the Eggvin Bank, in the JMFZ

and in the Greenland Basin will all be evaluated through the same velocity relationship. Approximating the upper most structures this way was considered to be sufficient for this study, as it would give a reasonable starting point for further mapping of the deep crustal structures.

Nearby investigations and empirical models can be assessed to help finding a suitable velocity model. A constant velocity of 2.0 km/s is commonly accepted as an average value in oceanic sediments (e.g., White, 1992). An approach was also done employing an empirical velocity-depth trend for deep sea sediments in the Norwegian-Greenland Sea (Myhre and Eldholm, 1981). A third attempt was to extract a velocity-depth trend from other nearby crustal studies conducted in the Greenland Basin (Voss et al., 2009; Kandilarov et al., 2012) and on the Iceland Plataeu (Kodaira et al., 1998), as well as across Jan Mayen Micro Continent (Kandilarov et al., 2012; Breivik et al., 2012). The average trend extracted from these studies corresponded well with mapped sedimentary velocities on the Greenland side of the Atlantic, as presented by Engen et al. (2006). The linear regression of sedimentary velocities is displayed in Figure 8.1. It was assumed that the sediments in these areas should there are similar to the sediments along the survey line in this study.

$$v_p = 2.0 \text{ km/s} \qquad \text{Average value (e.g., White, 1992)} \tag{8.2a}$$

$$v_p = 1.95 + 0.33Z \text{ km/s} \qquad \text{From Myhre and Eldholm (1981)} \tag{8.2b}$$

$$v_p = 1.8 + 0.7Z \text{ km/s} \qquad \text{Velocity-depth trend extracted from nearby studies} \tag{8.2c}$$

Lateral variation is expected from the findings of other nearby studies, but that would be too complicated to account for on the basis of the data set evaluated in this study. Kandilarov et al. (2012) mapped very high velocities in the vicinity of the Jan Mayen island, alongside the through of the JMFZ. They concluded it was because the sediments originated from the volcano itself. However, it was not be possible to investigate sedimentary velocities on the northern side of the fracture zone, as OBS 5 did not record during the survey. Hence, no effort was given to adjust for these possible higher velocities, as the lack of data coverage on the northern side makes a verification of such not possible.

Three different conversions are evaluated in Figure 8.2. They yield similar results for shallow depths, but differ for sedimentary thickness greater than half a kilometer. Constant velocity does not account for compaction of the sediments, i.e. depth conversion with a constant velocity is not preferred for thick sedimentary units. The velocity depth trend presented by Myhre and Eldholm (1981) and the one based on nearby studies give quite similar results. However, the later yields greater velocity with increasing depths, i.e. estimates a greater sedimentary thickness. Depth conversion differs up to 0.2 km at sedimentary thickness equal and greater than 1.5 km, and less than 0.1 km where the unit is less thick. In the end it was decided to use the velocity-depth trend in Equation 8.2c. It is assumed that the nearby studies can best account for the sedimentary properties found in the survey area. Nevertheless, it must be stressed that this velocity-depth trend is a rough estimate.

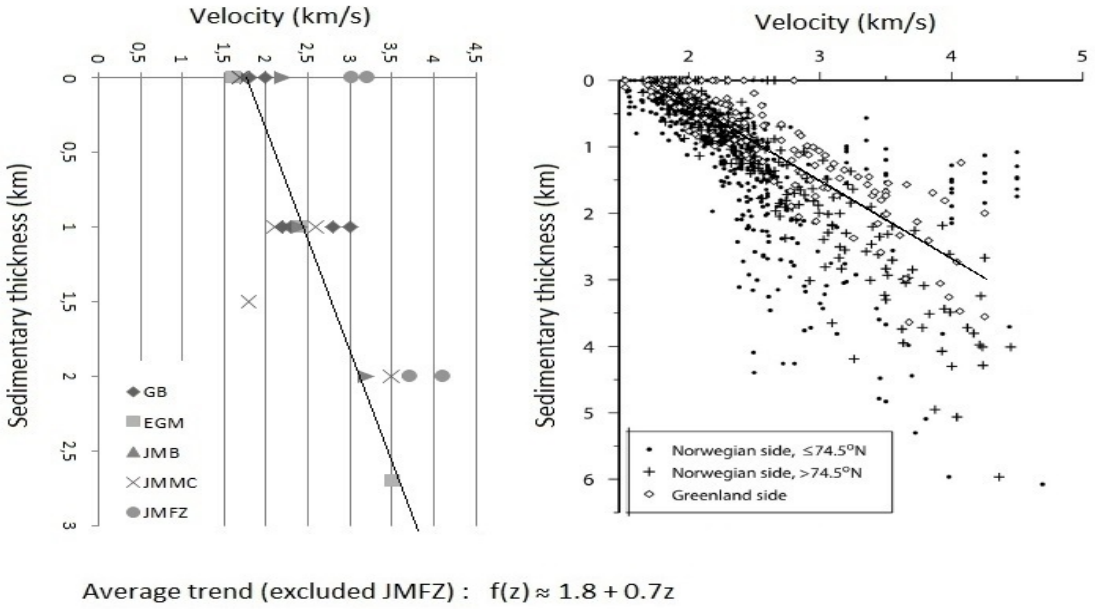

Figure 8.1: To the left: Extracted velocity-depth trend from nearby studies (Breivik et al., 2012; Kandilarov et al., 2012; Kodaira et al., 1998; Voss et al., 2009). GB: Greenland Basin. EGM: East Greenland margin. JMB: Jan Mayen Basin. JMMC: Jan Mayen Micro Continent. JMFZ: Jan Mayen Fracture Zone. To the right: Sedimentary velocities in the Atlantic ocean, as presented by Engen et al. (2006). "v_p = 1.8 + 0.7z" is plotted on top of the data to see how it compares with the study.

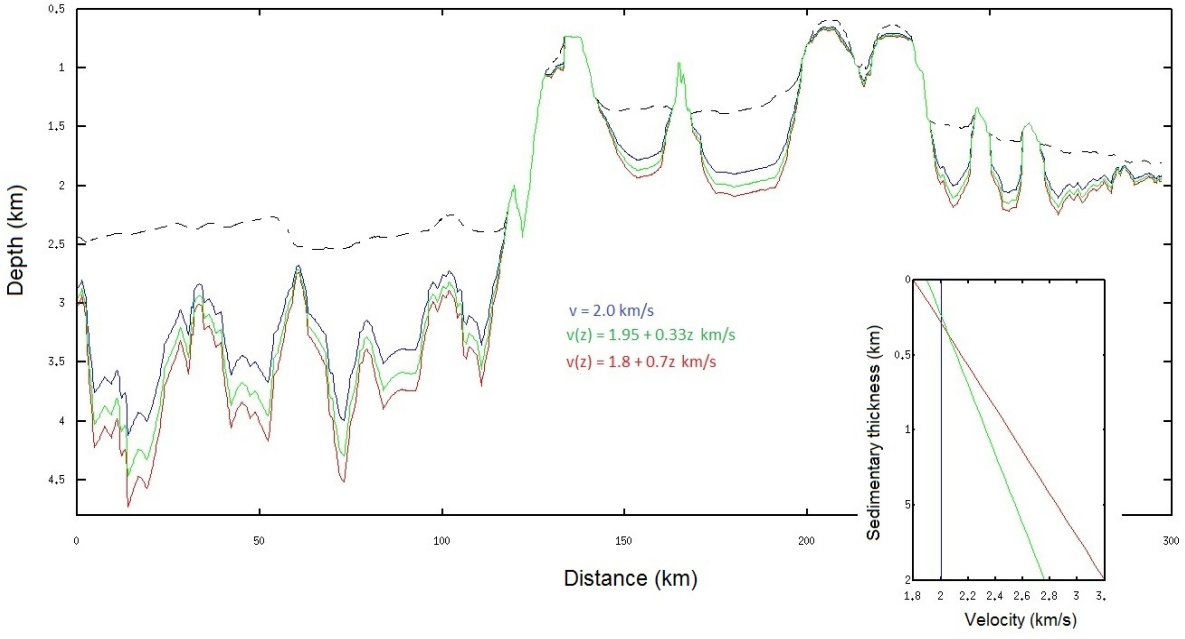

Figure 8.2: Depth converted sedimentary unit. Upper black dashed line is the seafloor. Blue line corresponds to a constant velocity, v_p = 2.0 km/s. Red line represents v_p = 1.95 + 0.33Z (Myhre and Eldholm, 1981). The green line, v_p = 1.8 + 0.7Z, is based on nearby crustal studies (Breivik et al., 2012; Kandilarov et al., 2012; Kodaira et al., 1998; Voss et al., 2009).

Depth conversion was calculated iteratively. It was done separately for each trace along the profile. The solver scheme used was an implementation of Euler's method, Table 8.1.

Table 8.1: Euler method used for depth conversion.

z_0
v_0
z(t + Δ t) = z(t) + v(z(t)) * dt
v(z + Δ z) = v(z) + $\frac{dv(z)}{dz}$ * (z(t + Δ t) – z(t))

"t" is the internal travel time vector. "z" is the thickness vector. $z_0 = 0$ and $v_0 = 1.8$ are the start values, i.e. initial conditions. A thickness and a velocity value are assigned to each time step Δt. The values found at the bottom of the layer are incorporated into the starting model as the thickness of the sedimentary unit and the bottom velocity. The error of the iteration is on the order of the value assigned to Δt. Δt was put equal 0.001 seconds.

The starting model is presented in Figure 8.3. There a value of 3.5 km/s is assigned to the basement as a constant value, which would later be adjusted. The number of boundary nodes and velocity nodes for the layers are also listed. The sea bed and the basement was re-sampled from 0.2 km intervals to 1.0 km intervals, and manual removal was done of nodes without any significance for the geometry. Velocity nodes were put at 5 km intervals in the sedimentary layer. In the basement velocity nodes were placed manually at each place a velocity difference could be expected.

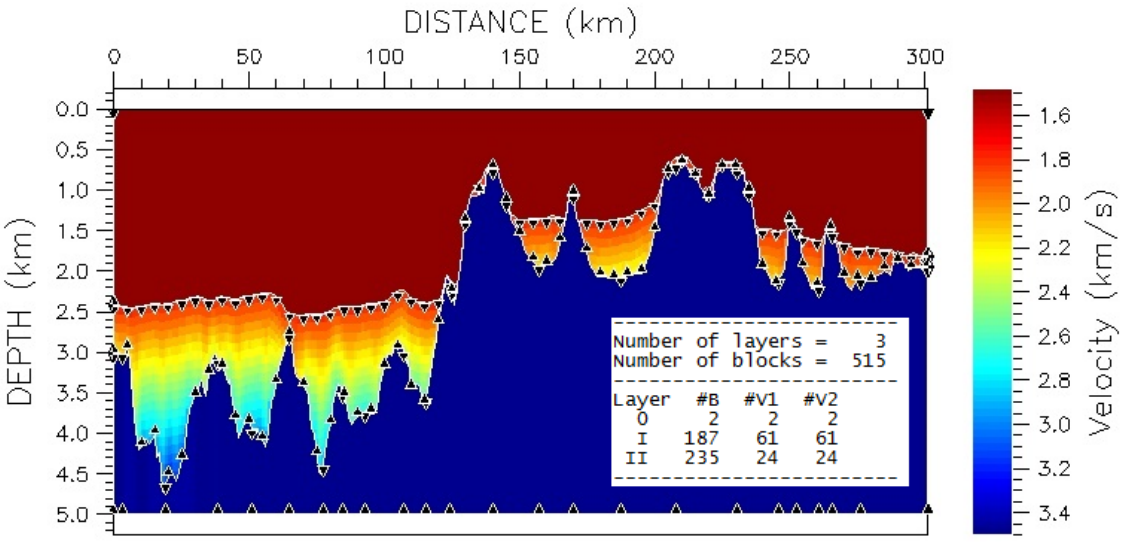

Figure 8.3: Starting model: Sea floor and depth converted top basement horizon.

8.2 P-wave forward modeling

Sparse OBS deployment and complex structures along the survey line, made the optimal choice of velocity layers somewhat difficult. Contradictory information was read in the datasets. OBS 1 and 3 indicated the need of four velocity layers, while OBS 2 and 4 indicated the need of only three. Possibly could there be lateral heterogeneities along the studied transect, which would make a variable number of layers along the line the best way of representing the data. However, layer pinch-outs did not turn out successful during modeling. It was decided that two separate models should be constructed simultaneously, to test which would be the most appropriate. These consisted of whole layers extending along the whole profile. Model 1 was constructed as a three layered crust: (I) Sedimentary unit, (II) upper crust and (III) lower crust. Model 2 was constructed as a four layered crust: (I) Sedimentary unit, (II-A) upper crust, (II-B) lower upper crust and (III) lower crust. The upper mantle (IV) was modeled as a underlying half-space.

Phases were identified through evaluating their geometrical shapes in the OBS data (see also Section 6.1.5). Over the Eggvin Bank the seafloor bathymetry is rough, which influence the geometrical shapes of the phases. Refracted waves were identified as first arrivals. These could potentially also have been head waves, but as head waves attenuate more easily they were mapped as refractions (see also Section 6.1.6). Secondary arrivals were more difficult to identify because of noise and interference below the first arrivals. Nevertheless, it was possible to identify a few reflections from the upper mantle. The terminology used in naming phases is listed in Table 8.2.

Table 8.2: P-wave phase notation.

Phase	Model 1	Model 2
P_d :	Direct water pulse	Direct water pulse
P_g :	Refraction within II	Refraction within II-A
P_s :	-	Refraction within II-B
P_c :	Refraction within III	Refraction within III
P_mP :	Moho reflection	Moho reflection
P_n :	Upper mantle (IV) refraction	Upper mantle (IV) refraction

Figure 8.4 displays how phase picking were done, as well as how Model 1 and 2 were picked differently from the same data set. The figure also contains an example of an unidentified near offset phase. Further explanation is found in the figure caption. Figure 8.5 shows a far offset feature in the data which could not be identified and in the end was not included into the model. Figure 8.6 presents an example of how amplitude evaluation was used in phase identification, as well as an example of the ambiguity between lower crustal refraction and Moho reflections. Further explanation is found in the figure caption. Multiples were not mapped, despite it is possible to model them in Rayinvr. However, they were in fact useful when identifying some phases at far offsets, where the multiples sometimes contained more signal strength than the first arrivals.

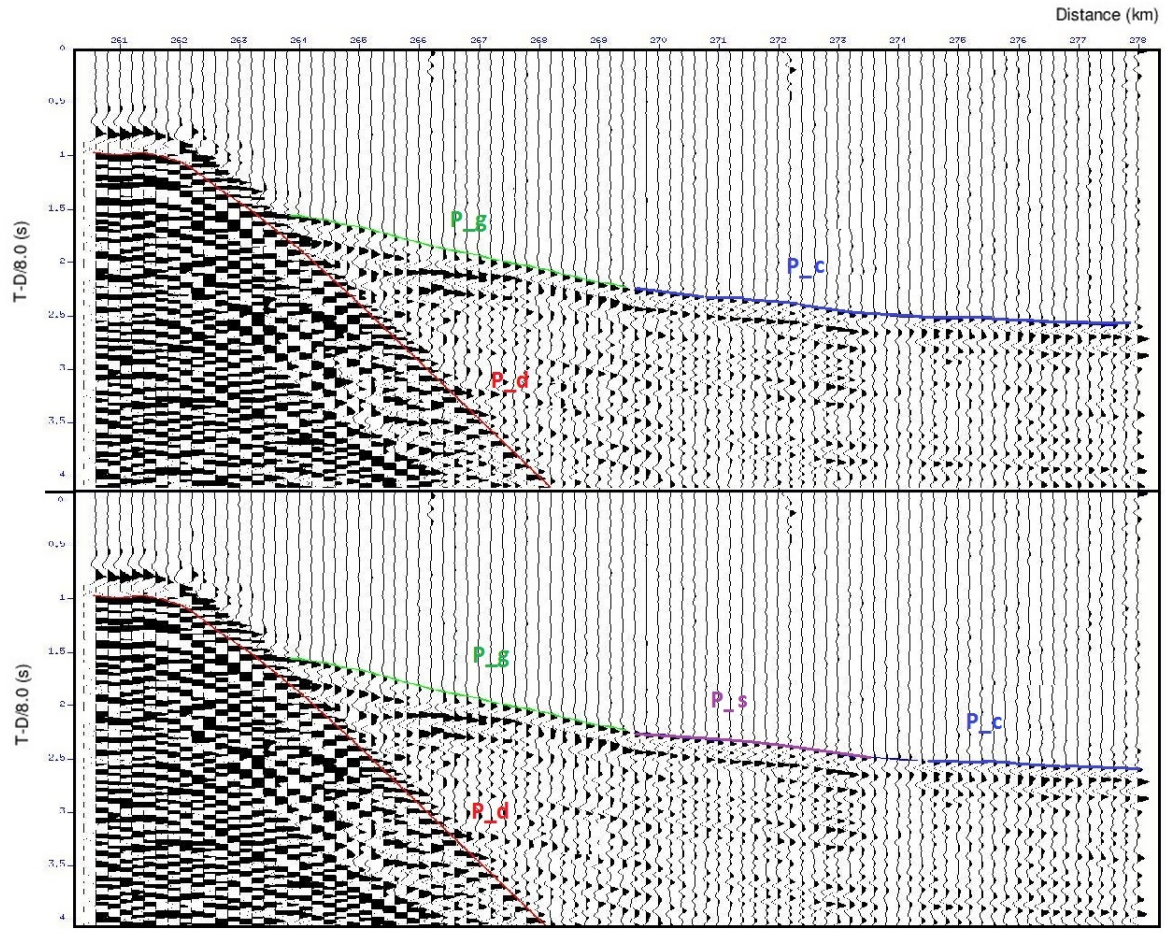

Figure 8.4: Example of phase picking on the southern side of OBS 1. The gather is displayed with wiggle traces. Top image shows how phase picking was done for Model 1, while the lower shows how it was done for Model 2. As the pulse is minimum phases, wave arrivals were picked at the first breaks, before maximum amplitude. Ringing caused by data processing is clearly visible above the water pulse, which is denoted P_d and marked with a red line. Refraction from the upper crust is marked with a green line and denoted P_g. What could possibly be a shallow reflection is observed underneath the green line. This Phase however could not be identified in the model and was in the end not included. An additional middle crustal phase was mapped for Model 2, P_s (purple color). Refraction from the lower crust is marked blue and denoted P_c. P_c in Model 1 encompasses both P_s and P_c as mapped in Model 2. This is the principal difference between the models, that Model 2 has introduced one extra velocity layer in the middle crust.

Uncertainties of 50 milliseconds were assigned to travel time picks of shallow phases from the upper crust. Phases from the lower crust were assigned 50 - 100 milliseconds. Mantle reflections and refractions were assigned 100 milliseconds uncertainties. To normalize the statistical weight of the phases and remove influence of uneven picking, the phases were re-sampled to 0.2 km intervals. The gap distance was chosen to be equal the shot distance. Phases with their assigned uncertainties are listed in Table 8.3 together with results from forward modeling. The two models obtained through forward modeling are presented in Figure 8.7.

The direct phase was mapped with remarkably bad fit, and it was decided not to include it in the estimates of the whole model resolution. Reasons for the bad fit could be the high amount of ringing observed around the direct pulse, which made it difficult to pick accurately (see also Figure 8.4). Another reason could possibly be off-line displacement of OBSs. The later could possibly generate small errors in the model caused by mismatch between phases mapped at different OBSs. To a certain extent this could be accounted for by making minor adjustments to the depth of the displaced OBS(s). A third reason for the bad fit could be an incorrect water velocity, or that one average velocity is not valid over the whole profile. Furthermore, in Rayinvr only two digits are included in each velocity parameter, while the water velocity was calculated to three digits. In the end so no actions were made to fix the bad fit, as the cause could not be identified. Accounting for one or more of the probable reasons would thus not necessarily improve the model.

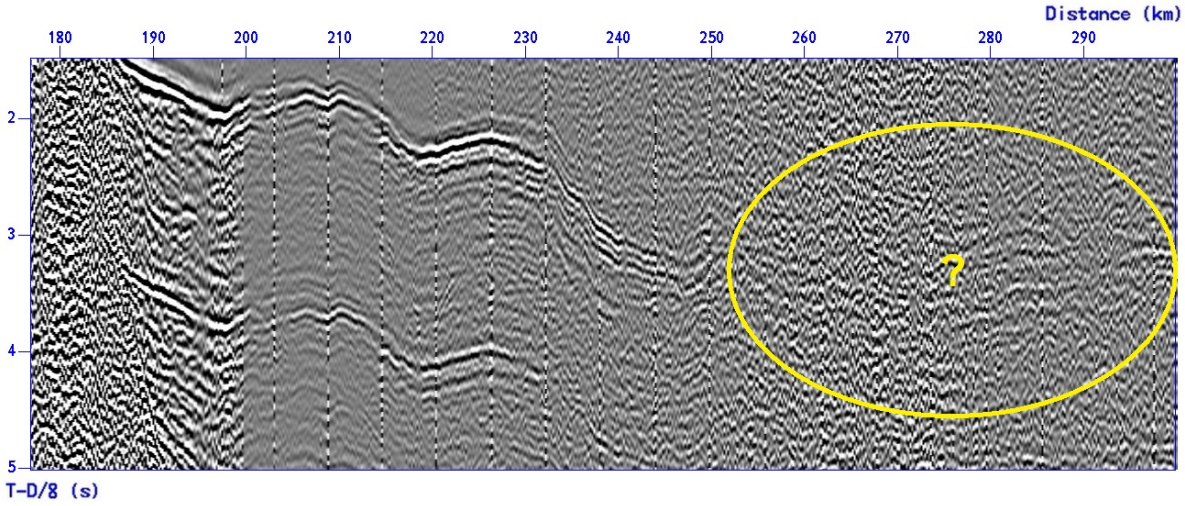

Figure 8.5: Unidentified feature at far offset on the south side of OBS 3. It can possibly be a phase, but it could not be incorporated into the model.

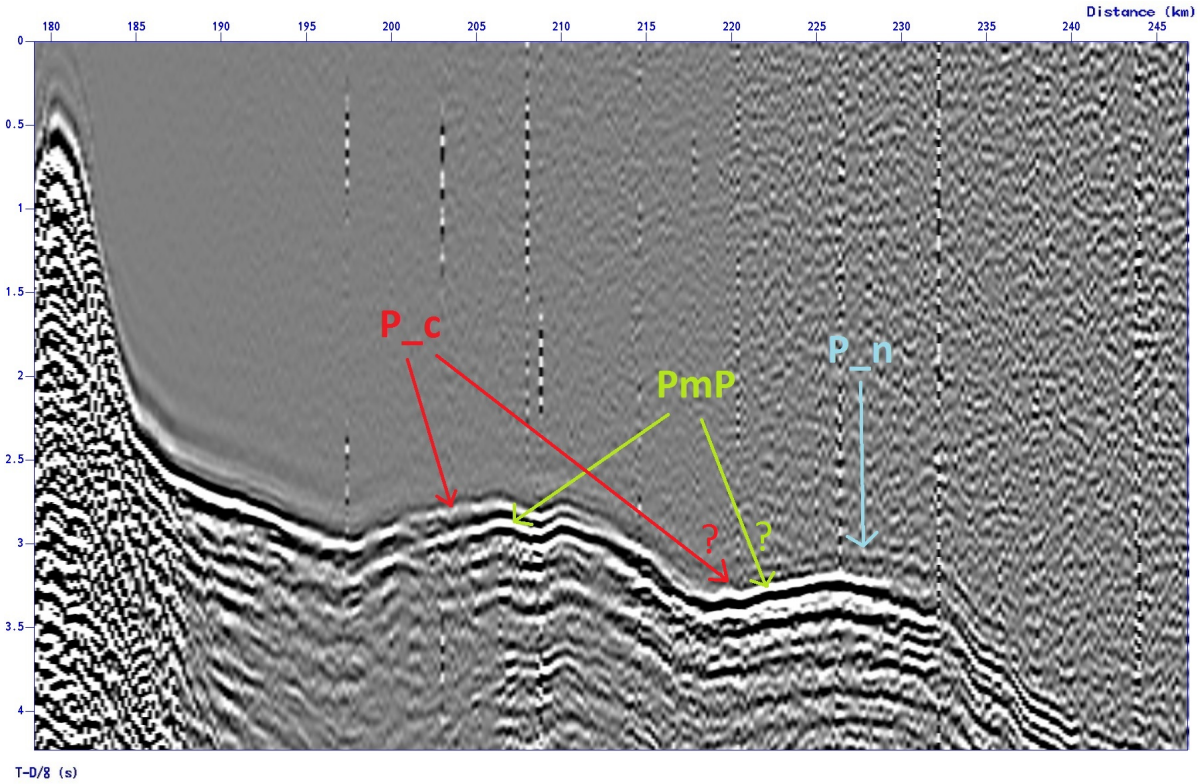

Figure 8.6: Example of different signature of phases, on the southern side of OBS 3. More shallow arrivals have greater amplitude than deeper ones, as seen from comparing the phase P_c with P_n. The P_mP-phase displays how reflections from the Moho will in general have a higher amplitude than refractions from the upper mantle, the P_n phase. At high incidence angles, greater than the critical angle, the reflections will have a very high amplitude (see also Figure 6.1, Section 6.1.3). A wave that enters the mantle, even at low incidence angles and with high transmission coefficients, will undergo more attenuation as the propagation path will be longer (see also Section 6.1.6). The image also shows the ambiguity that occur at far offsets between a refraction within a layer and a reflection from the bottom of that same layer. The phase was modelled as both a lower crustal refraction and a Moho reflection.

Table 8.3: Results from forward modeling of P-waves in Rayinvr. n: Number of traced rays. Δt_{RMS}: RMS travel time residual. χ^2: Chi-squared value. The direct phase is not included in the whole model estimates due to the bad fit.

		Model 1			Model 2		
Phase	Uncertainty (ms)	n	Δt_{RMS}	χ^2	n	Δt_{RMS}	χ^2
P_d :	50	40	0.175	11.308	40	0.175	11.308
P_g :	50	304	0.098	1.715	209	0.060	1.469
P_s :	50/100	-	-	-	280	0.061	1.483
P_c :	50/100	1321	0.074	1.322	1287	0.086	1.755
P_mP :	100	288	0.051	0.534	327	0.078	0.611
P_n :	100	1009	0.096	1.097	1006	0.081	0.655
Whole model:		2922	0.083	1.206	3109	0.080	1.233

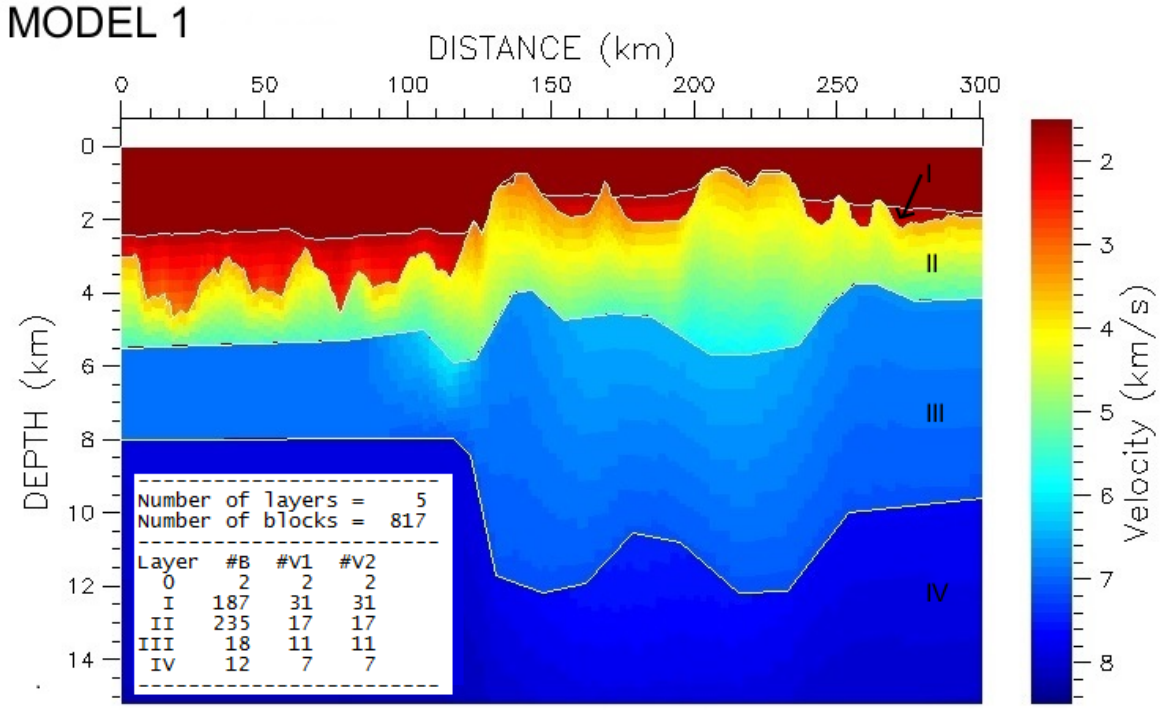

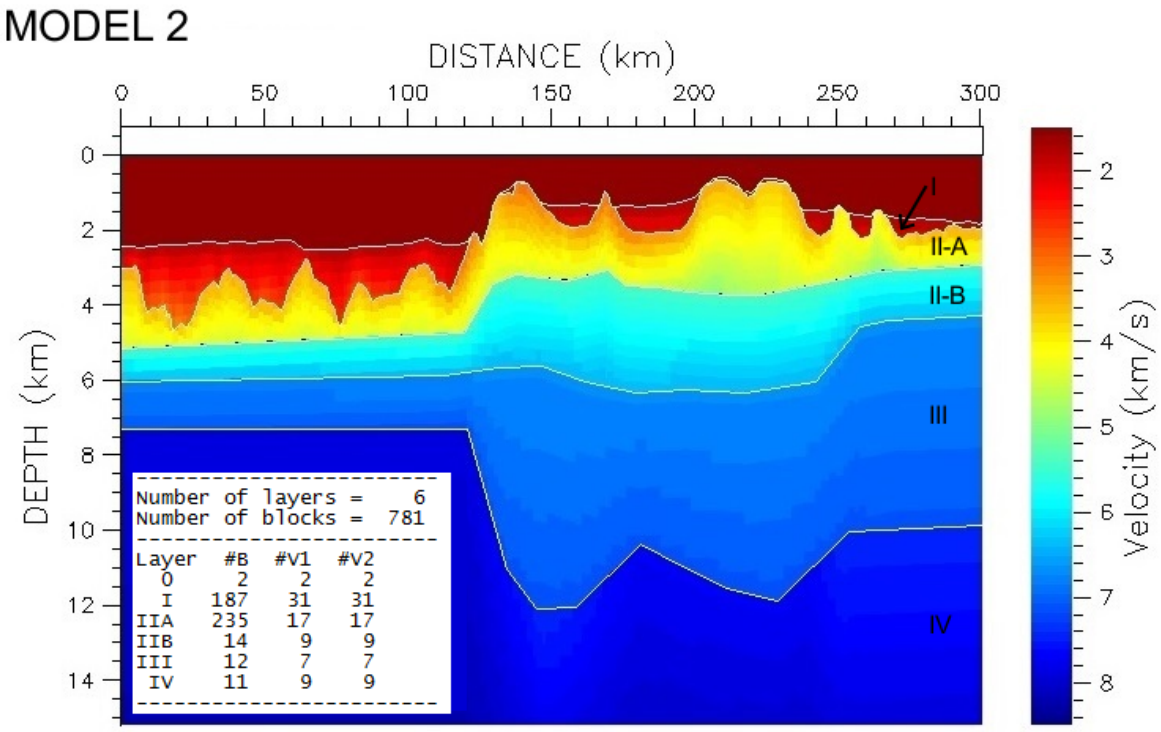

Figure 8.7: Result of P-wave forward modeling. Upper image is Model 1 containing three crustal layers: Sedimentary unit (I), upper crust (II) and lower crust (III). Lower image is Model 2 containing four crustal layers: Sedimentary unit (I), upper crust (II-A), lower upper crust (II-B) and lower crust (III). In both models the upper mantle (IV) is a half-space in the bottom.

8.3 P-wave inversion

An inversion was done to make small-scale adjustments to the model parameters while improving the fit between the calculated and the predicted travel times. The aim of the inversion was established according to Zelt and Smith (1992): Minimizing an overall chi-squared value, χ^2_N, without compromising the models ability to trace rays. These two targets are efficiently considered to be of equal importance. χ^2_N is a normalized value the χ^2 of all phases. A normalized chi-squared value of unity is the desired result (see also Section 7.2.4). The ray tracing ability is quantified as the number of traced rays in forward modeling.

The weighting factors W_t and W_m makes the inversion sensitive to the uncertainties of the travel time picks and model parameters (see also Equation 7.7, Section 7.2.3). Higher uncertainties of a parameter will make the parameter have less effect on the inversion. Pick uncertainties were used as the time weights. Uncertainties of model parameters were assigned typical values of 0.1 (Zelt and Smith, 1992). No difference were made between boundary and velocity nodes, as nothing implied that one were better constrained than the other.

To control the inversion a damping factor must be chosen (see also Equation 7.7, Section 7.2.3). This factor controls the trade off between best fit to the data and conservation of the original model. A plot is displayed in Figure 8.8 of how the model resolution depends on the choice of the damping factor. Single inversions was repeated for different damping factors, chosen at discrete intervals of 0.1 over the range 0.1 to 10.0. At each single inversion with a different damping factor, the number of traced rays, i.e. data points, and χ^2_N were compared.

As a measurement of the overall change in the model, the root mean square (RMS) of the model parameter perturbation was calculated. This was done separately for boundary nodes and velocity nodes, giving one estimate for the total change in all the boundary nodes and one for the total change in all velocity nodes. They were denoted "ψ_B" and "ψ_V", respectively. All nodes were incorporated in the calculations, except the sea floor horizon, the velocities of the sedimentary unit and the the top basement horizon.

$$\psi = \sqrt{\frac{\sum \Delta m_i^2}{M}} \tag{8.3}$$

$\Delta m_i = m_i^{(orginal)} - m_i^{(new)}$: The change in the i-th parameter.
M: Number of parameters

With the right choice of damping factor, only one single iteration of the inversion routine was needed to obtain a small χ^2_N without reducing the number of traced rays. This was true for both models. Even though unity is the desired result of χ^2_N, an even smaller value was obtained. Efficiently this corresponds to over-fitted data. That is, the uncertainties of the phase picks are greater than their corresponding travel time residual. However, while the model does not lose its ability to trace rays, a smaller χ^2_N corresponds to a better fitted model. The damping factor was

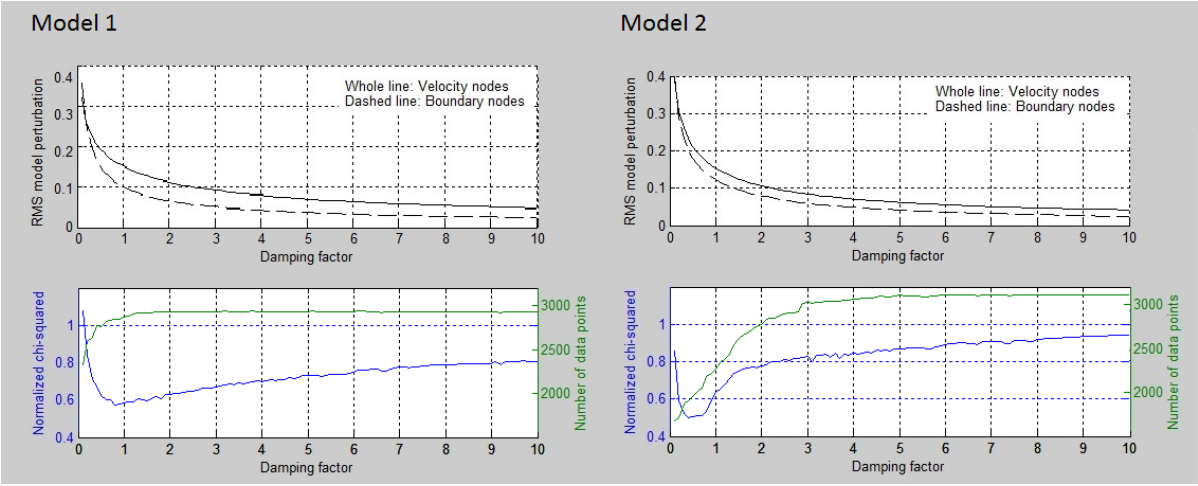

Figure 8.8: Plot showing how resolution from inversion varies for different damping factors. The purpose of the plot is to make an optimal choice of the damping factor. Left image is from Model 1, while right images is from Model 2. Lower graphs: χ^2_N and number of traced rays (data points) after inversion, done for a range of factor values. Upper graphs: The RMS model perturbation after inversion, done at the same range of factor values. For Model 1 a damping factor of 1.9 was determined the best choice. For Model 2 a damping factor of 5.0 was determined the best choice.

chosen to be equal 1.9 for Model 1 and 5.0 for Model 2. A greater change was applied to Model 1 than to Model 2. The resolution obtained was good for both models. Additional inversions and further improvement of travel time fit seemed to inevitably contribute to a decrease in traced rays. One single inversion was then determined to yield the preferred small-scale adjustments. Table 8.4 presents the results after one single inversion. Compared to Table 8.3 improvement of fit has occurred for all phases.

More documentation on the final P-wave models (after inversion) are attached in Appendix B.1. The complete documentation on phase picks and ray tracing is found there; e.g. images of OBS seismic, phase picks and ray tracing, as well as the numerical output from forward modeling.

Table 8.4: Results from inversion. D: damping factor used for inversion. ψ_B and ψ_V: RMS of the model boundary and velocity parameter perturbation, respectively. n: Number of traced rays. Δt_{RMS}: RMS travel time residual. χ^2: Chi-squared value.

		Model 1			Model 2		
		D	ψ_B	ψ_V	D	ψ_B	ψ_V
Description of single iteration:		1.9	0.067	0.115	5.0	0.041	0.062
Phase	Uncertainty (ms)	n	Δt_{RMS}	χ^2	n	Δt_{RMS}	χ^2
P_g :	50	304	0.051	0.609	210	0.049	0.953
P_s :	50/100	-	-	-	278	0.043	0.759
P_c :	50/100	1324	0.059	0.809	1282	0.074	1.320
P_mP :	100	288	0.047	0.502	327	0.072	0.518
P_n :	100	1015	0.061	0.442	1007	0.065	0.426
Whole model:		2931	0.058	0.630	3104	0.067	0.870

8.4 S-wave forward modeling

Two types of S-waves phases were identified on the radial component of the OBS data, PPS- and PSS-waves. PPS-waves travel downwards as P-waves, reaches it lowermost point and turns, and then convert to S-waves somewhere along the way upwards. PSS-waves convert on the way down, at the sea floor or top basement, and travel the rest of the way inside the crust as a S-wave.

In processing two different presentation of the radial components were made. A velocity reduction of 8.0 km/s was applied to enable identification of PPS-waves, while 4.6 km/s was applied to enable identification of PSS-waves. Figure 8.9 and 8.10 contain examples of how PSS- and PPS-phases were identified. PPS-phases were first arrivals on the horizontal component that arrived with a short time delay after the P-waves. PSS-waves were identified as secondary arrivals that have a less clear signature than the clear P- and PPS-wave arrivals. Uncertainties was typically set to 0.05 – 0.2 seconds for PPS-waves. The PSS-waves were assigned uncertainties between 0.1 and 0.2 seconds. Contrary to the strategy of P-wave picking, unsure S-wave phases were incorporated. This is because the S-waves were fitted into the framework of an already obtained p-wave modeling.

On the south side of OBS 4 no PSS-waves were identified. No PPS-phases were identified in the data from OBS 2, nor from the north side of OBS 4. In this data the first arrivals were time delayed less than 0.2 seconds from the first arrivals in the vertical component. A phase with such shallow conversion point was not possible to identify for the large scale velocity layers modeled.

Table 8.5 lists the phase notation used for S-waves. In Table 8.6 the phase picks are presented together with the results from ray tracing. Table 8.7 presents the Poisson's ratio obtained from PPS- and PSS-wave modeling in both models. The complete documentation on phase picks and ray tracing is attached in In Appendix B.2.

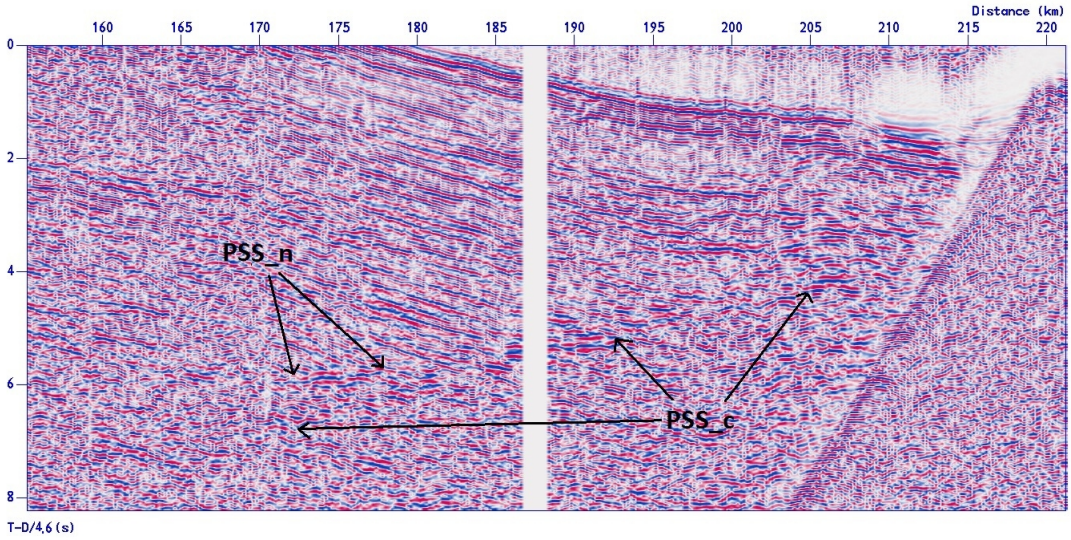

Figure 8.9: Example of PSS-wave phase picking on the northern side of OBS 2.

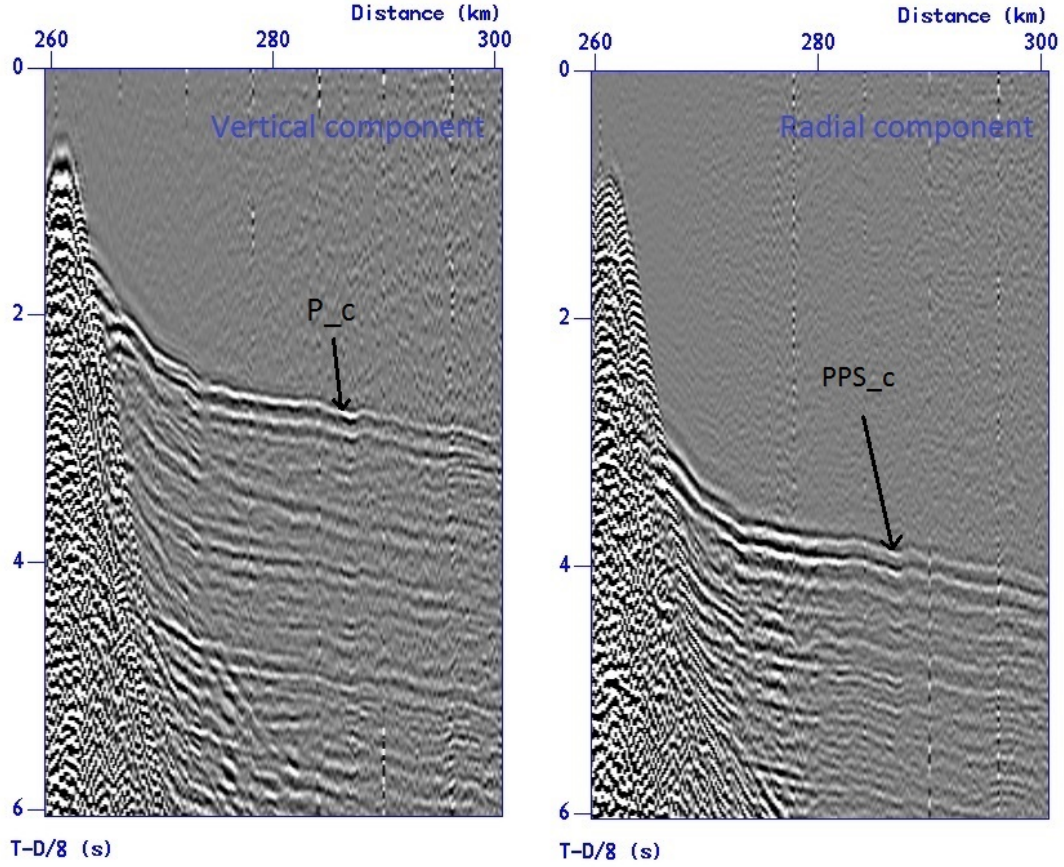

Figure 8.10: Example of PPS-wave phase picking on the southern side of OBS 1. A time lag exist between the P_c-phase in the vertical component (left image) and the PPS_c-phase in the radial component (right image).

Table 8.5: S-wave phase notation.

	Model 1		Model 2	
Phase	Path	Conversion	Path	Conversion
PSS-waves				
PSS_g :	Refraction within II	I/II	Refraction within II-A	I/II-A
PSS_s :	-	-	Refraction within II-B	I/II-A
PSS_c :	Refraction within III	I/II	Refraction within III	I/II-A
PSS_c* :	Refraction within III	0/I		
PS_mS :	Reflection from top of IV	I/II	Reflection from top of IV	I/II-A
PSS_n :	Refraction within IV	I/II	Refraction within IV	I/II-A
PSS_n* :	Refraction within IV	0/I	Refraction within IV	0/I
PPS-waves				
PPS_s :	-	-	Refraction within II-B	II-B/II-A
PPS_c :	Refraction within III	III/II	Refraction within III	III/II-B
PPS_c* :	-	-	Refraction within III	II-B/II-A
PPS_n :	Refraction within IV	IV/III	Refraction within IV	IV/III
PPS_n* :	Refraction within IV	III/II	Refraction within IV	III/II-B

Table 8.6: Results from S-wave forward modeling. n: Number of traced rays. Δt_{RMS}: RMS travel time residual. χ^2: Chi-squared value. For the whole model weighted averages are presented.

		Model 1			Model 2		
Phase	Uncertainty (ms)	n	Δt_{RMS}	χ^2	n	Δt_{RMS}	χ^2
PSS-waves							
PSS_g :	100	50	0.109	1.208	39	0.173	3.068
PSS_s :	100	-	-	-	57	0.202	4.156
PSS_c :	100	786	0.246	6.048	1084	0.244	5.942
PSS_c* :	100	344	0.098	0.956	-	-	-
PS_mS :	100	49	0.400	4.078	49	0.267	1.822
PSS_n :	200	729	0.239	1.431	729	0.283	2.003
PSS_n* :	200	201	0.152	0.584	201	0.262	1.720
$Combined$:		2159	0.221	3.007	2159	0.258	4.020
PPS-waves							
PPS_s :	50/100	-	-	-	112	0.114	1.301
PPS_c :	100	958	0.237	10.787	630	0.097	2.719
PPS_c* :	100	-	-	-	383	0.134	1.812
PPS_n :	200	160	0.373	3.507	160	0.398	3.985
PPS_n* :	100	-	-	-	101	0.054	0.295
$Combined$:		1118	0.261	9.741	1386	0.170	2.317
Whole model:		3277	0,235	5,304	3545	0.224	3.354

Table 8.7: Distribution of Poisson's ratio in the crust. Results from S-wave forward modeling.

		Model 1		Model 2	
		PSS-wave	PPS-wave	PSS-wave	PPS-wave
Poisson's ratio:	I	0.38	0.41	0.40	0.38
	II-A	0.34	0.35	0.34	0.36
	II-B	-	-	0.35	0.35
	III	0.29	0.29	0.29	0.29
	IV	0.25	0.25	0.25	0.25

8.5 Estimated uncertanties of model parameters

Several ways have been suggested to asses resolution of a model obtained with Rayinvr (Zelt, 1999). Estimated uncertainties should address the amount of change that can be aplied to model parameters without making the model lose its ability to trace rays or reducing the accuracy of data fit, in any significant amount. In this study it was chosen to estimate uncertainties through a multi-node perturbation test (Section 4.3.1 in Zelt, 1999). The following procedure was done: A set of boundary or velocity nodes were perturbed a given amount. These were in turn held fixed while all other parameters were inverted. The result were then compared to the original model. This was repeated with an increase in perturbation for each turn. The uncertainty limit was reached when the new model was statistical different than the original, determined by an F-test at a 95% probability level.

$$F = \frac{\chi_1^2}{\chi_2^2} \tag{8.4}$$

With probability density function (e.g., pp 204 in Bevington and Robinson, 2003):

$$P_F(F, \nu_1, \nu_2) \tag{8.5}$$

ν: Degrees of freedom (see also Section 7.2.4)

An F-test compares the travel time fits and the number of rays of two models, and determines whether they are statistically different. It was controlled that the model did not lose its ability to trace rays before a statistical different model was obtained. Using χ^2 values to evaluate the model uncertainties is considered a good way to relate uncertainties in the phase picks with uncertainties in the model parameters. Furthermore, inverting for each perturbarion accounts for the correlation between model parameters. Theoretically, the uncertainty of each model parameter can be a correlated estimate that reflect uncertainties of all the data parameters (e.g., pp 421 in Stein and Wysession, 2003).

$$\sigma_m^2 = G_{ij}\ \sigma_d^2\ G_{ji} \tag{8.6}$$

σ_m^2 and σ_d^2 are the variance-covariance matrices for the model and data parameters.
G_{ij} is a generalized inverse of matrix A_{ij}, from: $\Delta t_i = A_{ij}\Delta m_j \rightarrow \Delta m_i = G_{ij}\Delta t_j$
Δm_i are the model parameters, A_{ij} the partial perivative matrix and Δt_j the data points.
(see also Section 7.2.3).

For boundary nodes the final uncertainty is the RMS average of maximum positive and negative perturbation. For velocity nodes the uncertainty estimate is the RMS average of maximum positive and maximum negative perturbation of upper and lower nodes, as well as the maximum positive and negative bulk layer perturbation. Estimates of uncertainties in S-wave velocities could not be obtained. The estimated uncertainties are listed in Table 8.8.

Table 8.8: Estimated bulk parameter uncertainties.

Model 1				
	Eggvin Bank and Island Plateau (120-301 km)		Greenland Basin (0-120 km)	
Layer	Boundary (km)	Velocity (km/s)	Boundary (km)	Velocity (km/s)
II	-	0.07	-	-
III	0.10	0.04	-	-
IV	0.30	0.09	0.86	0.11
Model 2				
	Eggvin Bank and Island Plateau (120-301 km)		Greenland Basin (0-120 km)	
Layer	Boundary (km)	Velocity (km/s)	Boundary (km)	Velocity (km/s)
IIA	-	0.07	-	-
IIB	0.16	0.06	-	-
III	0.20	0.05	-	-
IV	0.40	0.09	1.20	0.2

8.6 Comparison of two obtained models

Two different models were obtained through velocity modeling. One was modeled with three velocity layers and the other one with with four. The preferred model should contain minimum complexity where its features are directly accounted for by the data. At the same time, geological insight must be applied in an heuristic approach.

It was concluded that Model 2 was the more appropriate representation of the data.

Commonly in crustal velocity models, the subsurface is modeled as discrete horizontally orientated layers stacked on top of each other. Model 2 displays a more traditional way of modeling oceanic crust than what Model 1 does. The horizon II/III in Model 1 shows a complex structure, while horizons II-A/II-B and II-B/III in Model 2 are more horizontal and plane. Furthermore, in Model 1 it is seen that the horizon contains sharp peaks underneath OBS 1 and OBS 4. Similar, the velocity gradient underneath OBS 2 is very high. The fact that these features are found

underneath the OBS locations, indicate that the three layered crust is not the optimal choice. Shallow features can only be observed in the near offset range. A simplification was done while forward modeling of Model 1. Lower crustal phases were set to encompass a shallow phase in the near offset of each OBS. This was done because it was not clear whether the OBS data indicated the need of an extra layer. However, this way of picking phases lead to quite severe artifacts underneath the OBSs. By introducing an extra velocity layer in the upper crust, a more horizontal topography was achieved.

χ^2 and Δt_{RMS} for both p-wave models are similar. However, Model 1 has a slightly better fit than Model 2 (see Table 8.4, Section 8.3). On the other hand, Model 2 has about 6% more rays traced than Model 1. There are some phases that can be traced slightly longer in Model 2. Nevertheless, in both models it is possible to trace rays to most of the observed P-wave arrivals in the OBS data. Estimated uncertainties indicate that the model parameters in Model 1 are slightly better constrained than in Model 2 (see Table 8.8).

The PSS-wave data do not indicate the necessity of an additional layer, as the data do not provide information about the shallow structures. For the same amount of rays, Model 1 has a slightly better fit than Model 2 (see Table 8.6, Section 8.4). The PPS-phases, on the other hand, yields a much better fit for Model 2 than for Model 1. Model 2 has χ^2 = 2.317 while Model 1 has χ^2 = 9.741. Furthermore, about 24% more rays are traced in Model 2. Upper crustal phases in OBS 3 indicate the presence of a conversion point that can not be provided in Model 1. The additional horizon in Model 2 gives a good fit for this phase.

Model 2 has a more stepwise velocity increase with depth, while Model 1 has a high velocity gradients, especially in the upper crust (layer II). Following an heuristic approach, Model 2 is the more traditional way of modeling the crust and it is more similar to how the Iceland Plateau has been mapped in other surveys (Kodaira et al., 1997, 1998). The lower crustal structures are mapped about equally with both models. The Moho topography is much the same in both models. 0.7 km difference in thickness of the Greenland Basin is an arbitrary result, caused by low seismic coverage in the area.

It was concluded that the data indeed indication the presence of an additional velocity layer in the lower upper crust. Thus, only Model 2 will be evaluated further in Part IV.

Part IV

Results, Interpretation and Discussion

Chapter 9

Velocity Model

9.1 Presentation of results

Results form velocity modeling are presented in Figure 9.1. Phase statistics are listed in Table 9.1.

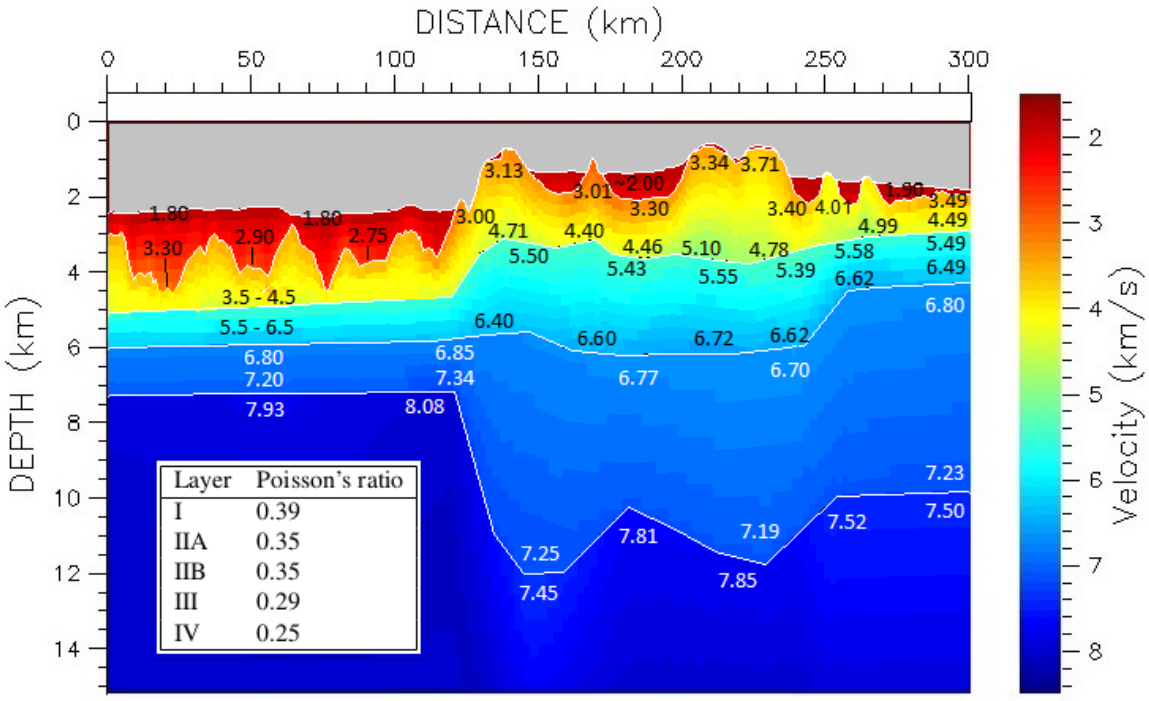

Estimated uncertainties

Layer	Greenland Basin (0-120 km) Boundary (km)	Velocity (km/s)	Eggvin Bank and Island Plateau (120-301 km) Boundary (km)	Velocity (km/s)
IIA	-	-	-	0.07
IIB	-	-	0.16	0.06
III	-	-	0.20	0.05
IV	1.2	0.2	0.40	0.09

Figure 9.1: Results form velocity modeling, including P-wave velocities (color coded and indicated with numeric value), Poisson's ratio and estimated uncertainties.

Table 9.1: Phase statistics of both P- and S-waves.

Phase	Uncertainty (ms)	Conversion	n	Δt_{RMS}	χ^2
P-waves					
P_g	50	-	210	0.049	0.953
P_c	50	-	278	0.043	0.759
P_s	50	-	1282	0.074	1.320
P_mP	100	-	327	0.072	0.518
P_n	100	-	1007	0.065	0.426
Total:			3104	0.067	0.870
PSS-waves					
PSS_g :	100	I/II-A	39	0.173	3.068
PSS_s :	100	I/II-A	57	0.202	4.156
PSS_c :	100	I/II-A	1084	0.244	5.942
PS_mS :	100	I/II-A	49	0.267	1.822
PSS_n :	200	I/II-A	729	0.283	2.003
PSS_n* :	200	0/I	201	0.262	1.720
Total:			2159	0.258	4.020
PPS-waves					
PPS_s :	50/100	II-B/II-A	112	0.114	1.301
PPS_c :	100	III/II-B	630	0.097	2.719
PPS_c* :	100	II-B/II-A	383	0.134	1.812
PPS_n :	200	IV/III	160	0.398	3.985
PPS_n* :	100	III/II-B	101	0.054	0.295
Total:			1386	0.170	2.317

Results from velocity modeling are P-wave velocity distribution over the crustal transect with estimated uncertainties, as well as one value of Poisson's ratio for each layer. P-wave modeling were used to construct the model. Layer I is the sedimentary unit. The crystalline crust consists of three layers: Upper (layer II-A), middle (layer II-B) and lover (layer III). Upper mantle (layer IV) is modeled as a half-space below the crust. S-waves were later fitted into the model. The value of Poisson's ratio is the average between modeling results of PSS- and PPS-waves. The PSS- and PPS-waves list results obtained with different Poisson's ratio in layer I and II-A (see also Table 8.7, Section 8.4). Figure 9.2 presents plots of P-wave ray density and the diagonal elements of the resolution matrix. Figure 9.3 presents the ray density of PSS- and the PPS-waves. In the density plots an high cut sensitivity was set at 100 rays, to better enhance smaller variations. It was not possible to obtain resolution matrices for S-waves since inversion was not done for converted waves.

No information about the sediment velocities was extracted form the data. Sediment thickness and P-wave velocities come from depth conversion of single-channel streamer seismic (see Section 8.1). Over the Eggvin Bank and the Iceland Plateau the velocities obtained range from 1.80

– 2.30 km/s. Thickness varies from zero to 0.5 km. In the Greenland Basin thickness vary from 0.2 to 2.0 km. 1.80 km/s was assigned the top velocities. Bottom velocities range from 2.40 - 3.30 km/s. A Poisson's ratio was estimated to be 0.39 over the whole profile.

Low seismic coverage over the Greenland Basin prevented detailed information about the crystalline layers. Most parts of Eggvin Bank and Iceland Plateau were well resolved. Layer II-A include seamounts and the uppermost crystalline crust. Typical velocities range from 3.4 to 4.6 km/s. Uncertainties were estimated to be $\pm$0.07 km/s. Average thickness is about 1.0 km. Where seamounts are located the thickness increases to about 2.0 km. Higher bottom velocities, 5.10 $\pm$0.07 km/s, were obtained at distance 200-230 km. Thickness of layer II-B increases from about 1 km in the Iceland Plateau to about 2 km in the Eggvin Bank. Typical velocities are 5.5 – 6.5 km/s. Uncertainties were estimated to be $\pm$0.07 km/s. For both II-A and II-B the average overall Poisson's ratio was estimated to be 0.35. Typical velocities in layer III are 6.80 – 7.20 km/s. Uncertainties were estimated to $\pm$0.07 km/s. S-wave modeling estimated Poisson's ratio to be 0.29. Average thickness is 6 km.

Gross crustal features could be estimated in the Greenland Basin close to the transform (km 60 – 110), although estimations were made from low seismic coverage and with high uncertainties. The crystalline crust is on average 4.0 km thick. Estimated uncertainty of Moho depth is $\pm$ 1.2 km. Upper mantle velocities were estimated to be 7.9 – 8.1km/s with estimated uncertainties of $\pm$ 0.2 km/s. The crystalline crust of the Eggvin Bank is thicker, 11 km at the seamount locations and 8 km in the middle of the bank. Moho depths rang from 10.3 and 12.1 km. Uncertainty of Moho depth was estimated to be $\pm$0.4 km. 7.81 and 7.85 km/s were obtained as upper mantle velocities. Uncertainty of velocities were estimated to be $\pm$0.09 km/s. A very low velocity (7.45 km/s) was modeled at the northern edge of the the Eggvin Bank (km 130 - 140). Low velocities ($\sim$7.50 km/s) were also modeled under the Iceland Plateau (km 245 – 300). These are areas with very little or no ray coverage and very poorly constrained velocity nodes. These values were disregarded as they were considered an artifact from velocity modeling. The Moho depth underneath Iceland Plateau was estimated 10.0 $\pm$0.4 km. This boundary is also badly constrained. A possible trade-off between Moho depth and upper mantle velocities can not be excluded. The Poisson's ratio of the mantle was estimated to be 0.25 over the whole profile.

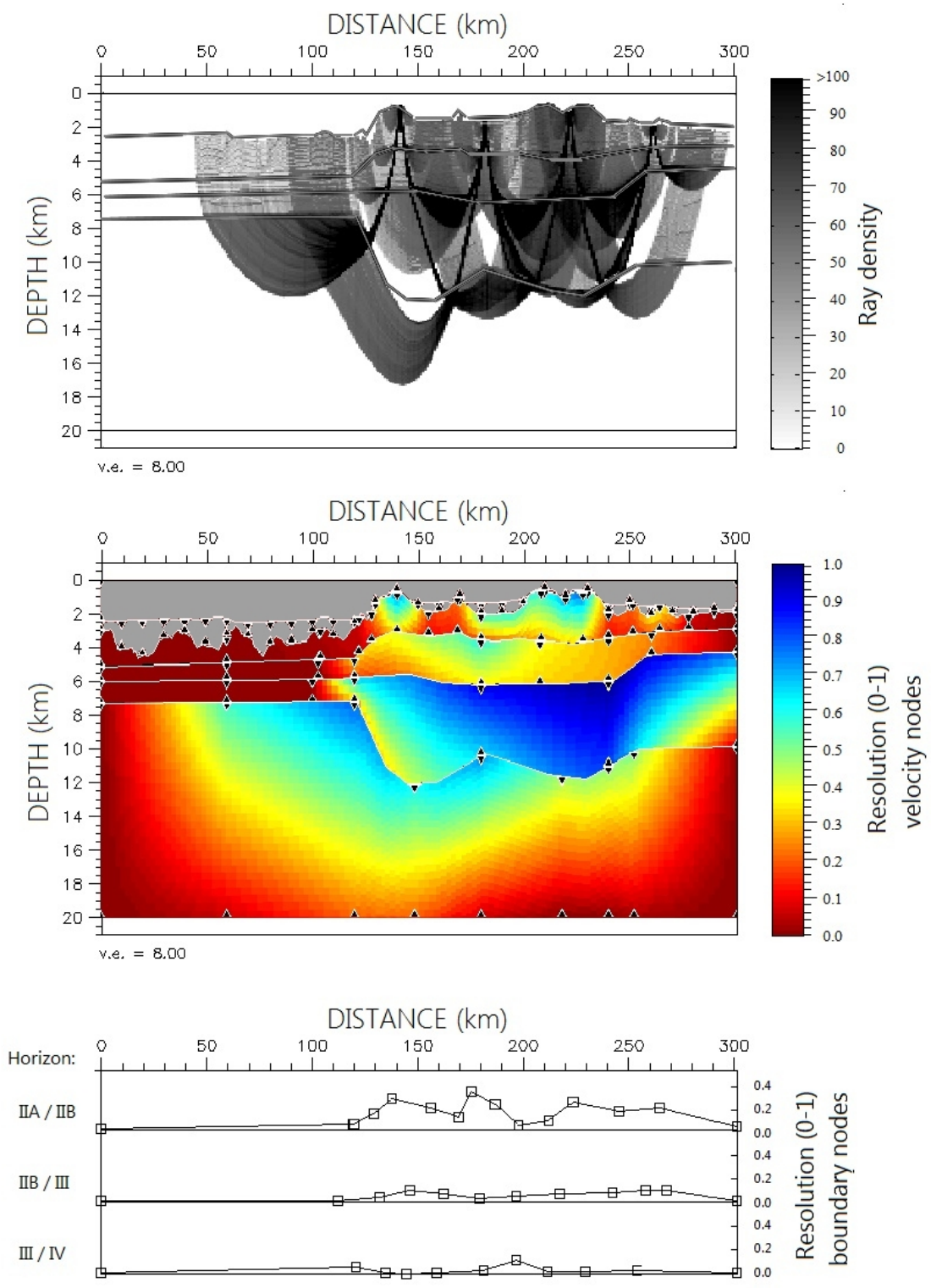

Figure 9.2: Upper image: P-wave ray density. Below: Linear dependence of model parameters. Resolution (0 - 1) is the diagonal component in the resolution matrix. A value of one indicates that the node is linearly independent, i.e. fully resolved by the ray coverage. A value of zero indicates that the node is totally unconstrained. Linear interpolation has been done between the resolution of each node, possibly exaggerating the spatial extent of well resolved structures. Boundary nodes are displayed as graphs for each horizon separately.

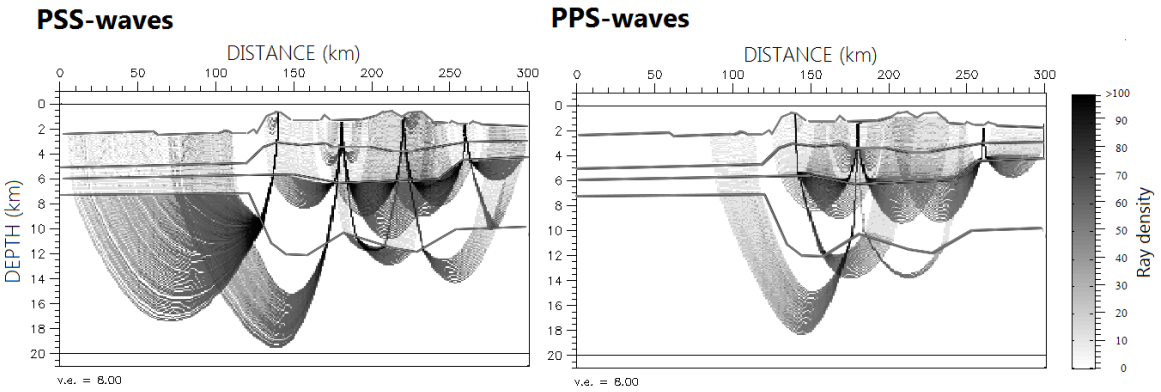

Figure 9.3: S-wave ray density: PSS-waves to the left and PPS-waves to the right.

9.2 Remark about model reliability

P-wave phase statistics show a good fit between the modeled and the observed data. RMS of travel time residuals ranges from 40 to 70 ms. Uncertainties of data picks were set between 50 and 100 ms. This gives an over-fitted χ^2_N with a value less than unity. At far offsets uncertainties were set to 100 ms. In hindsight this was slightly too high. A more accurate evaluation could have been done at various offsets to augment the credibility of the phase statistics. The degree of linear dependence is a measurement of how well the model parameters are constrained by the data. A very low resolution was obtained for the boundary nodes. This implies that the boundary nodes are not directly resolved by the data. It is seen that the node spacing is denser than what can be accounted for by the data, e.g. the model boundaries are too detailed. Velocity nodes on the other hand are better resolved, especially in the center of the model. However, these are maybe too sparsely separated in the deeper structures, e.g. in layer III velocity nodes can not resolve lateral changes corresponding to the highly variable Moho topography. The current node parametrization is somewhat too arbitrary, and that the model probably includes some details which can not be directly accounted for by the data. The opposite is also probable, that some lateral changes present in the data are excluded from the model because of too sparse node placement.

Two different models were derived simultaneously and both gave for example similar Moho structure. In Section 8.6 it was decided that the four layer crust is a better representation of the data than the three layer crust. More observations in the data could be identified and included into a model of four layers than into a model of three. If even more layers were to be included into the model, would it lead to a better fit of the data? This is probably true. However, the need for additional layers and complexity was not strongly indicated by the data. An exception is presented in Figure 8.4, Section 8.2. The PPS-waves in OBS 2 and 4 (cf. Section 8.4) could possibly also indicate the need of more complexity. However, the great majority of the OBS recordings did not indicate this.

The model parameters were constrained by P-wave phases. The major features observed in the OBS data was identified and modeled with a good fit. Nevertheless, some phases observed in the seismic could not be identified. At far offset it is difficult to decide whether it is patterns

in the noise or if it is seismic waves (see also Figure 8.5, Section 8.2). It was decided that it would be more correct to follow a more restrained approach, including only data that had been identified with certainty. To incorporate unsure phase picks, would increase the risk of introducing errors that would propagate into the model. Floating reflectors as well were omitted, as their presence were only weakly indicated. It was desirable to ensure that the model would be a true representation of the data, and that arbitrariness was excluded. Nevertheless, omitting parts of the data is to exclude potential information about the crustal structure. In the end a subjective decision has to be made. Consistency of one approach throughout the modeling, is thus believed to be a major constituent in the model's reliability.

The topography of the top basement has a great impact on the shape of the phase curves. The top basement was picked from the single-channel streamer seismic. Geometrical errors, which is usually resolved with migration techniques in multi-channel streamer seismic, had not been accounted for. An empirical velocity-depth trend was then used for depth converting the sediments, adding more uncertainties to the geometry of the horizon. Nevertheless, during ray tracing a good match was achieved between the modeled phases and the phase picks. The depth conversion was considered reliable for further mapping of the deeper structures.

S-wave modeling do not fit the data as well as the P-wave modeling. RMS of travel time residuals (100 – 400 ms) are greater than the assigned uncertainty picks (100 – 200 ms). Thus, χ^2_N for both PSS- and PPS-phases is much greater than unity, 4.0 and 2.3, respectively. Only one value of Poisson's ratio was assigned each layer. Lateral and vertical changes which do not directly relate to changes in P-wave velocities, were not accounted for. The obtained values of Poisson's ratio are thus more representative for the structures in the Eggvin Bank, than the peripheral structures. Uncertainties of the Poisson's ratio in each layer could not be estimated. Furthermore, the presented results are the weighted average between PSS- and PPS-phases. Modeling of different wave types gave different results for layer I and II-A. The appearance of the PSS-waves in the OBS data was very unclear, so unsure phases were incorporated into the model. Erroneous phase pick has most likely contributed to the low fit of the data. However, incorporating uncertain waves to constrain Poisson's ratio, in the framework of the P-wave model, was not considered as crucial as employing uncertain waves during P-wave modeling. The ray density plots shows where the seismic sampled the subsurface. PSS-phases turn as S-waves in layer III and IV, and give a good estimate of the S-wave velocity in these layers. Only a few PSS-waves turn in layer II-A and II-B, so the S-wave velocities in these layers are not as well constrained.

Chapter 10

Interpretation and Discussion

10.1 Presentation of regional geophysical data

Two regional maps of gravity and magnetic anomalies are presented in this section, Figure 10.1 and 10.2, respectively. A bathymetric map is presented in Figure 2.1, Section 2.1.

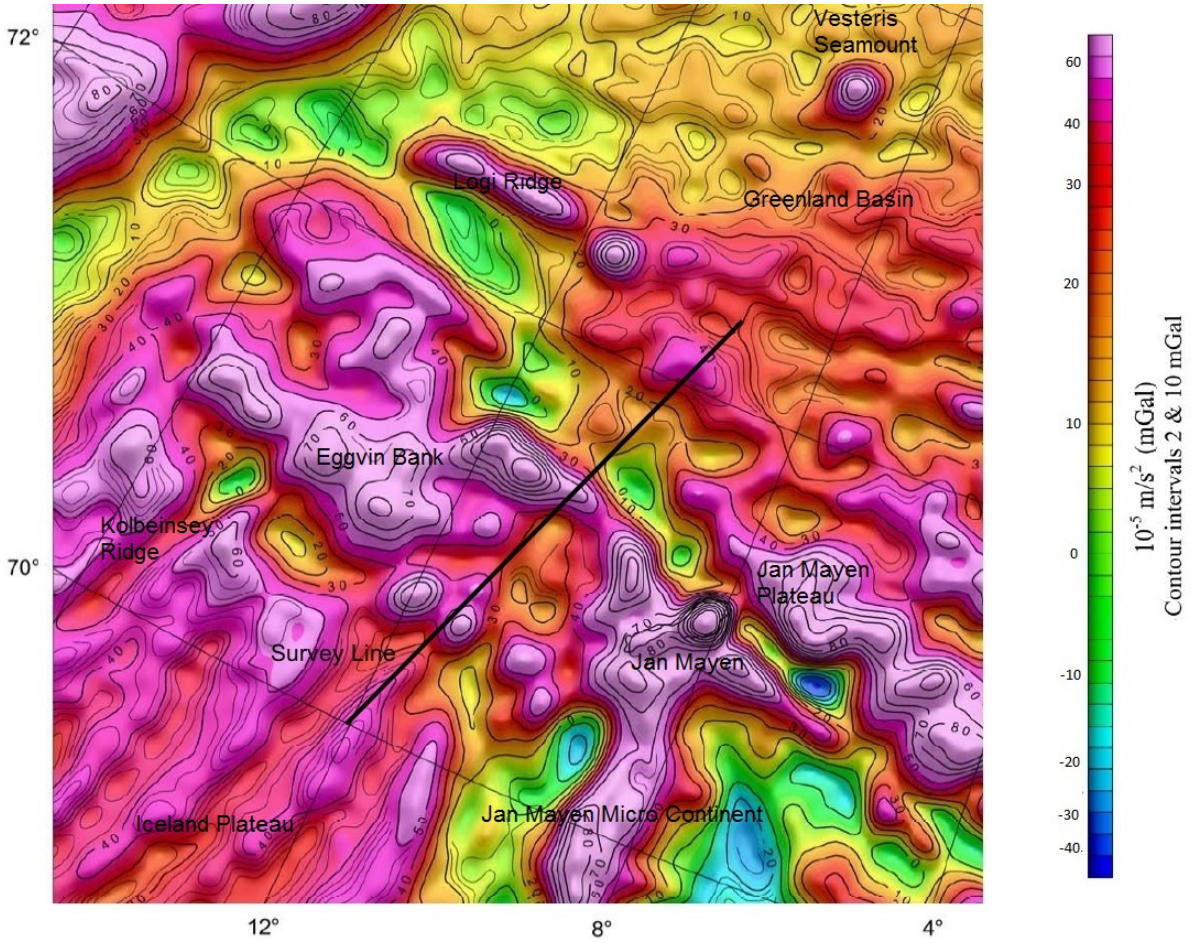

Figure 10.1: Regional gravity anomaly map, modified from Olesen et al. (2010). Survey line is indicated by the black line.

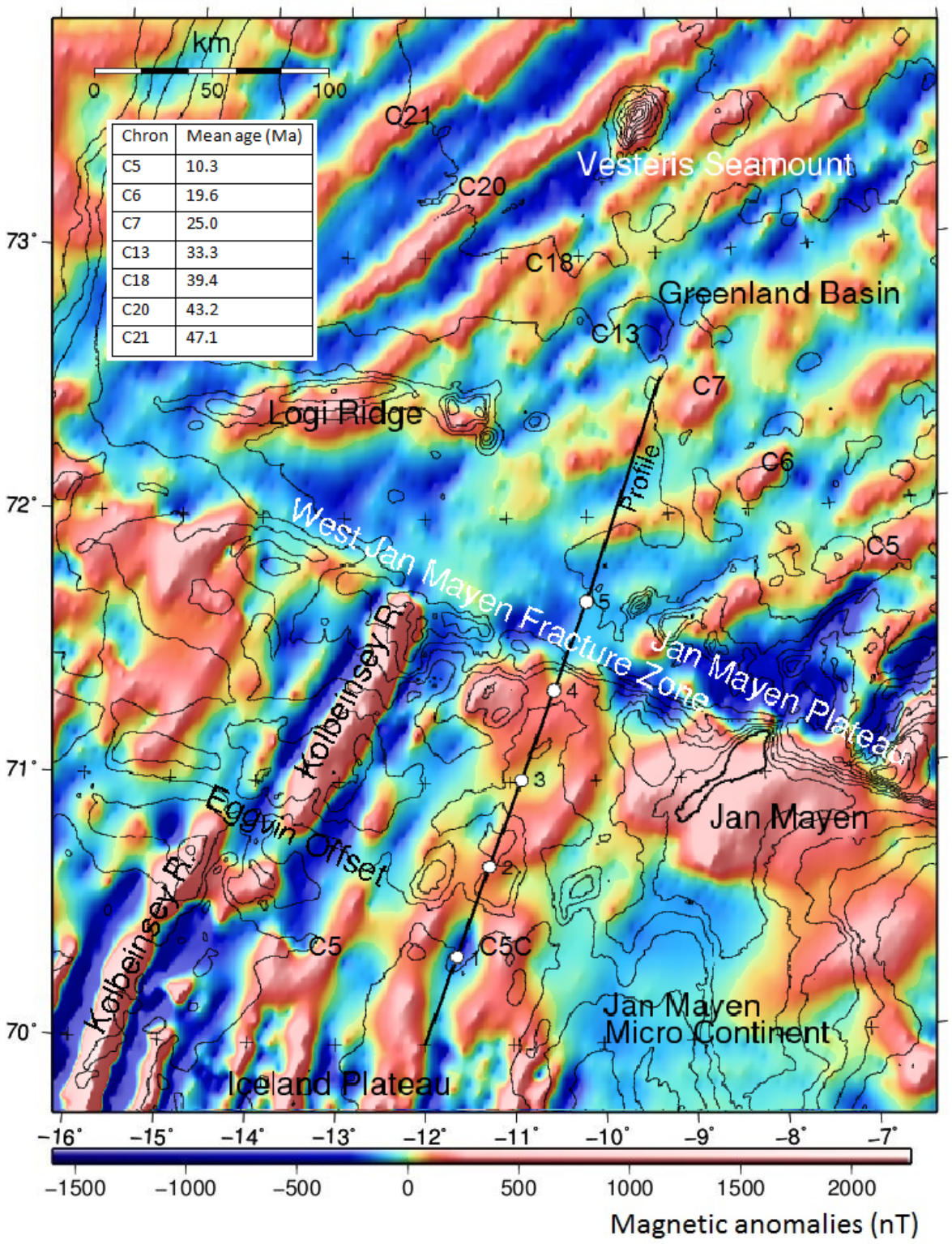

Figure 10.2: Regional magnetic anomaly map produced with data from Verhoef et al. (1996). Chrons in the Greenland Basin are after Engen et al. (2008). Chrons in the Iceland Plateau are after Peron-Pinvidic et al. (2012) and references therein. Average age of chrons are according to Cande and Kent (1995).

Figure 10.1 is an isostasy-corrected free-air gravimetric anomaly map (Olesen et al., 2010). It is derived from radar altimetry collected by satellites. The map can indicate differences in gross crustal thickness and seafloor bathymetry, as the sea surface elevation is compared to a reference geoid.

Figure 10.2 contains a compilation of magnetic data gathered during different surveys (Verhoef et al., 1996). The data displays the magnetic anomaly field. This is caused by permanent magnetization frozen into seafloor rocks, as they cooled below their Curie temperature. The earth's magnetic field strength itself, as well as short-term field variations, have been removed. Data coverage over the Eggvin Bank is from airborne surveying conducted along parallel lines in WNW-ESE direction. Spacing between survey lines are 20-30 km. In the surrounding areas data from both marine and airborne surveys have been compiled together. Survey lines are more densely spaced, as well as both in-line and cross-line.

10.2 Interpretation of single-channel streamer seismic

10.2.1 Eggvin Bank and Iceland Plateau

Interpretation of single-channel streamer (SCS) seismic over the Eggvin Bank and the Iceland Plateau is presented in Figure 10.3. The seismic features discussed in the text are marked in the figure.

The sedimentary unit is distinct from the underlying basement and the volcanic peaks. The seismic facies of the sediments display an over all parallel layering, while the basement has an high reflectivity and and granular appearance. The layering is not reverberation connected with the source, as that was removed during spiking deconvolution. Seabed multiples arrive underneath the top basement horizon. The most prominent features are the seamounts. They are denoted S1 to S6, from north to south. Underneath S1, S3 and S4 strong sea floor multiples are visible. S3 and S4 have a thin sedimentary unit at the top. S1 has a flat top and a thin sedimentary lens attached on its northern side. The flat top implies that S1 has extended above the sea surface at one point, before it was eroded down to sea level. Subsidence of the whole area must have happened later. The depth to S1 is about 700 meters below sea level. This coincide with the depth to underneath the sedimentary units of S3 and S4.

In the profile, the sedimentary thickness decreases southwards on the Icelandic Plateau. After depth conversion it is estimated to be 0.6 km thick in the north and 0.2 km thick in the south. On top of the Eggvin Bank, the sediments are zero to 0.7 km thick. Strong reflectors are present within the unit. These align quite well with the seafloor, though they have a less coherent appearance. The high reflectivity reflectors in the vicinity of S1 are interpreted as volcanic material eroded from the seamount. The deeper reflectors could potentially also be sills. It is not clear from the seismic whether sedimentary horizons of Eggvin Bank and Iceland Plateau are connected.

On the Eggvin Bank towards S1 and S3, the sedimentary layering is inclined with the slope

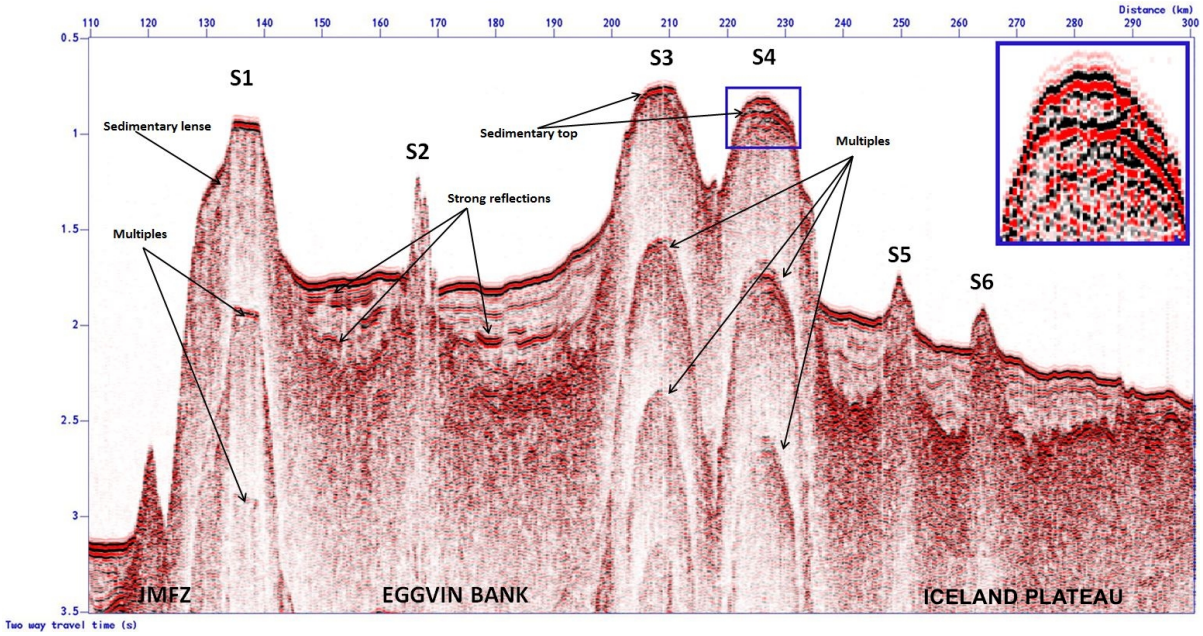

Figure 10.3: Interpretation of SCS seismic from the Eggvin Bank and the Iceland Plateau. Features highlighted in the seismic are discussed in the text. Top right frame is an enlargement of seamount S4 and its sedimentary top.

of the peaks. Towards S1 on the northern side only slightly, but towards S3 it is prominent. This could be caused by recent movement of the seamounts. Alternatively, the seamounts could also be of younger age than the sediments and the surrounding crust. The feature could also derive from sediment supply, i.e. erosion from the peaks. This feature is not seen on the southern side of S4. Typical on-lap deposition is seen towards the smaller seamounts, S2, S5, and S6.

10.2.2 Greenland Basin and the Jan Mayen Fracture Zone

Figure 10.4 contains an interpretation of the SCS profile over the Greenland Basin and the Jan Mayen Fracture Zone (JMFZ). The seismic features discussed in the text are marked in the figure.

A thick sedimentary sequence is present in the Greenland Basin. Depth conversion indicate that it varies from between 0.2 to 2 km in thickness. The unit contains clear parallel layering. This is not reverberation connected with the source, as that was removed during spiking deconvolution. Seabed multiples arrive underneath the top basement horizon. Some peg-leg multiples could be present in the seismic. Most layers, however, are not strictly parallel with respect to one another. Underneath the sedimentary unit is the basement, dominated by sharp peaks that cut up into the overlying sediments. Two horizons have been traced along the profile, R1 and R2. The lower, R2, has a layering corresponding to a in-fill in between the basement structures. Except at 60 km and 100 km along the profile, the lower sediments on-lap to most of the basement structures. The upper horizon, R1, lies semi-horizontally above in the upper part. Some undulation of the layers is observed along the line. The whole sedimentary unit has a slight apparent dip in northward direction.

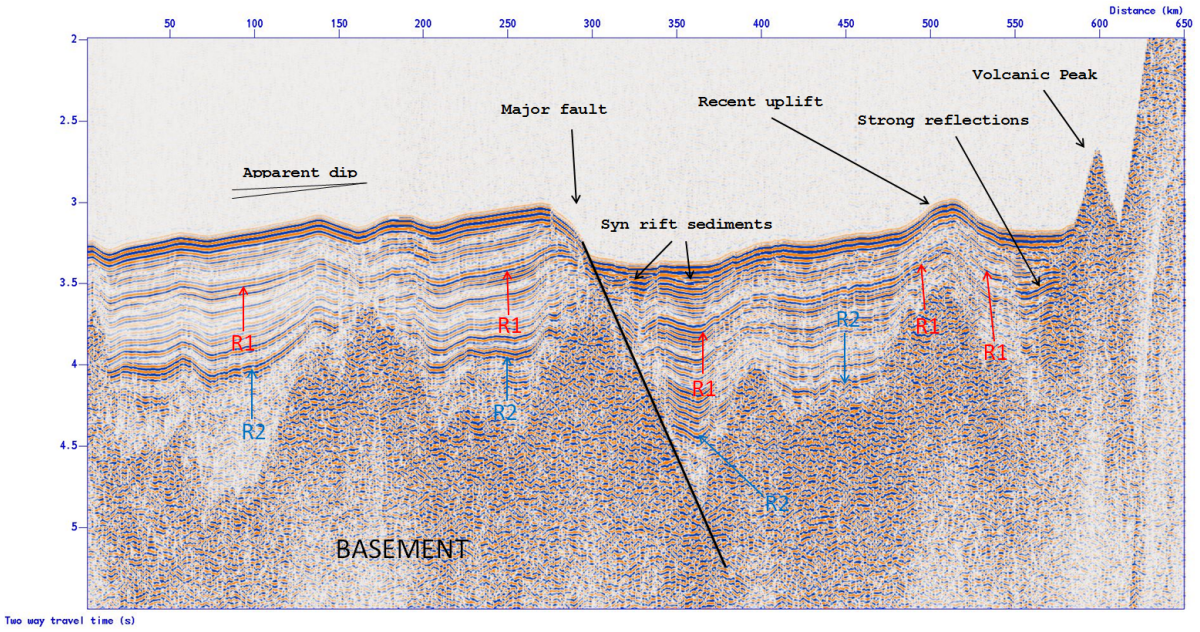

Figure 10.4: Interpretation of SCS data over the Greenland Basin and the Jan Mayen Fracture Zone.

In the middle of profile (km 60) a major fault is present. It cuts through all of the sedimentary layers, so the faulting must be of recent age. The sea floor is roughly displaced 200 meter vertically across the fault. Some bending is seen among the sedimentary layers on the foot wall. Erosional truncation is seen in on the sea bed at this local high. In the through a small amount of syn rift sediments are present. The fault could be an extensional feature correlated with the observed apparent dip of the sediments.

Next to the Eggvin Bank and above the JMFZ is a ∼300 m high peak. In its vicinity are high amplitude reflectors within the sedimentary unit. These are interpreted as eroded volcanic material from the Eggvin Bank, or possibly minor sills extending out from the fracture zone. Further north (km 100) a swell has occurred over one basement peak and the seabed is elevated about 150 m. Basement movement is visible through the whole overlying sedimentary package, all the way up to the seabed. This sedimentary layering is different compared to elsewhere along the profile.

10.3 Geological Discussion

10.3.1 Iceland Plateau

In the magnetic data a typical oceanic crust is observed south of the Eggvin Bank. OBS 1 was deployed on crust corresponding to magnetic anomaly C5, 10.3 Ma. The shallow bathymetry and general trend of positive gravity anomalies over the Iceland Plateau indicate a thickened crust. Kodaira et al. (1998) mapped a 9 km thick crystalline crust further south on the Iceland Plateau. Average thickness for normal oceanic crust is about 7 km (White, 1992). The deeper

parts of the Iceland Plateau was little constrained by the seismic coverage. Nevertheless, modeled thickness is 8 – 8.5 km. In Figure 10.5 two 1-D velocity profiles from the Iceland Plateau are evaluated. 1D P-wave velocity distribution correlates well with average normal crust (White, 1992) and with the study of Kodaira et al. (1998). Figure 10.6 shows the crustal structure of Iceland Plateau as presented by Kodaira et al. (1998).

Layer II-A has low P-wave velocities. However, there are other 1D-velocity profiles along the survey line (e.g., km 250 and 265) that have slightly higher II-A velocities. Layer II-A has Poisson's ratio of 0.35. The layer compare well with oceanic layer 2-A on the Iceland Plateau (Kodaira et al., 1998). P-wave velocities of II-B compare well with lab measurements of diabase (Christensen, 1996) as well as oceanic layer 2-B further south on the Iceland Plateau (Kodaira et al., 1998). However, the Poisson's ratio (0.35) is higher. Layer II-A and II-B both have the same high Poisson's ratio which correlates with the average serpentinite trend (Carlson and Miller, 1997). Only one single value of Poisson's ratio was assigned each layer over the whole profile. The structures of the Eggvin Bank has most likely affected the value much more than the peripheral structures of Iceland Plateau. Nevertheless, further south on the Iceland Plateau porosity in the upper crystalline crust was given as an explanation for low P-wave velocities (Kodaira et al., 1997, 1998) and high Poisson's Ratios (Mjelde et al., 2002a, 2007).

P-wave velocities and Poisson's ratio of layer III corresponds well with lab measurements of gabbro (Christensen, 1996), as well as investigations on Iceland Plateau (Kodaira et al., 1998; Mjelde et al., 2002a). Estimates was made from good seismic coverage. On the other hand, the Moho and upper mantle were not well constrained. The upper mantle was only sampled by one P_n phase and one PSS_n phase. Nevertheless, a good fit of travel times was achieved for the P-waves (cf. Figure B.6, Appendix B.1). A fairly good fit was obtained for the S-wave (cf. Figure B.17, Appendix B.2). A remarkably low velocity was modeled in the upper mantle. This is most likely an artifact of velocity modeling, as nodes were little constrained.

10.3.2 Eggvin Bank

Comparison to oceanic crust

Velocities on the Eggvin Bank compare well with those of the Iceland Plateau, Figure 10.6 and 10.7. The thickness of layer II-A and II-B increase from the Iceland Plateau to the Eggvin Bank. The thickness of II-A increases from $\sim$ 1 km to $\sim$ 1.5 km. Thickness of II-B increases from $\sim$ 2 km to $\sim$ 3 km. These layers are thicker than in average oceanic crust (White, 1992). Variation in thickness of layer II-A and II-B are within the limits of what has been documented further south (Kodaira et al., 1997, 1998). Velocities of II-A and II-B are generally lower than the equivalents presented by Kodaira et al. (1998).

Poisson's ratio of II-A and II-B (0.35) is higher than laboratory estimates of oceanic layer 2-A (basalts) and 2-B (diabase) presented by Christensen (1996), Figure 10.7B. Estimates at 600MPa (sufficiently high pressures such that porosity is eliminated) are 0.294 $\pm$0.015 for basalts and 0.279 $\pm$0.016 for diabase. II-A compares with the other studies of Iceland Plateau (Mjelde et al., 2002a, 2007) but II-B has a higher Poisson's ratio, Figure 10.7C. High Poisson's

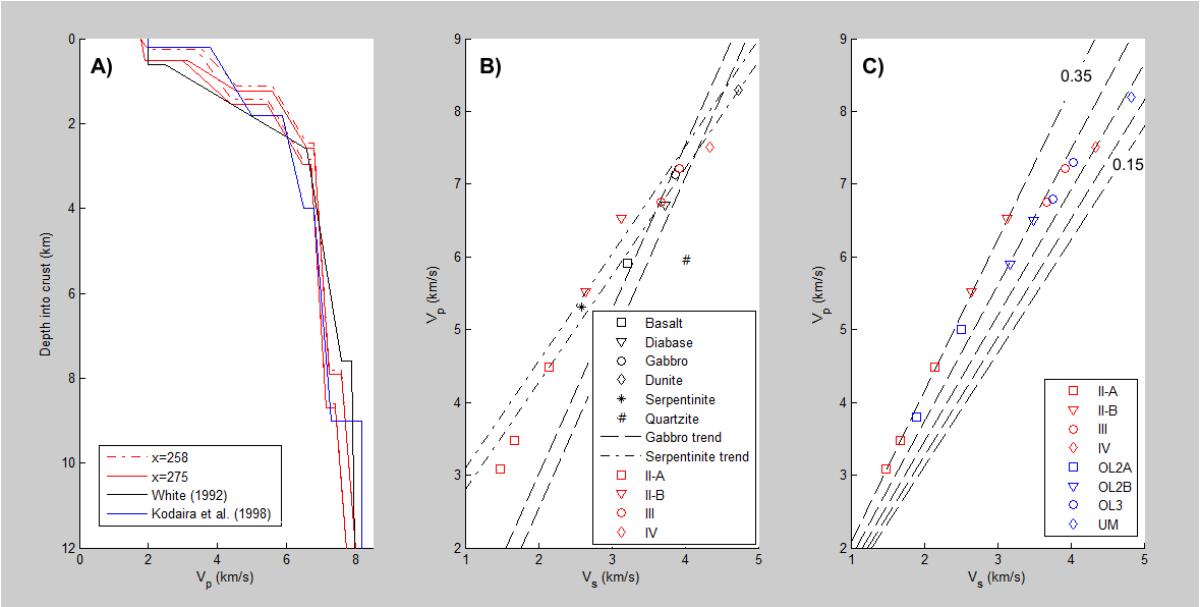

Figure 10.5: Velocity profiles from the Iceland Plateau, sampled at distance 258 and 275 km along the survey line. A): 1D-velocity profile compared with average crust (White, 1992) and a study further south on the plateau (Kodaira et al., 1998). B): V_p - V_s plot of velocities. Results (red color) are compared with laboratory measurements estimated for 600 MPa pressure (Christensen, 1996), plotted with black color. Average gabbro and serpentinite trends (Carlson and Miller, 1997) are also added. C): Layer velocities are compared to the velocity layers mapped by Kodaira et al. (1998) and Mjelde et al. (2002a), marked with blue color. Poisson's ratio is indicated by stippled lines, counterclockwise from 0.15 to 0.35 at intervals of 0.05. In "A)" two lines are plotted for each 1D velocity profile extracted from the model. These are the two extremes defined by the uncertainties of velocities and boundaries. Average values are used for the other profiles. In "B)" and "C)" average values are plotted.

ratios in II-A were ascribed effects of porosity and cracks in the extrusive layer (Mjelde et al., 2007). Extensive volcanic activity could have yielded porosity and cracks in both layer II-A and II-B. Both layers falls on the estimated curves of serpentinization (Carlson and Miller, 1997). It is also possible that these layers has underwent a metamorphic change as seawater has penetrated down into the rocks. More extensively magmatic activity on the Eggvin Bank compared to the Iceland Plateau could have caused higher crack porosity in the layers. Furthermore, these cracks could have made it possible for seawater to penetrate down to layer II-B. Extensive serpentinization of layer II-B could be an explanation of the anomalous values on the Eggvin Bank and the differences with the values on the Iceland Plateau.

P-wave velocity and Poisson's ratio of layer III corresponds to laboratory measurements of gabbro (Christensen, 1996; Carlson and Miller, 1997), Figure 10.7B. Velocities as well as thickness correlates with the lower crust in the Iceland Plateau, as mapped in this and in other studies (Kodaira et al., 1997, 1998; Mjelde et al., 2002a, 2007), Figure 10.7C.

Poisson's ratio of 0.25 in the upper mantle is typical. The abnormal P-wave velocity, obtained at distance 130 km along the survey line, was disregarded because of low seismic coverage (see

ray density plot in Figure 9.2). Typical P-wave velocities obtained in the upper mantle were 7.81 - 7.85 km/s. On average the values are slightly lower than 8.2 km/s presented by Kodaira et al. (1998), Figure 10.6. This could be ascribed anisotropic effects caused by mineral orientation in the upper mantle. Determined by the orientation of olivine, fast direction is away form spreading axis and slow direction is parallel with axis (Christensen, 2004). Eggvin Bank upper mantle could have been formed entirely at spreading along northern Kolbeinsey Ridge, lower values should then be expected, compared to the studies of Kodaira et al. (1998), that conducted surveys along the fast direction. Average anisotropi has been estimated to give velocity effects of $\pm$ 5% (Christensen, 2004). However, (Kodaira et al., 1998) also mapped 8.1 km/s parallel with the Kolbeinsey spreading ridge. According to White (1992) average P-wave velocities in the upper mantle range between 7.9 and 8.1 km/s. Obtained upper mantle velocities (excluded anomalous values) are slightly low. Velocities compare, nevertheless, well with peridotitic composition.

Comparison to Jan Mayen Micro Continent

Figure 10.6 presents the crustal transect (Kodaira et al., 1998) across the westside of Jan Mayen Micro Continent (JMMC). The former idea that the crust under the Eggvin Bank could be intruded continental crust extending out from JMMC (Evans and Sacks, 1979; Campsie et al., 1990) is investigated in Figure 10.8. Layer II-B and III from the Eggvin Bank are compared with the upper and lower continental crust of the Jan Mayen Ridge. Average P-wave velocities from Kodaira et al. (1998) are plotted with Poisson's ratios form Mjelde et al. (2007). Iceland Plateau and laboratory estimates are also added for comparison. Both the lower and upper continental crust have in general higher S-wave velocities than mafic rocks and layer II-B and III of the Eggvin Bank. P-wave velocities of the lower continental crust are low compared to the gabbroic oceanic layer. Oceanic layer 2-B as mapped in the Iceland Plateau is not to different from the upper continental crust. However, a great difference is seen with layer II-B on the Eggvin Bank, because of its anomalously high Poisson's ratio. The bottom of the lower continental crust clearly differ from the bottom structures of layer III of the Eggvin Bank, as well bottom structures of oceanic layer 3 in the Iceland Plateau. The Eggvin Bank velocities do not resemble those of the JMMC.

Comparison to crust beneath Jan Mayen

Figure 10.9 presents a line from Kandilarov et al. (2012) that mapps the structures below the Jan Mayen island. The northern boundary of the JMMC was determined to be at distance 90 km along the survey line. In between this boundary to the south and the JMFZ to the north, the crust was determined to be of complex nature. Part of it similar to oceanic crust found beneath Iceland. Crustal velocities are also similar to those of the Jan Mayen Ridge. The two lowermost crustal layers, denoted Layer 5 and 6, range in between 6.20 – 6.60 km/s and 6.70 – 6.90 km/s, respectively. Compared to the Eggvin Bank, layer 5 is similar to layer II-B while Layer 6 has lower velocities than layer III. In the vicinity of the Jan Mayen Fracture Zone velocities of the lowermost crust increase to high values (6.50 – 6.90 km/s in Layer 5 and 7.20 – 7.50 km/s in Layer 6). Underneath the island and to the northwest, upper mantle velocities ranges from 7.50 to 7.80 km/s. These compares with those under the Eggvin Bank, 7.81 – 7.85 km/s. Kandilarov

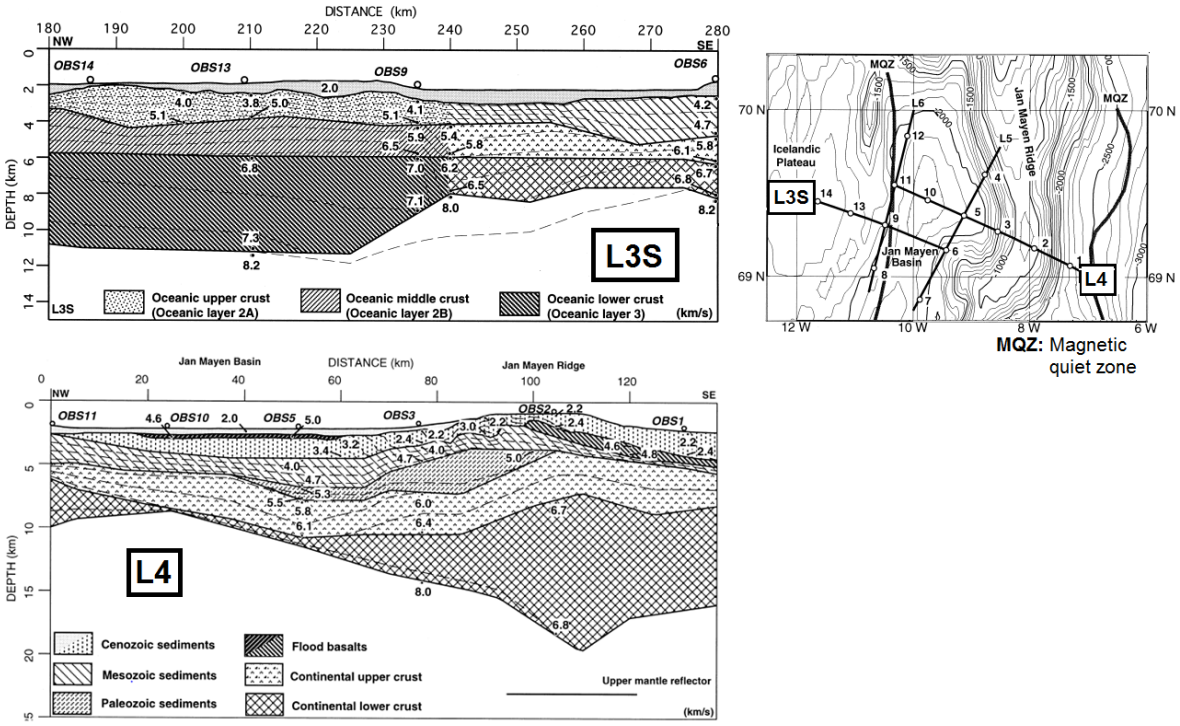

Figure 10.6: Crust in Iceland Plateau and on the Jan Mayen Micro Continent, modified from Kodaira et al. (1998).

et al. (2012) mapped the Moho right under Jan Mayen to be shallow. This feature could possibly correlate with the shallow feature under the central parts of the Eggvin Bank. It could have been a tectonic feature in the crust orientated parallel with the JMFZ. However, considering how the thickened crust coincides with the each seamount, it is more likely to believe that the thick crust is directly ascribed to the presence of the seamounts.

Fe-depleted mantle source?

Haase et al. (2003) ascribed the magmatism responsible for the shallow bathymetry of the Eggvin Bank, a Fe-depleted and less dense mantle source. Mg-Fe substitution in pyroxenes and olivines will lower the Poisson's ratio in rocks (Christensen, 1996). Upper mantle peridotites are rich in both pyroxenes and olivines. Pyroxenes are a major constituent in gabbros as well. Furthermore, Mjelde et al. (2002a) interpreted relatively low Poisson's ratio for all crustal layers in the Iceland Plateau in terms of gabbroic composition with increased Mg content. However, no anomalously low value were detected in layer III nor in the upper mantle (poorly resolved areas are not considered). Estimated Poisson's ratio in the lower crust and upper mantle under Eggvin Bank were 0.29 and 0.25, respectively. These values correspond to a normal peridotitic composition. The inaccuracy of S-wave modeling in this study makes it unlikely that it would be possible to detect Fe-depletion in the crust and upper mantle.

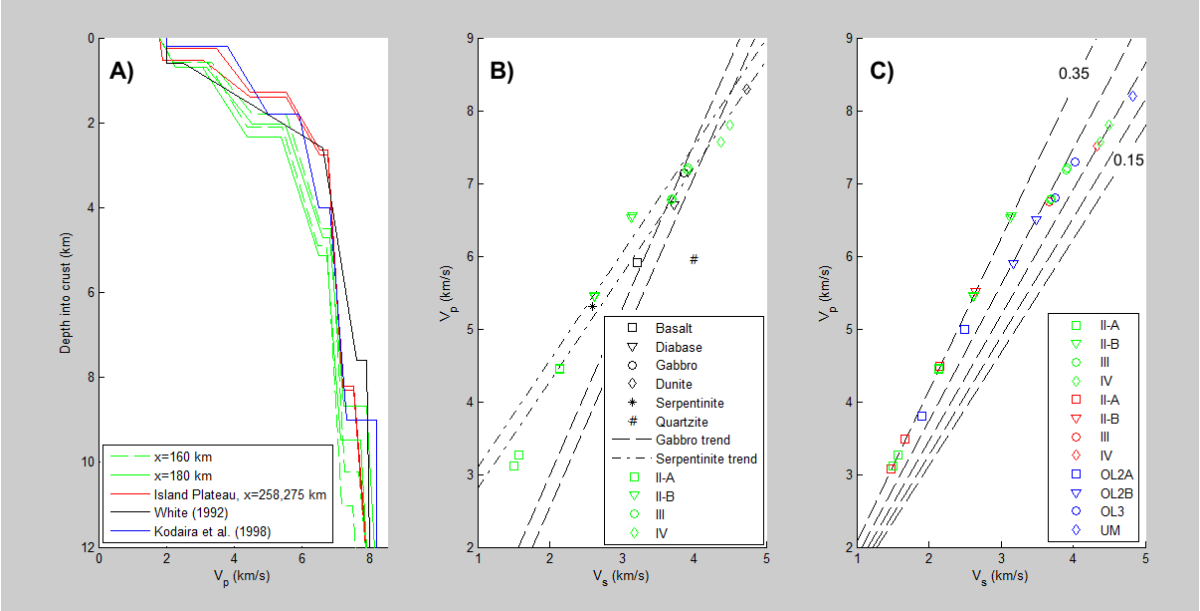

Figure 10.7: 1D velocity profiles from the Eggvin Bank are compared to the Iceland Plateau. Velocity profiles are sampled at distance 160 and 180 km along the survey line. A): 1D-velocity profiles compared to average crust (White, 1992), Iceland Plateau (this study) and Iceland Plateau mapped by Kodaira et al. (1998). B): V_p – V_s plot of velocities. Results are compared with laboratory measurements estimated for 600 MPa pressure (Christensen, 1996), colored in black. Comparison is also done with average gabbro and serpentine trends (Carlson and Miller, 1997). C): V_p – V_s plot of Eggvin Bank velocities (green color) compared to velocities from the Iceland Plateau. Iceland Plateau velocities from this study are colored red while velocities from the studies of Kodaira et al. (1998) and Mjelde et al. (2002a) are colored blue. Poisson's ratio is indicated by stippled lines, counterclockwise from 0.15 to 0.35 at intervals of 0.05. In "A)" two lines are plotted for each 1D velocity profile extracted from the model. These are the two extremes defined by the uncertainties of velocities and boundaries. Average values are used for the other profiles. In "B)" and "C)" average values are plotted.

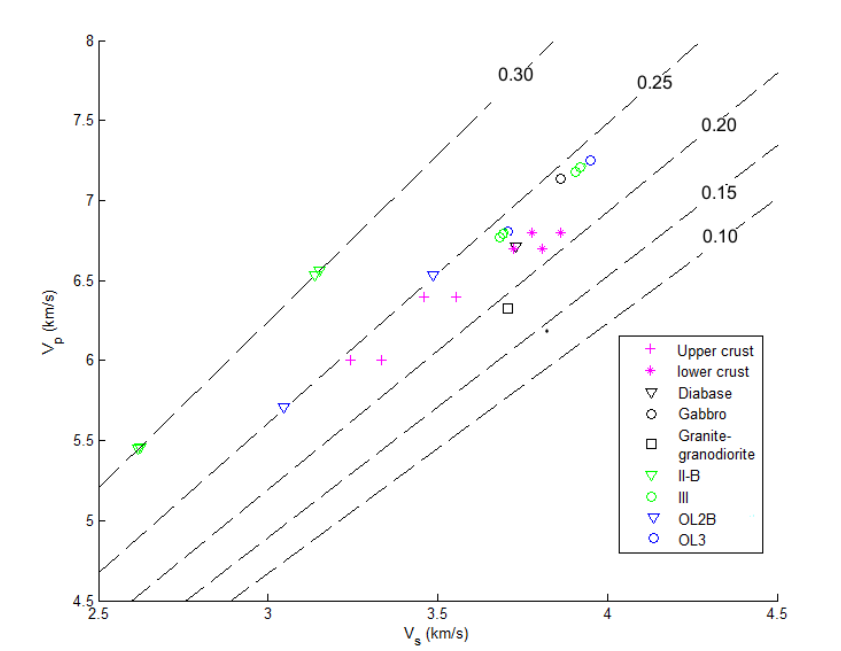

Figure 10.8: Velocities of Layer II-B and III from the Eggvin Bank are compared to continental crust of JMMC in a V_p - V_s plot. Eggvin Bank velocities are colored green. Upper and lower continental crust from the Jan Mayen Ridge (Kodaira et al., 1998; Mjelde et al., 2007) are plotted with magenta color. Average values from laboratory measurements (Christensen, 1996) are colored in black. Iceland Plateau (Kodaira et al., 1998; Mjelde et al., 2002a) are also added for comparison, colored in blue. Poisson's ratio is indicated by stippled lines.

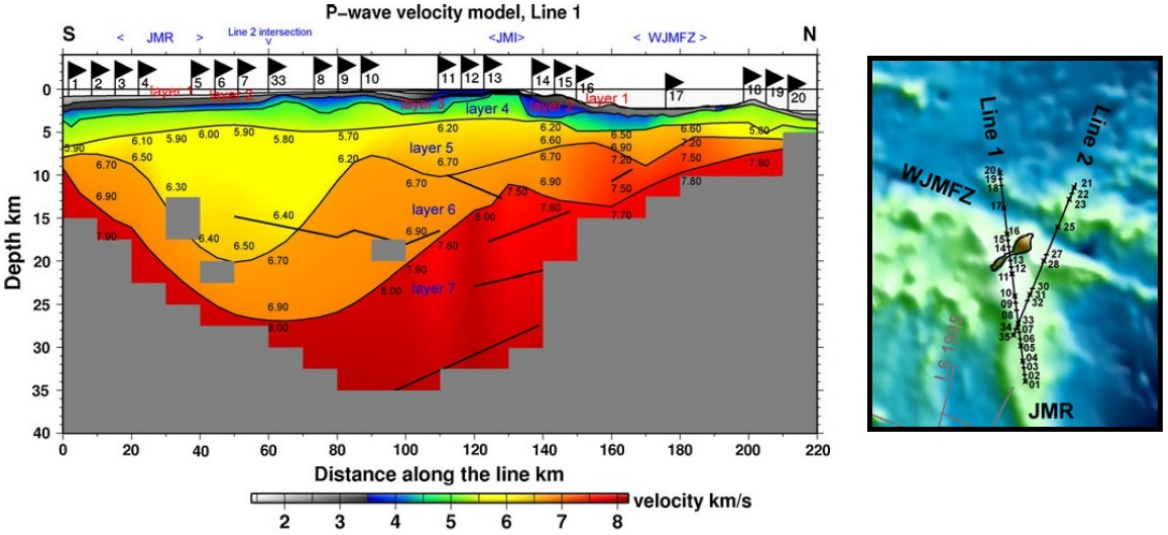

Figure 10.9: Crustal structure across Jan Mayen island, modified from (Kandilarov et al., 2012). On the right side the orientation of the crustal transect is indicated relative to Jan Mayen.

Implications of recent volcanism

Mertz et al. (2004) identified two types of seamounts on the Eggvin Bank, tholeiitic near-axis lavas (< 0.1 Ma) and transitional-to-alkaline off-axis seamount lavas (0.6 - 0.7 Ma). First type is geochemically similar to Kolbeinsey Ridge basalts while the second is geochemically similar to other alkaline basalts in the Jan Mayen area (see also Figure 2.5, Section 2.3). One of the investigated off-axis seamounts ($\sim 71^0$19'N and $\sim 11^0$09'W) is located on top of seafloor which is evidently older, considering the distance away from the spreading ridge.

In the magnetic data, the Eggvin Bank has weak anomalies aligned with the Kolbeinsey Ridge. Because of low data coverage over the bank it is not possible to determine with certainty if these are regular seafloor anomalies and what the age of the crust is. Furthermore, it is not possible to tell if there are secondary magmatic features that interrupts the regular pattern. Bathymety shows a clear asymmetry about the Kolbeinsey Ridge. The asymmetry of the volcanic peaks could indicate that these are secondary to the creation of the crust at the spreading ridge. However, asymmetric spreading has occurred and been documented in the North Atlantic Sea (e.g., Mosar et al., 2002).

In the SCS seismic, the sediments on the Eggvin Bank are disrupted and inclined towards the big seamounts. The smaller seamounts do not disturb the sedimentary unit the same way. This fact could imply that the small volcanic peaks were created together with the crust while the big seamounts could have been created at a later stage. The sediments in the Iceland Plateau, however, do not incline towards the southernmost big seamount of the Eggvin Bank.

The near-axis and off-axis basalts have different geochemical composition. Alkali basalts are somewhat enriched in Na_2O and K_2O compared to normal depleted thoeliitic composition, but these differences can not be distinguished by seismic velocities. A notifiable thickening of layer II-A and II-B coincides with the shallow bathymetry over Eggvin Bank. It could be an feature caused by more volcanism and extrusive material in the Eggvin Bank compared to the Iceland Plateau. The crust directly underneath the big seamounts is thicker. It appears to be directly related to their presence. It is not understood whether these features derive from creation along the spreading axis or if they are caused by secondary volcanism.

10.3.3 Greenland Basin and the Jan Mayen Fracture Zone

The crustal thickness and the velocity distribution of the Greenland Basin were weakly constrained by only two P_n phases, recorded in OBS 3 and 4. Two PSS_n phases, also recorded in OBS 3 and 4, were used to constrain the Poison's ratio. An additional PPS_n phase from OBS 3 were also traced through the upper mantle. It was possible to make an estimate of the upper mantle velocities in the vicinity of the transform (7.9$\pm$0.2 – 8.1$\pm$0.2 km/s). Furthermore, a substantial change in crustal thickness between the Greenland Basin and the Eggvin Bank could be detected, which is also indicated by bathymetry and gravity anomalies. The crystalline thickness was estimated 4.0 $\pm$1.2 km. The survey line transverses magnetic anomaly C5 and C7 in the Greenland Basin, 10.3 – 25.0 Ma. A very different crustal thickness is observed compared to the crust of comparable age on the Iceland Plateau.

To the west of the survey line, crustal thickness is documented to be 4.8 km with upper mantle velocities about 8.0 km/s (Voss and Jokat, 2007), for crust 33.3 – 39.4 Ma. To the east of the survey line, Kandilarov et al. (2012) reported a slightly thicker crust of $\sim$ 6 km which increases to $\sim$ 10 km towards the Mohns Ridge. Anomalously thick crust was ascribed to an effect of the Jan Mayen Plateau, a magmatic anomaly in the vicinity of the Mohns Ridge. Velocities in the upper mantle were mapped 7.8 km/s. Klingelhofer and Geli (2000) documented that the crustal thickness at latitude $\sim 72^0$N on the conjugate side of the Mohns Ridge was 4.0 ± 0.5 km. This was done for 0-22.4 Ma oceanic crust. The upper mantle velocities were estimated to be 7.4 – 7.8 km/s.

Good correlation with nearby studies is observed for the gross crustal thickness. Velocities correlate with the crust to the west (Voss and Jokat, 2007), but is higher than to the east (Kandilarov et al., 2012; Klingelhofer and Geli, 2000). Normal P-wave velocity ($\sim$8 km/s) and Poisson's ratio (0.25) for the upper mantle indicate peridotitic composition. The little data available do not indicate serpentinization of mantle peridotites, which is often present along transform zones according to Christensen (2004) and references therein.

A major fault observed in the seismic coincides with an uplift seen in the bathymetry and a strong positive anomaly in the gravity. The 50 km long and 30-40 km wide uplift in the bathymetry extends from the easternmost part of Logi Ridge, along its lineament. Because of low seismic coverage it is not possible to tell anything about how this feature propagates into the deeper crust.

Chapter 11

Conclusions and Future Work

11.1 Conclusions

Optimal results of modeling were obtained with a four layered model (I: Sediments. II-A: Upper crust. II-B: Middle crust. III: Lower crust) over a half-space (IV: Upper mantle). Structures in the Eggvin Bank and upper crust of Iceland Plateau were well resolved. P-waves were modeled with a good fit (χ^2_N = 0.870). The fit of the S-waves, however, were not very exact (χ^2_N = 4.020 for PSS-waves and χ^2_N = 2.317 for PPS-waves). The model was assessed with resolution estimates, which made it possible to disregard certain obtained anomalous values, e.g. low mantle velocities in the Eggvin Bank (7.45 km/s) and under the Iceland Plateau (7.50 km/s).

Crystalline thickness of Eggvin Bank was modeled to be 11 km thick underneath (and including) the big seamounts. In the central parts of the bank thickness was estimated to 8 – 9 km. Iceland Plateau crust was estimated to be 8 km thick, though Moho was little constrained. The crystalline structures of the Greenland Basin were poorly constrained by the seismic, because it was not possible to recover recordings from OBS 5. However, a substantial change in gross crustal thickness from the Eggvin Bank was identified. In the vicinity of the Jan Mayen Fracture Zone, the Greenland Basin crystalline crust was modeled to be 4.0 $\pm$1.2 km thick. Depth conversion gave a thicker sedimentary unitin the Greenland Basin (0.2-2km) than on the Eggvin Bank and Iceland Plateau (0-0.5km). The obtained gross structures of the Greenland Basin correlate well with other studies (Voss and Jokat, 2007; Klingelhofer and Geli, 2000).

In the Eggvin Bank and Iceland Plateau, average P-wave velocities in the upper and middle crust were estimated to be 3.45 - 4.6 0 km/s and 5.50 – 6.55 km/s, for layer II-A and II-B respectively. Poisson's ratios were estimated to be 0.35 for both layers. The relatively low P-wave velocities and high Poisson's ratio were ascribed to high crack porosity in extrusive and intrusive volcanic rocks. Velocities in both layers coincides with the serpentinite trend (Carlson and Miller, 1997). Serpentinization is also a possible cause for obtained velocity values, especially for layer II-B. P-wave velocities of the lower crust, layer III, were estimated to range in between 6.80 - 7.20 km/s. Poisson's ratio was estimated to be 0.29. Velocities correlate well with laboratory measurements of gabbro (Christensen, 1996). Upper mantle P-wave velocities were estimated to be around 8.0 $\pm$0.2 km/s under the Greenland Basin and 7.80 – 7.85 km/s

under the Eggvin Bank. Because of low seismic coverage, upper mantle velocities under the Iceland Plateau was not determined. Poisson's ratio in the Upper mantle was estimated to be 0.25. Velocities indicate normal perioditic composition in the upper mantle underneath Greenland Basin and Eggvin Bank.

The mapped part of Iceland Plateau has a thickened crust with velocities similar to what has been documented further south (Kodaira et al., 1997, 1998; Mjelde et al., 2002a, 2007). The Eggvin Bank have a crust similar to oceanic crust, in particular the Iceland Plateau. Magnetic anomalies, even though the regional data has low coverage over Eggvin Bank, indicate alignment of magnetic anomalies parallel with Kolbeinsey Ridge. The obtained velocities do not resemble those of the Jan Mayen Micro Continent nor those underneath Jan Mayen. A thickening of layer II-A and II-B occurs on the Eggvin Bank, compared to the Iceland Plateau. This was interpreted as a result of extensive volcanic activity. Thickened crust coincides with the major seamounts, and it was ascribed directly their presence. Velocities in the upper mantle are slightly lower than average values (White, 1992) and velocities under the Iceland Plateau (Kodaira et al., 1998), but they compare well with underneath Jan Mayen (Kandilarov et al., 2012).

11.2 Future work

11.2.1 Seismic analysis of anisotropy

Analysis of S-waves in the two horizontal components could be done in a polarization analysis, e.g. hodogram, to identify anisotropy in Eggvin Bank crust. At low pressure anisotropy is caused by oriented crack porosity (Christensen, 2004). High Poisson's ratio was obtained for the upper crustal layers in this study. High Poisson's ratio in the upper crust could indicate crack porosity (e.g., Mjelde et al., 2002a). It would be interesting to see if it is possible to identify (1) if the stress field and crack porosity are aligned with the Kolbeinsey Ridge spreading axis or (2) if an orientated related to extension over the Jan Mayen Fracture Zone is present. Extensional feature across the Jan Mayen Fracture Zone was observed in single-channel streamer seismic in the Greenland Basin, implied by the over-all apparent northward dip in the sedimentary layering. As some authors (e.g., Havskov and Atakan, 1991; Gernigon et al., 2008; Kandilarov et al., 2012) suggest that the volcanism on Jan Mayen is caused by minor spreading -or leakage- along the JMFZ, a study related to this would be interesting.

11.2.2 Including recordings from magnetometer and gravimeter into model

Magnetic and gravimetric data was also acquired during the East Greenland 2011 Survey. Density and magnetic properties could be assigned to the geometry of the velocity model, and a better constraint on lithology could be obtained.

11.2.3 Constraining the crust of Greenland Basin despite low coverage

Despite the low seimic coverage and poorly resolved structures in the Greenland Basin, it is believed that the crust could be better constrained by choosing alternative approaches. Information about the crustal structure nearby has been provided by Kandilarov et al. (2012) and Voss et al. (2009). Using these studies and fitting an apparent crustal structure together with recordings of gravity and magnetism, could yield a better constrained crustal structure. Then the major fault, coinciding with the bathymetric uplift and gravity anomaly (see aslo Section 10.2.2 and 10.3.3), could be investigated further.

11.2.4 Direct model assessment with a tomographic approach

It was identified during model evaluation in Section 9.2 that node parametrization was not optimal. Details not accounted for by the data had been incorporated into the model. Furthermore, details in the data could also have been excluded from the model. As most of the phases have been identified, it would be interesting to try a fully tomographic approach to find a minimum model. Inversion should be done on a grid with regular and sparse node placement, where boundary and velocity nodes are uniformly spread out. Zelt (1999) argues how direct model assessment is the best way to test reliability of an model. To see how a model which is based purely on inversion compares with the obtained model, could give indications to which of the model features that are likely real and which are likely arbitrary.

Bibliography

Au, D. and Clowes, R. M. (1984). Shear-wave velocity structure of the oceanic lithosphere from ocean bottom seismometer studies. *Geophysical Journal International*, 77:105–123.

Bevington, P. and Robinson, D. (2003). *Data reduction and error analysis for the physical sciences. 3rd ed.* New York: McGraw-Hill.

Breivik, A. J., Mjelde, R., Faleide, J. I., and Murai, Y. (2012). The eastern Jan Mayen micro-continent volcanic margin. *Geophysical Journal International*, 188(3):798–818.

Campsie, J., Rasmussen, M. H., Kovacs, L. C., Dittmer, F., Bailey, J. C., Hansen, N. O., Laurscn, J., and Johnson, L. (1990). Chronology and evolution of the northern Iceland Plateau. *Polar Research*, 8:237–243.

Cande, S. C. and Kent, D. V. (1995). Revised calibration of the geomagnetic polarity timescale for the Late Cretaceous and Cenozoic. *Journal of Geophysical Research: Solid Earth*, 100:6093–6095.

Carlson, R. and Miller, D. (1997). A new assessment of the abundance of serpentinite in the oceanic crust. *Geophysical Research Letters*, 24(4):457–460.

Cherkis, N., Steinmetz, S., Schreiber, R., Thiede, J., and Theiner, J. (1994). Vesteris Seamount: An enigma in the Greenland Basin. *Marine Geophysical Researches*, 16(4):287–301.

Christensen, N. (1996). Poisson's ratio and crustal seismology. *Journal of Geophysical Research*, 101(B2):3139–3156.

Christensen, N. (2004). Serpentinites, Peridotites, and Seismology. *International Geology Review*, 46:795–816.

Cliet, C. and Dubesset, M. (1988). Polarization analysis in three-component seismics. *Transactions of the American Geophysical Union*, 34:101–119.

CREWES (2005). Zoeppritz Explorer 2.2 [WWW] University of Calgary. Available from: http://www.crewes.org/ResearchLinks/ExplorerPrograms/ [Accessed 11/05/14].

Del Grosso, V. A. (1974). New equation for the speed of sound in natural waters (with comparisons to other equations). *The Journal of the Acoustical Society of America*, 56(4):1084–1091.

Eldholm, O. and Talwani, M. (1982). *The passive margins of northern Europe and east-Greenland. In: Scrutton, R.A. (eds.) Dynamics of Passive Margins* . Washington: American Geophysical Union, pp. 30-44.

Engen, O., Faleide, J., and Dyreng, T. (2008). Opening of the Fram Strait gateway: A review of plate tectonic constraints. *Tectonophysics*, 450(1–4):51 – 69.

Engen, O., Frazer, N., Wessel, P., and Faleide, J. I. (2006). Prediction of sediment thickness in the Norwegian–Greenland Sea from gravity inversion. *Journal of Geophysical Research*, 111:0148–0227.

Evans, J. and Sacks, I. (1979). Deep structure of the Iceland Plateau. *Journal of Geophysical Research*, 84:6859–6866.

Fowler, C. (2005). *The Solid Earth: An introduction to Global Geophysics. 2nd ed.* Cambridge: Cambridge University Press.

Gaina, C., Gernigon, L., and Ball, P. (2009). Palaeocene - Recent plate boundaries in the NE Atlantic and the formation of the Jan Mayen microcontinent. *Journal of the Geological Society, London*, 166:601–616.

Gelius, L.-J. and Johansen, T. (2010). *Petroleum geophysics*. Bergen: UniGEO AS.

Gercek, H. (2007). Poisson's ratio values for rocks. *International Journal of Rock Mechanics and Mining Sciences*, 44(1):1–13.

Gernigon, L., Olesen, O., Ebbing, J., Wienecke, S., Gaina, C., Mogaard, J. O., Sand, M., and Myklebust, R. (2008). Geophysical insights and early spreading history in the vicinity of the Jan Mayen Fracture Zone, Norwegian–Greenland Sea. *Tectonophysics*, 468(1–4):185 – 205.

Haase, K. and Devey, C. (1994). The Petrology and Geochemistry of Vesteris Seamount, Greenland Basin—an Intraplate Alkaline Volcano of Non-Plume Origin. *Journal of Petrology*, 35(2):295–328.

Haase, K., Devey, D., and Wieneke, M. (2003). Magmatic processes and mantle heterogeneity beneath the slow-spreading northern Kolbeinsey Ridge segment, North Atlantic. *Contributions to Mineralogy and Petrology*, 144:428–448.

Haase, K. M., Devey, C. W., Mertz, D. F., Stoffers, P., and Garbe-Schönberg, D. (1996). Geochemistry of lavas from Mohns Ridge, Norwegian-Greenland Sea: implications for melting conditions and magma sources near Jan Mayen. *Contributions to Mineralogy and Petrology*, 123(3):223–237.

Havskov, J. and Atakan, K. (1991). Seismicity and volcanism of Jan Mayen Island. *Terra Nova*, 3(5):517–526.

Imsland, P. (1980). *The petrology of the volcanic Island Jan Mayen, Arctic Ocean*. Reykjavik: Nordic Volcanological Institute.

Imsland, P. (1986). The volcanic eruption on Jan Mayen, January 1985: Interaction between a volcanic island and a fracture zone. *Journal of Volcanology and Geothermal Research*, 28:45 – 53.

Jakobsson, M., Mayer, L., Coakley, B., Dowdeswell, J. A., Forbes, S., Fridman, B., Hodnesdal, H., Noormets, R., Pedersen, R., Rebesco, M., Schenke, H. W., Zarayskaya, Y., Accettella, D., Armstrong, A., Anderson, R. M., Bienhoff, P., Camerlenghi, A., Church, I., Edwards, M., Gardner, J. V., Hall, J. K., Hell, B., Hestvik, O., Kristoffersen, Y., Marcussen, C., Mohammad, R., Mosher, D., Nghiem, S. V., Pedrosa, M. T., Travaglini, P. G., and Weatherall, P. (2012). The International Bathymetric Chart of the Arctic Ocean (IBCAO) Version 3.0. *Geophysical Research Letters*, 39(12).

Johnson, G. and Campsie, J. (1976). Morphology and structure of the Western Jan Mayen Fracture Zone. *Norsk Polarinstitutt Årbok 1974: 69–81*.

Jurkevics, A. (1988). Polarization analysis of three-component array data. *Bulletin of the Seismological Society of America*, 78(5):1725–1743.

Kanasewich, E. R. (1981). Time sequence analysis in geophysics. 3rd ed. *Alberta: The University of Alberta Press*.

Kandilarov, A., Mjelde, R., , R. B., Hellevang, B., Papenberg, C., Petersen, C. J., Planert, L., and Flueh, E. (2012). The northern boundary of the Jan Mayen microcontinent, North Atlantic determined from ocean bottom seismic, multichannel seismic, and gravity data. *Marine Geophysical Research*, 33(1):55–76.

Klingelhofer, F. and Geli, L. (2000). Geophysical and geochernical constraints on crustal accretion at the very-slow spreading Mohns Ridge. *Geophysical Research Letters*, 27:1547–1550.

Kodaira, S., Mjelde, R., Gunnarsson, K., Shiobara, H., and Shimamura, H. (1997). Crustal structure of the Kolbeinsey Ridge, North Atlantic, obtained by use of ocean bottom seismographs. *Journal of Geophysical Research: Solid Earth*, 102(B2):3131–3151.

Kodaira, S., Mjelde, R., Gunnarsson, K., Shiobara, H., and Shimamura, H. (1998). Structure of the Jan Mayen microcontinent and implications for its evolution. *Geophysical Journal International*, 132:383–400.

Maercklin, N. (2007). SUPOLAR and SUPOFILT: SU programs for polarization analysis and filtering of three-component data [WWW]. Available from: http://http://purl.org/net/nils/man/supolar. [Accessed 01/03/14].

Mertz, D., Sharp, W., and Haase, K. (2004). Volcanism on the Eggvin Bank (Central Norwegian-Greenland Sea, Latitude $\sim 71^0$N): Age, Source and Relationship to The Iceland and Putative Jan Mayen plumes. *Journal of Geodynamics*, 38:57–83.

Mjelde, R., Aurvaag, R., Kodaira, S., Shimamura, H., Gunnarsson, K., Nakanishi, A., and Shiobara, H. (2002a). Vp/Vs-ratios from the central Kolbeinsey Ridge to the Jan Mayen Basin, North Atlantic; implications for lithology, porosity and present-day stress field. *Marine Geophysical Researches*, 23:125–145.

Mjelde, R., Eckhoff, I., Solbakken, S., Kodaira, S., Shimamura, H., Gunnarsson, K., Nakanishi, A., and Shiobara, H. (2007). Gravity and S-wave modelling across the Jan Mayen Ridge,

North Atlantic; implications for crustal lithology. *Marine Geophysical Researches*, 28(1):27–41.

Mjelde, R., Timenes, T., Shimamura, H., Kanazawa, T., Shiobara3, H., Kodaira, S., and Nakanishi, N. (2002b). Acquisition, processing and analysis of densely sampled P- and S-wave OBS-data on the mid-Norwegian Margin, NE Atlantic. *Earth Planets Space*, 54:1219–1236.

Morgan, W. (1981). Hotspot tracks and the opening of the atlantic and pacific oceans. *In: Emiliani, C. (Ed.), The Sea*, 7:443–487.

Morgan, W. (1983). Hotspot tracks and the early rifting of the Atlantic. *Tectonophysics*, 94:123–139.

Mosar, J., Lewis, G., and Torsvik, T. (2002). North Atlantic sea-floor spreading rates: implications for the Tertiary development of inversion structures of the Norwegian–Greenland Sea. *Journal of the Geological Society*, 159(5):503–515.

Myhre, A. M. and Eldholm, O. (1981). Sedimentary and crustal velocities in the Norwegian-Greenland Sea. *Journal of geophysical research*, 86:5012–5022.

National Oceanographic Data Center (2013). World Ocean Atlas 2013 [WWW]. Available from: http://www.nodc.noaa.gov/OC5/woa13/ [Accessed 20/01/14].

Olesen, O., Ebbing, J., Gellein, J., Kihle, O., Myklebust, R., Sand, M., Skilbrei, J., Solheim, D., and Usov, S. (2010). Gravity anomaly map, Norway and adjacent areas. Målestokk / Scale 1:3 million. *Trondheim: Geological Survey of Norway*.

Pedersen, S., Larsen, O., Hald, N., Campsie, J., and Bailey, J. (1976). Strontium isotope and lithophile element values from the submarine Jan Mayen province. *Geological Society of Denmark Bull*, 25:15–20.

Peron-Pinvidic, G., Gernigon, L., Gaina, C., and Ball, P. (2012). Insights from the Jan Mayen system in the Norwegian-Greenland seauI. Mapping of a microcontinent. *Geophysical Journal International*, 191(2):385–412.

Pilidou, S., Priestley, K., Debayle, E., and Ólafur Gudmundsson (2005). Rayleigh wave tomography in the North Atlantic: high resolution images of the Iceland, Azores and Eifel mantle plumes. *Lithos*, 79:453 – 474.

Samson, C., Barton, P. J., and Karwatowski, J. (1995). Imaging beneath an basaltic layer using densely sampled wide-angle OBS data. *Geophysical Prospecting*, 43:509–528.

Schilling, J.-G., Kingsley, R., Fontignie, D., Poredda, R., and Xue, S. (1999). Dispersion of the Jan Mayen and Iceland mantle plumes in the Arctic: A He–Pb–Nd–Sr isotope tracer study of basalts from the Kolbeinsey, Mohns, and Knipovich Ridges. *Journal of Geophysics*, 104:10543–10569.

Schilling, J.-G., Zajac, M., Evans, R., Johnston, T., White, W., Devine, J., and Kingsley, R. (1983). Petrologic and geochemical variations along the Mid-Atlantic Ridge from 29^0N to 73^0N. *American Journal of Science*, 283:510–586.

Stein, S. and Wysession, M. (2003). *An introduction to seismology, earthquakes, and earth structure*. Oxford: Blackwell Publishing.

Stockwell Jr., J. W. and Cohen, J. K. (2007). The New SU User's Manual Version 3.3 [WWW] Colorado School Of Mines. Available from: http://www.cwp.mines.edu/sututor/sututor.html [Accessed 10/01/14].

Sørnes, A. and Navrestad, T. (1976). Seismic survey about Jan Mayen. *Norwegian Polar Institute, Yearbook of 1975*, 94:37–52.

Talwani, M. and Eldholm, O. (1977). Evolution of the Norwegian-Greenland Sea. *Geological Society of America*, 88:969–999.

Tessensoh, F. and Piepjohn, K. (2000). Eocene Compressive Deformation in Arctic Canada, North Greenland and Svalbard and Its Plate Teetonic Causes. *Polar Forschung*, 68:121–124.

Trevorrow, M. V., Yamamoto, T., Turget, A., Goodman, D., and Badiey, M. (1989). Very low frequency ocean bottom ambient seismic noise and coupling on the shallow continental shelf. *Marine Geophysics*, 11:129–152.

Trønnes, R. G., Planke, S., Sundvoll, B., and Imsland, P. (1999). Recent volcanic rocks from Jan Mayen: Low-degree melt fractions of enriched northeast Atlantic mantle. *Journal of Geophysical Research: Solid Earth*, 104(B4):7153–7168.

Verhoef, J., Roest, W., Macnab, R., Arkani-Hamed, J., and of the Project Team", M. (1996). Magnetic anomalies of the Arctic and North Atlantic Oceans and adjacent land areas, GSC Open file 3125, 225 pp., 300 figures. *Ottawa: Geological Survey of Canada*.

Vink, G. (1984). A hotspot model for Iceland and the Vøring Plateau. *Journal of Geophysical Research*, 89:9949–9959.

Virieux, J. (1996). *Seismic ray tracing. In: Boschi, E. et al, (eds.) Seismic Modeling of Earth Structure*. Bologna: Editrice Compositori, pp. 223-304.

Voss, M. and Jokat, W. (2007). Continent–ocean transition and voluminous magmatic underplating derived from P-wave velocity modelling of the East Greenland continental margin. *Geophysical Journal International*, 170(2):580–604.

Voss, M., Schmidt-Aursch, M., and Jokat, W. (2009). Variations in magmatic processes along the East Greenland volcanic margin. *Geophysical Journal International*, 177:755–782.

Webb, S. C. and Cox, C. S. (1986). Observations and modeling of seafloor microseisms. *Journal Geophysics*, 91:7343–7358.

White, R. and McKenzie, D. (1989). Magmatism at rift zones: The generation of volcanic continental margins and flood basalts. *Journal of Geophysical Research*, 94:7685–7729.

White, R. S. (1992). Crustal structure and magmatism of the North Atlantic continental margin. *Journal of the Geological Society of London*, 149:841–854.

Yilmaz, O. (1987). *Seismic Data Analysis*. Tulsa, Oklahoma: Society of Exploration Geophysics.

Zelt, C. A. (1999). Modelling strategies and model assessment for wide-angle seismic traveltime data. *Geophysical Journal International*, 139:183–204.

Zelt, C. A. and Ellis, R. M. (1988). Practical and efficient ray tracing in two-dimensional media for rapid traveltime and amplitude forward modelling. *Canadian Journal of Exploration Geophysics*, 24:16–31.

Zelt, C. A. and Smith, R. B. (1992). Seismic traveltime inversion for 2-d crustal velocity structure. *Geophysical Journal International*, 108:16–32.

Zoeppritz, K. (1919). On the reflection and propagation of seismic waves. *Gottinger Nachrichten*, 1:66–84.

Appendix A

Processing in Seismic Unix: Shell Script Examples

A.1 Locating missing traces and editing header

```
#! /bin/sh
# # # # # # # # # # # # # # # # # # # # # # # # # # # # # # # # # # # # # # # # # # # # # #
# Fill in trace gaps in OBS gather (S.E. 26.03.2014)
# # # # # # # # # # # # # # # # # # # # # # # # # # # # # # # # # # # # # # # # # # # # # #
# Input OBS data as argument

input=$1

# # # Find which fldr that are missing
sugethw < $input key=fldr output=geom > fldr.tmp
octave < find_nofldr.m > screendump.tmp
cat nofldr_octave.tmp | awk ' { if($1!="#") print $1 } ' > nofldr.tmp

# # # Read file containing missing traces and assign values to shell vector
while read line
do
x+=("$line")
done < nofldr.tmp

# # # Create null-traces
for ((i=1;i<${#x[@]};i++))
do
sunull nt=15360 dt=3906 ntr=1 | \
sushw key=fldr a=${x[$i]} ≫ nulls.tmp
done
```

```
# # # Combine null-traces and OBS data
cat $input nulls.tmp | susort fldr > $input.corrected.su

rm *.tmp

# # # End of script # # #

% % % % % % % % % % % % % % % % % % % % % % % % % % % % % % %
% find_nofldr.m (Octave script)
% % % % % % % % % % % % % % % % % % % % % % % % % % % % % % %

x=12:1:1517;
load fldr.tmp;
fldr=fldr(:,1);
nofldr(1)=zeros(length(x)-length(fldr),1);
m=1;
n=1;
for i=1:length(x)
if fldr(m)!=x(i)
nofldr(n,1)=x(i);
n=n+1;
else
m=m+1;
end
end
save nofldr_octave.tmp nofldr

% % % End of script % % %
```

A.2 Polarization analysis

```
#! /bin/sh
# # # # # # # # # # # # # # # # # # # # # # # # # # # # # # # # # # # # # # # # # # # # # # # # #
# Shell script example: Polarization analysis with Seismic Unix (S.E. 10.03.2014)
# # # # # # # # # # # # # # # # # # # # # # # # # # # # # # # # # # # # # # # # # # # # # # # # #
# Read 3-component OBS recording from separate SU-files:
# input.C1.su, input.C2.su and input.C3.su.

# # # Combine and sort 3 component data
sushw < input.C1.su key=trid,tracf a=12,1 b=0,1 > data3C.tmp
sushw < input.C2.su key=trid,tracf a=13,1 b=0,1 ≫ data3C.tmp
sushw < input.C3.su key=trid,tracf a=14,1 b=0,1 ≫ data3C.tmp
susort < data3C.tmp > data3C.sort.tmp tracf trid
```

```
# # # Pick out a small correlation window around the water pulse:
suxwigb < input.C1.su mpicks=pick.dat perc=90
x= ‘ awk ’ { print $2 } ’ < pick.dat ‘
tmn= ‘ awk ’ { print $1 - 0.1 } ’< pick.dat ‘
tmx= ‘ awk ’ { print $1 + 0.15 } ’ < pick.dat ‘
for ((i=0;i< ${#x[*]};i++ ))
do
suwind < data3C.sort.tmp key=fldr min=${x[i]} max=${x[i]} \
tmin=${tmn[i]} tmax=${tmx[i]} ≫ data3C.win.tmp
done

# # # Polarization analysis
supolar < data3C.win.tmp wl=0.25 phi=3 angle=deg r1=2 rlq=1

# # # Write to file
n=‘surange<data3C.sort.tmp key=ns | awk ’NR==2 { print ($2-1)/2 }’‘
suwind < polar.phi itmin=$n itmax=$n | suascii | awk ’ NR%5==4 { print $2 } ’ > phi.txt
suwind < polar.rl itmin=$n itmax=$n | suascii | awk ’ NR%5==4 { print $2 } ’ > rl.txt

rm *.tmp polar.*

# # # End of script # # #
```

Appendix B

Rayinvr Modeling Results

B.1 P-wave modeling

B.1.1 Model 1

Forward modeling results:

Number of data points used: 2922
RMS traveltime residual: 0.083
Normalized chi-squared: 1.206

phase	npts	Trms	chi-squared
P_g	304	0.098	1.715
P_c	1321	0.074	1.322
PmP	288	0.051	0.534
P_n	1009	0.096	1.097

shot	dir	npts	Trms	chi-squared
260.871	-1	511	0.058	0.922
260.871	1	164	0.035	0.482
220.742	-1	328	0.120	1.608
220.742	1	335	0.042	0.706
180.568	-1	448	0.066	1.156
180.568	1	364	0.072	2.089
140.503	-1	454	0.120	1.444
140.503	1	318	0.090	0.896

Results after inversion:

Number of data points used: 2931
RMS traveltime residual: 0.058
Normalized chi-squared: 0.630

phase	npts	Trms	chi-squared
P_g	304	0.051	0.609
P_c	1324	0.059	0.809
PmP	288	0.047	0.502
P_n	1015	0.061	0.442

shot	dir	npts	Trms	chi-squared
260.871	-1	511	0.051	0.710
260.871	1	165	0.022	0.200
220.742	-1	323	0.087	0.881
220.742	1	336	0.031	0.391
180.568	-1	448	0.056	0.822
180.568	1	371	0.046	0.866
140.503	-1	459	0.071	0.509
140.503	1	318	0.058	0.367

Model parameters:

Number of layers = 5
Number of blocks = 817
Xmin = 0.00 Xmax = 301.00
Zmin = 0.00 Zmax = 20.00
Vmin = 1.48 Vmax = 8.50

Layer	#B	#V1	#V2	Zave	V1ave	V2ave
0	2	2	2	0.00	1.48	1.48
I	187	31	31	1.75	1.80	2.25
II	253	17	17	2.40	3.61	5.53
III	18	11	11	4.96	6.72	7.16
IV	12	7	7	9.73	7.83	8.42
Base	2			20.00		

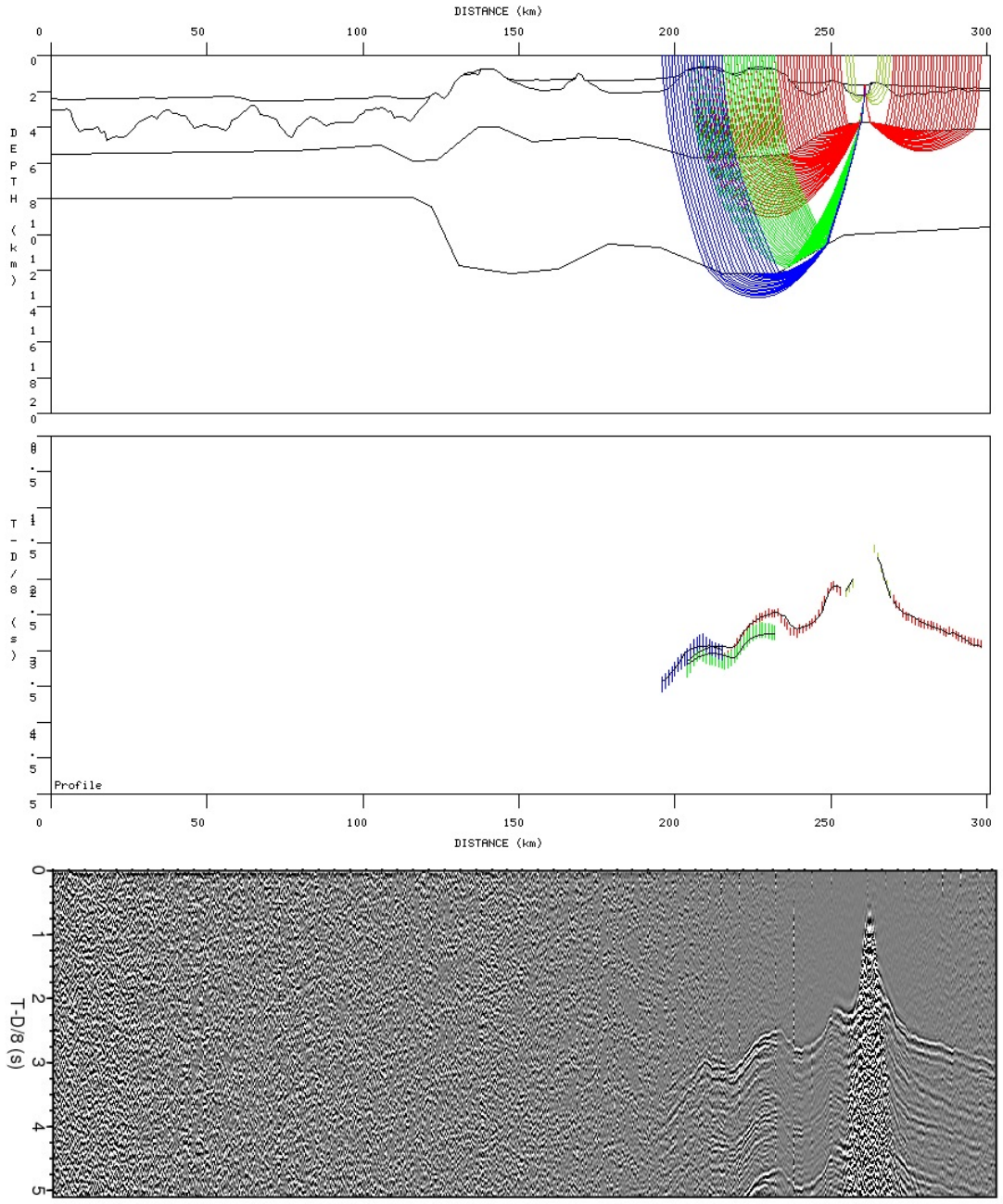

Figure B.1: Model 1: Picked P-wave phases and traced rays of OBS 1.

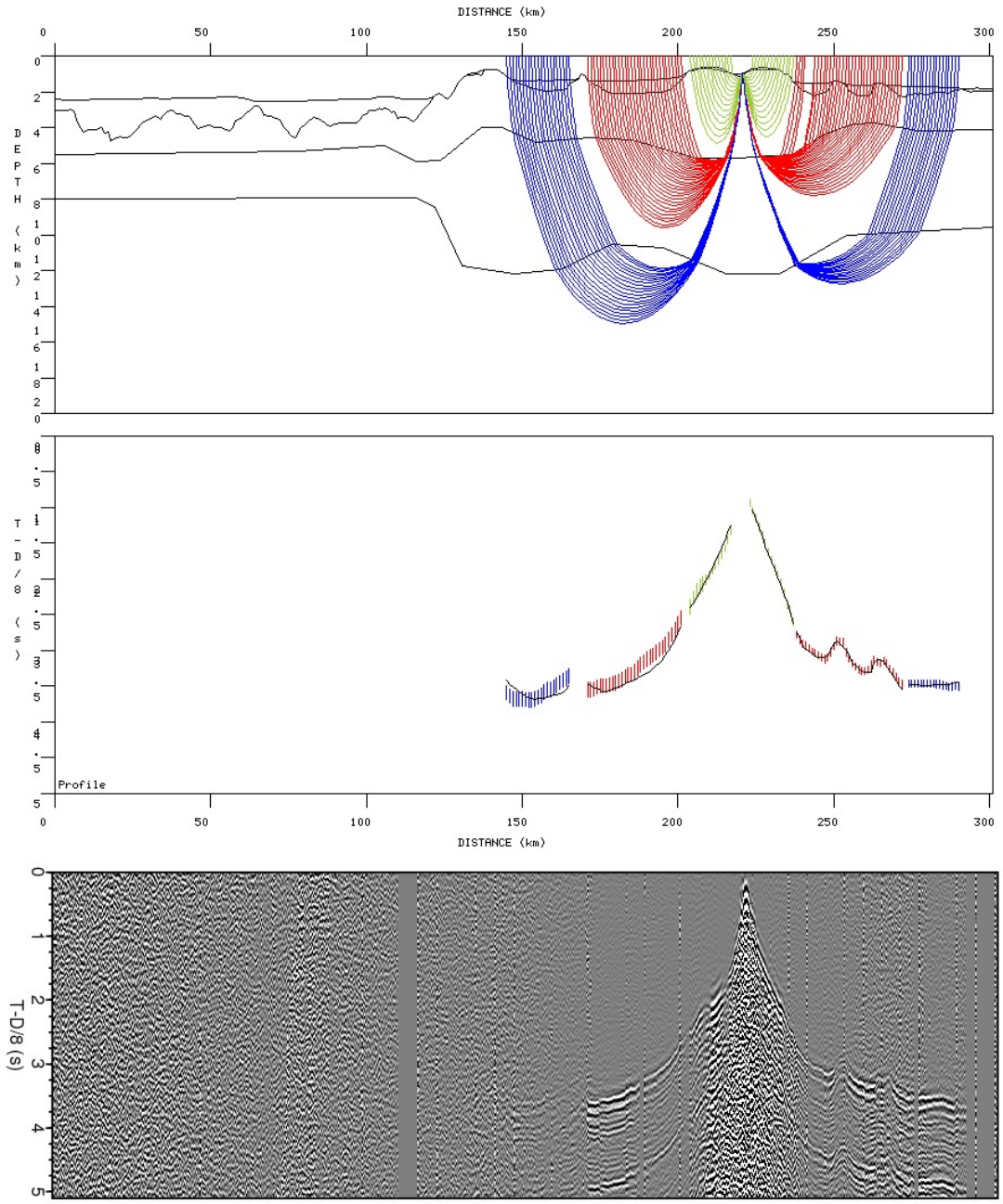

Figure B.2: Model 1: Picked P-wave phases and traced rays of OBS 2

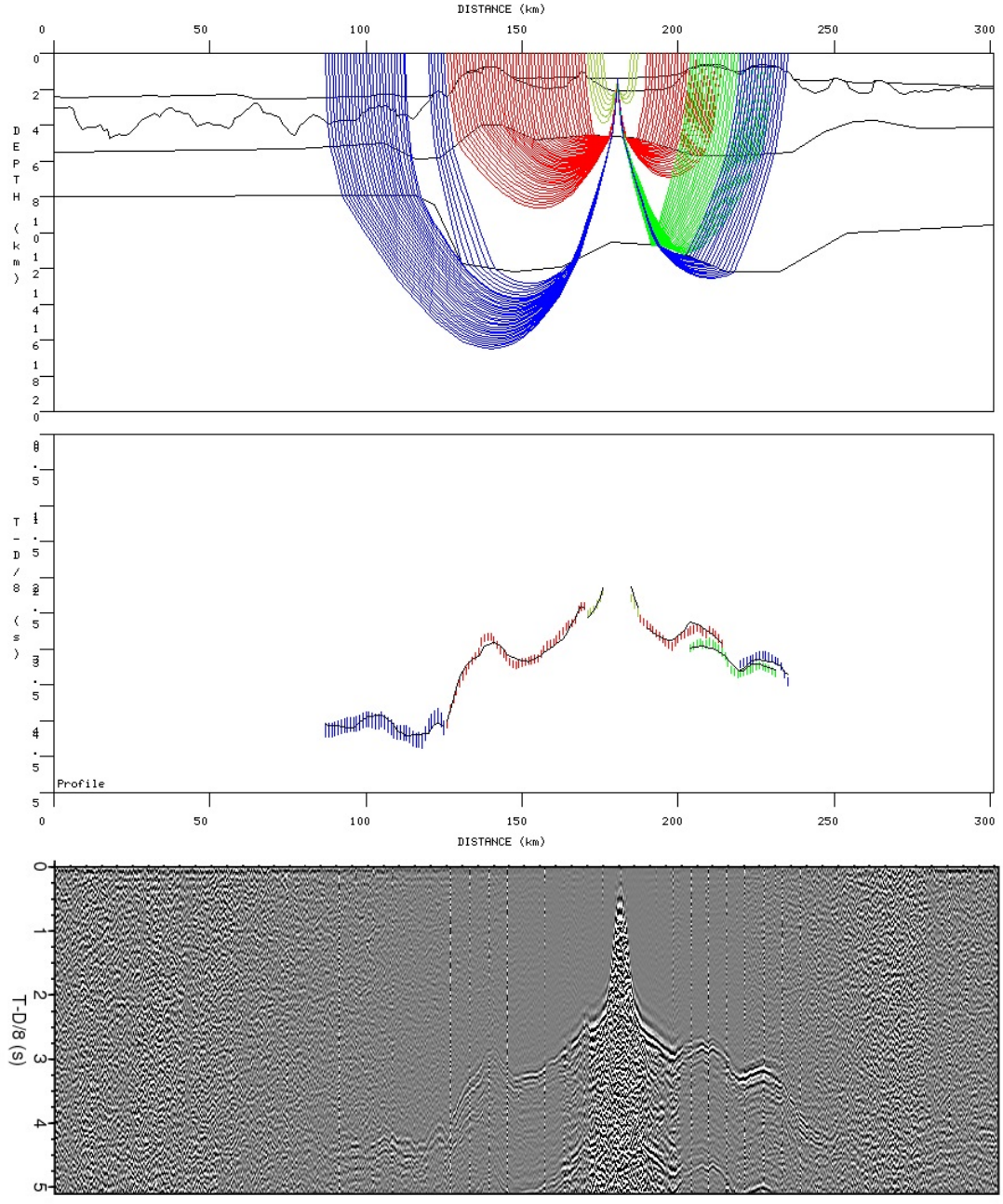

Figure B.3: Model 1: Picked P-wave phases and traced rays of OBS 3.

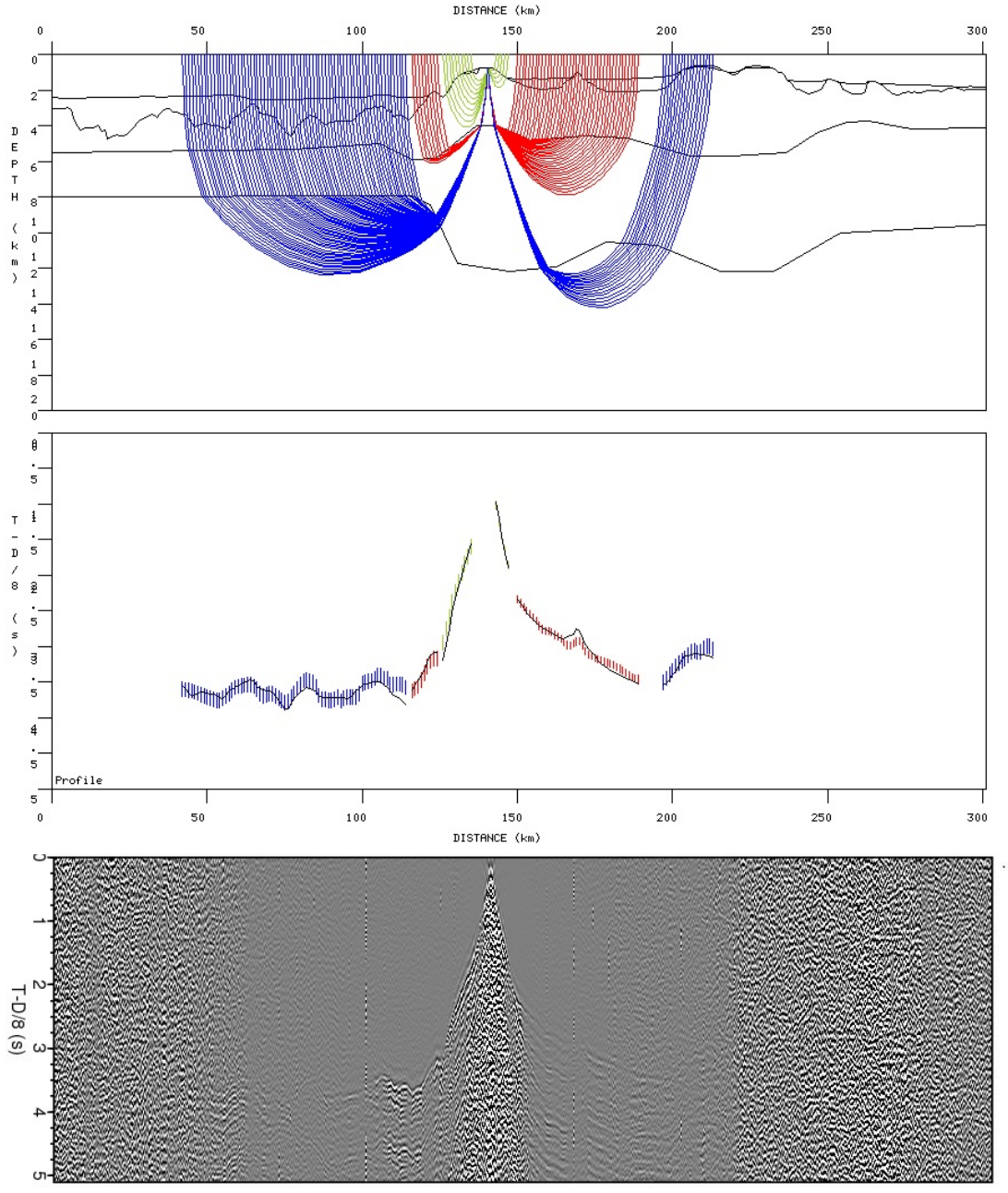

Figure B.4: Model 1: Picked P-wave phases and traced rays of OBS 4.

B.1.2 Model 2

Forward modeling results:

Number of data points used: 3109
RMS traveltime residual: 0.080
Normalized chi-squared: 1.233

phase	npts	Trms	chi-squared
P_g	209	0.060	1.469
P_s	280	0.061	1.483
P_c	1287	0.086	1.755
PmP	327	0.078	0.611
P_n	1006	0.081	0.655

shot	dir	npts	Trms	chi-squared
260.871	-1	511	0.075	0.974
260.871	1	163	0.040	0.641
220.742	-1	349	0.089	1.599
220.742	1	329	0.038	0.554
180.568	-1	442	0.077	1.774
180.568	1	535	0.094	1.074
140.503	-1	462	0.095	1.004
140.503	1	318	0.078	2.130

Results after inversion:

Number of data points used: 3104
RMS traveltime residual: 0.067
Normalized chi-squared: 0.870

phase	npts	Trms	chi-squared
P_g	210	0.049	0.953
P_s	278	0.043	0.759
P_c	1282	0.074	1.320
PmP	327	0.072	0.518
P_n	1007	0.065	0.426

shot	dir	npts	Trms	chi-squared
260.871	-1	511	0.066	0.722
260.871	1	161	0.040	0.632
220.742	-1	346	0.082	1.070
220.742	1	330	0.035	0.454
180.568	-1	440	0.069	1.456
180.568	1	535	0.079	0.664
140.503	-1	463	0.067	0.490
140.503	1	318	0.064	1.546

Model parameters:

Number of layers = 6
Number of blocks = 781
Xmin = 0.00 Xmax = 301.00
Zmin = 0.00 Zmax = 20.00
Vmin = 1.48 Vmax = 8.50

Layer	#B	#V1	#V2	Zave	V1ave	V2ave
0	2	2	2	0.00	1.48	1.48
I	187	31	31	1.75	1.80	2.25
IIA	235	17	17	2.40	3.44	4.58
IIB	14	9	9	4.01	5.49	6.55
III	12	7	7	5.73	6.78	7.22
IV	11	9	9	9.37	7.79	8.48
Base	2			20.00		

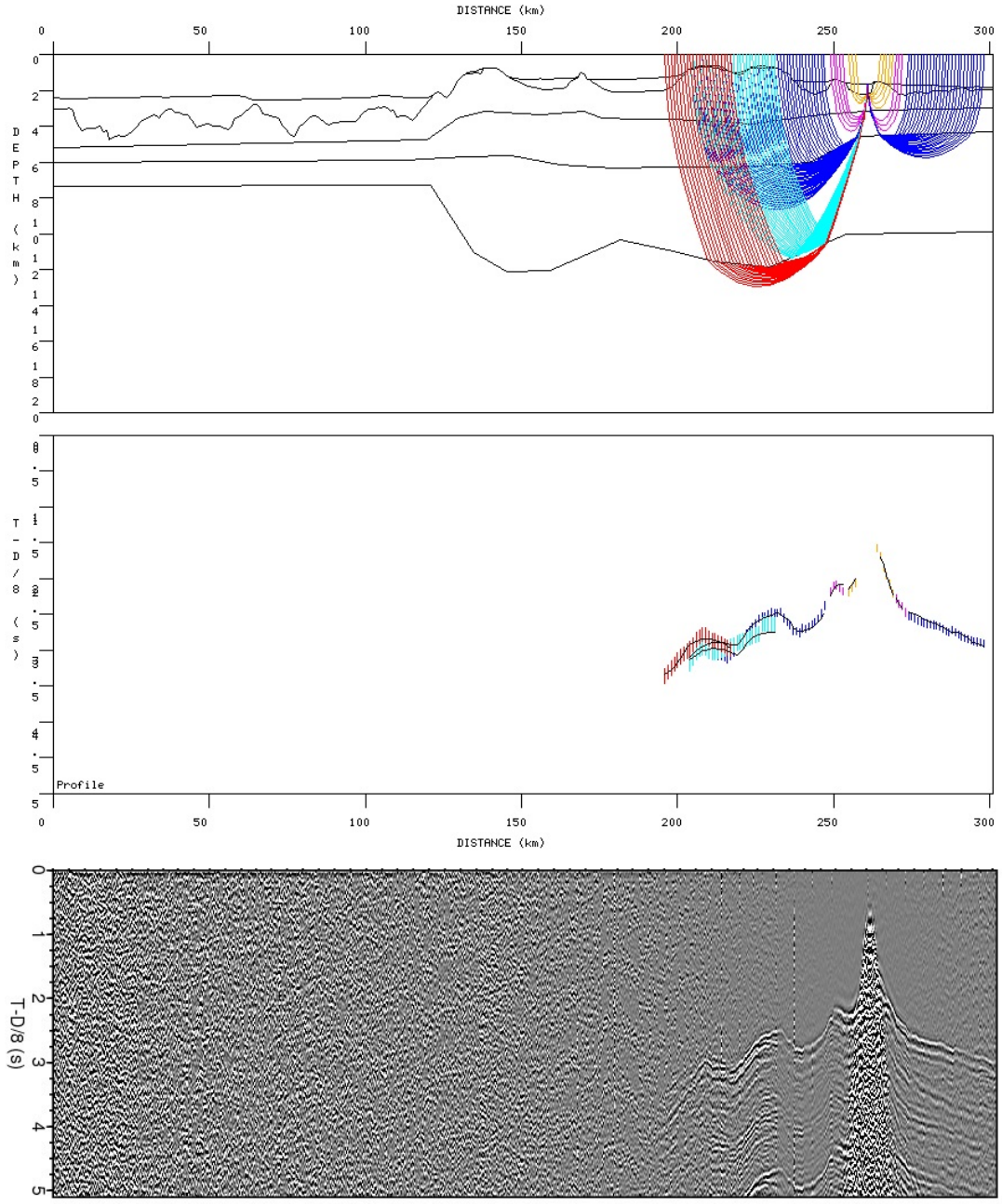

Figure B.5: Model 2: Picked P-wave phases and traced rays of OBS 1.

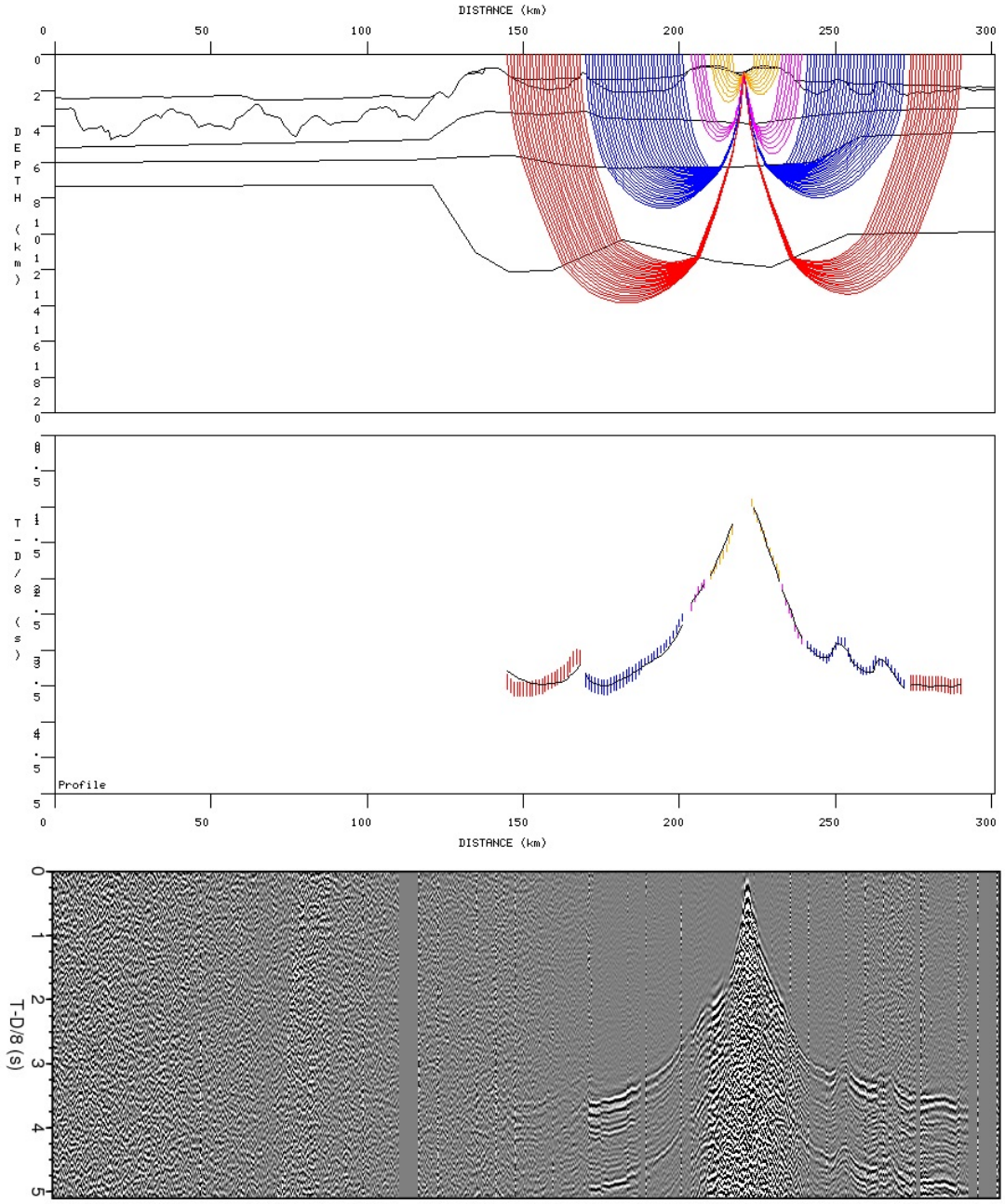

Figure B.6: Model 2: Picked P-wave phases and traced rays of OBS 2

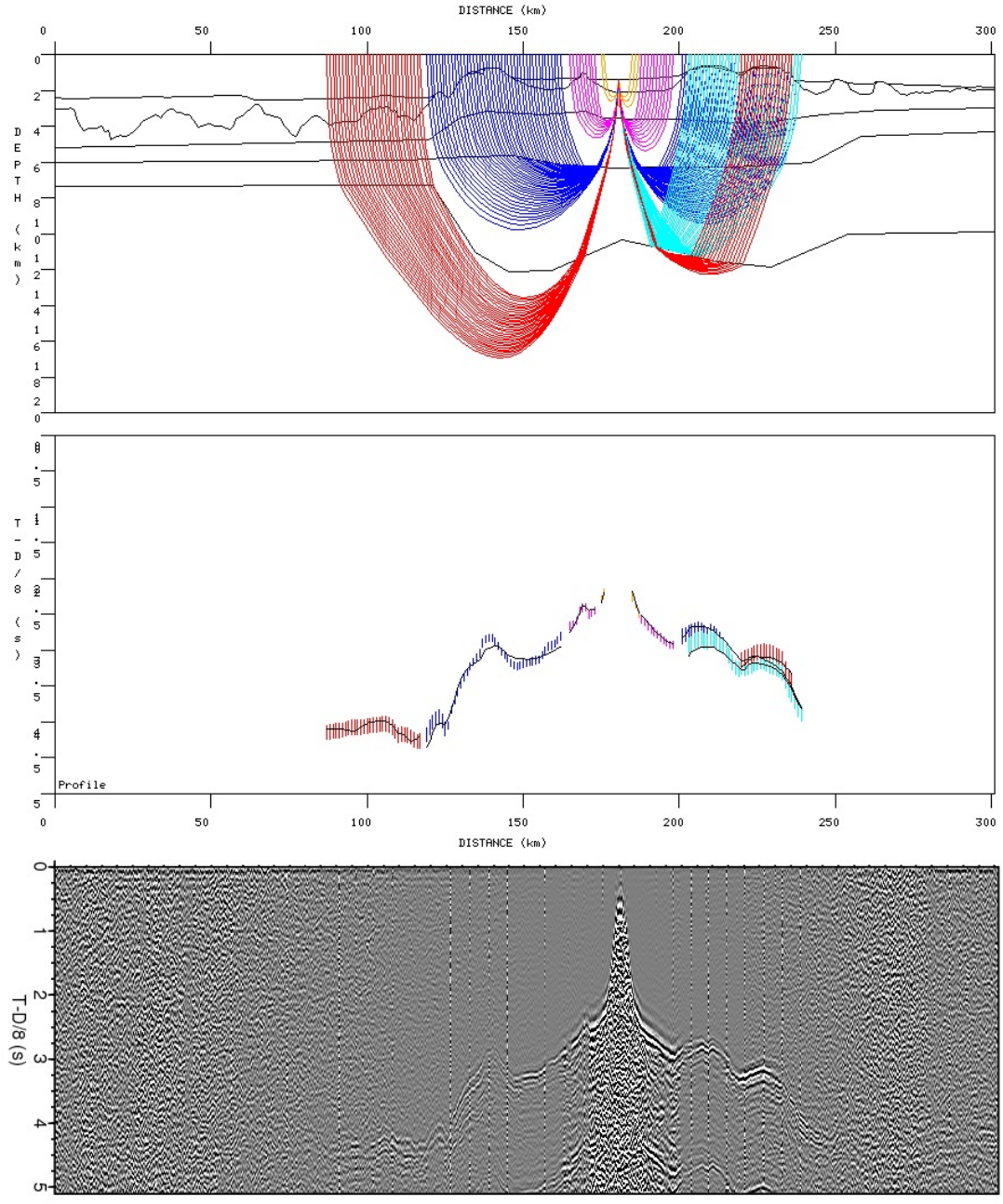

Figure B.7: Model 2: Picked P-wave phases and traced rays of OBS 3.

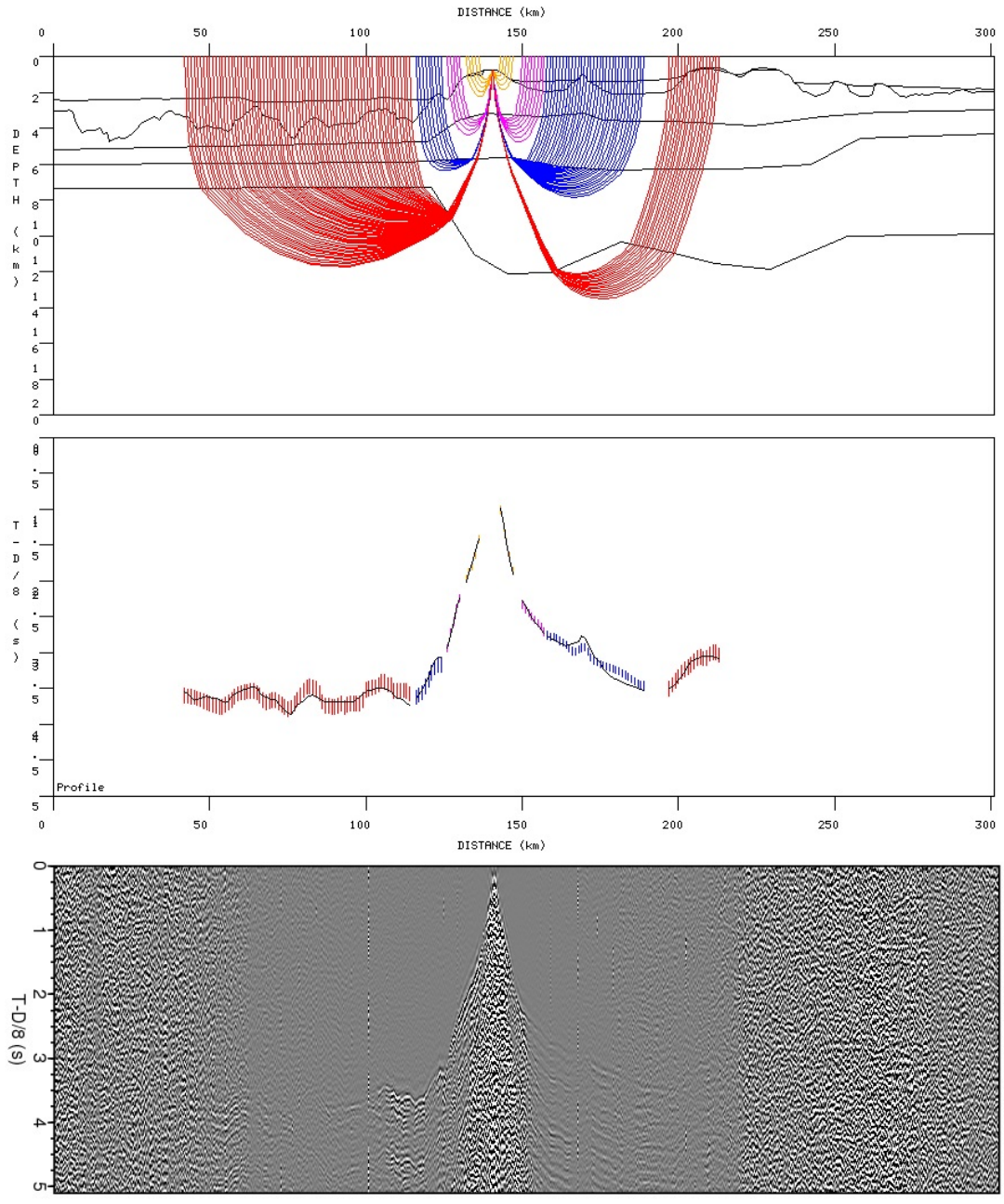

Figure B.8: Model 2: Picked P-wave phases and traced rays of OBS 4.

B.2 S-wave modeling

B.2.1 Model 1

PSS-wave forward modeling

```
Number of data points used:     2159
RMS traveltime residual:       0.221
Normalized chi-squared:        3.007
```

phase	npts	Trms	chi-squared
PSS_g	50	0.109	1.208
PSS_c	786	0.246	6.048
PSS_c*	344	0.098	0.956
PSmS	49	0.400	4.078
PSS_n	729	0.239	1.431
PSS_n*	201	0.152	0.584

shot	dir	npts	Trms	chi-squared
260.871	-1	201	0.112	1.268
260.871	1	192	0.211	1.413
220.742	-1	217	0.329	10.040
220.742	1	256	0.206	3.653
180.568	-1	400	0.148	1.313
180.568	1	345	0.271	4.897
140.503	-1	548	0.218	1.200

PPS-wave forward modeling

```
Number of data points used:     1118
RMS traveltime residual:       0.261
Normalized chi-squared:        9.741
```

phase	npts	Trms	chi-squared
PPS_c	958	0.237	10.787
PPS_n	160	0.373	3.507

shot	dir	npts	Trms	chi-squared
260.871	-1	268	0.185	13.729
260.871	1	170	0.207	17.244
180.568	-1	268	0.369	7.549
180.568	1	193	0.258	6.468
140.503	1	219	0.218	4.789

PSS-wave modeling

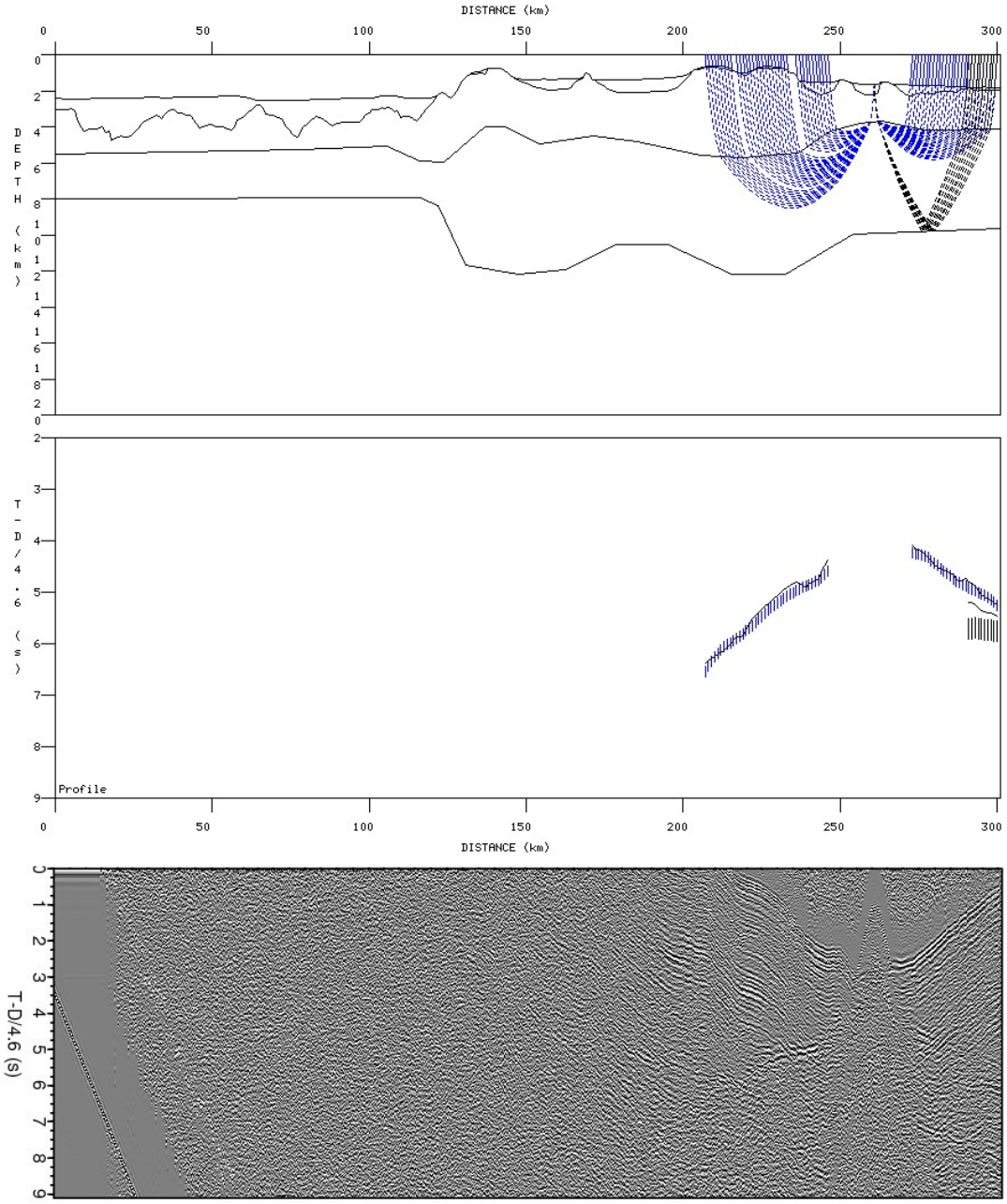

Figure B.9: Model 1: Picked PSS-wave phases and traced rays of OBS 1.

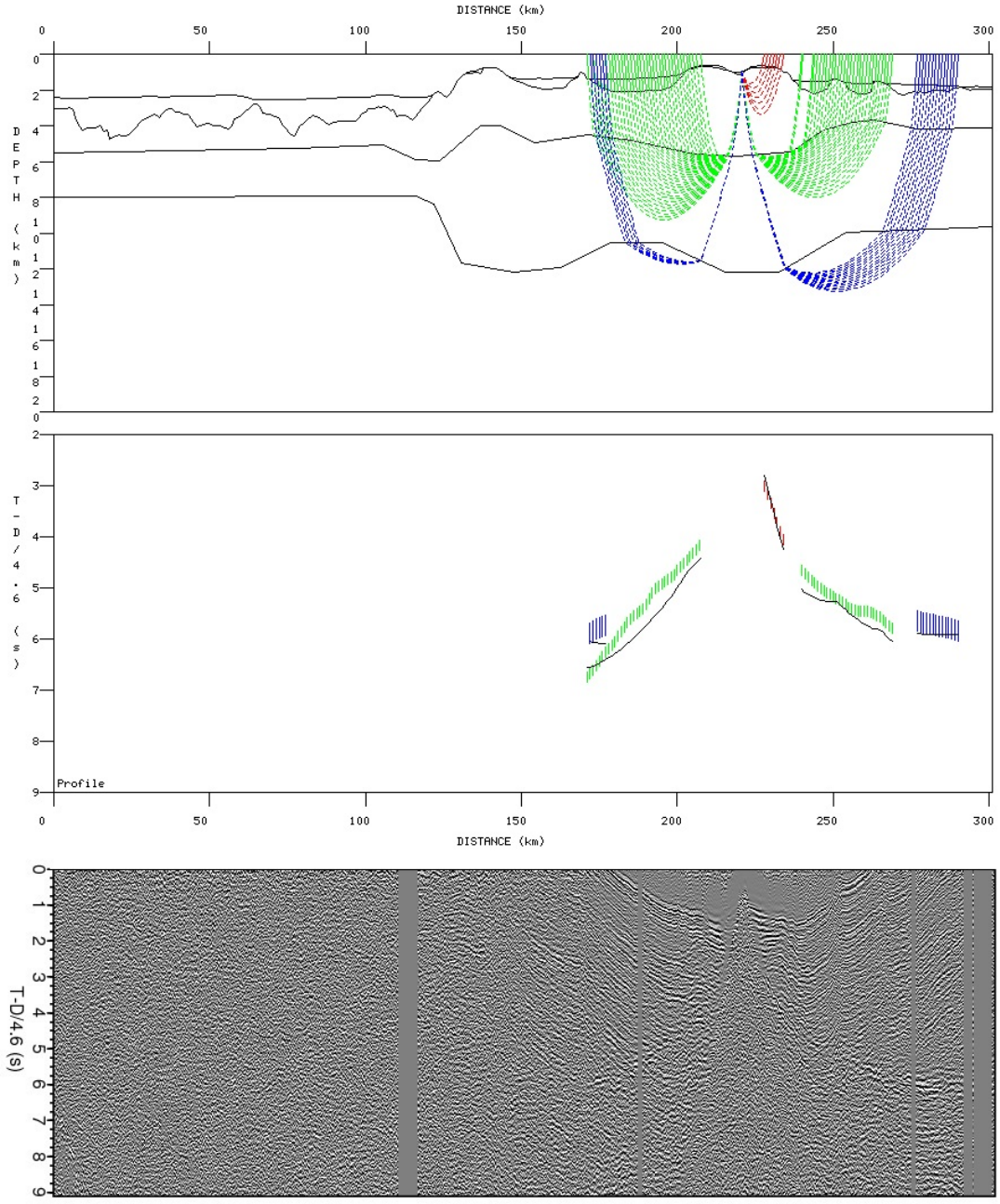

Figure B.10: Model 1: Picked PSS-wave phases and traced rays of OBS 2.

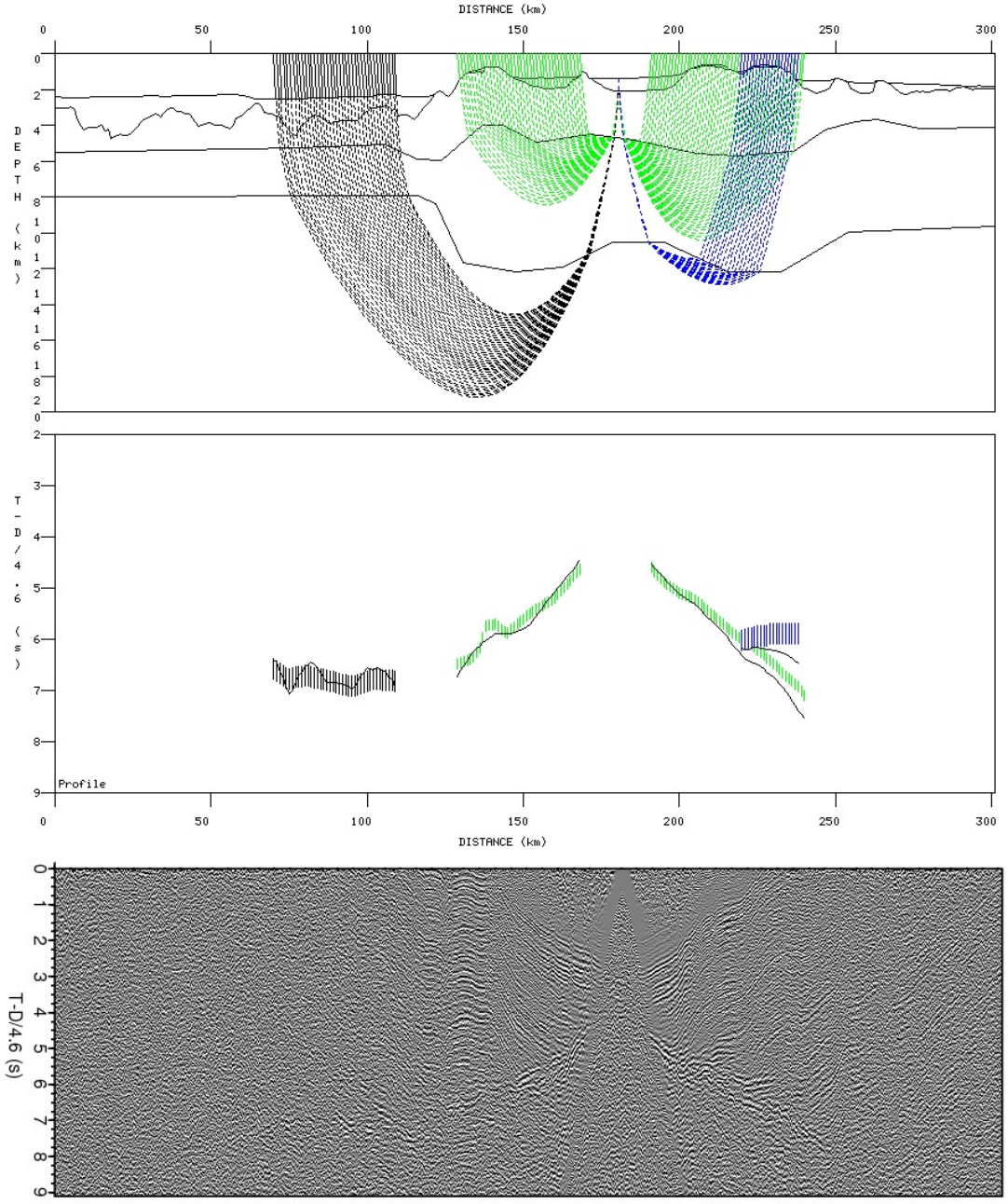

Figure B.11: Model 1: Picked PSS-wave phases and traced rays of OBS 3.

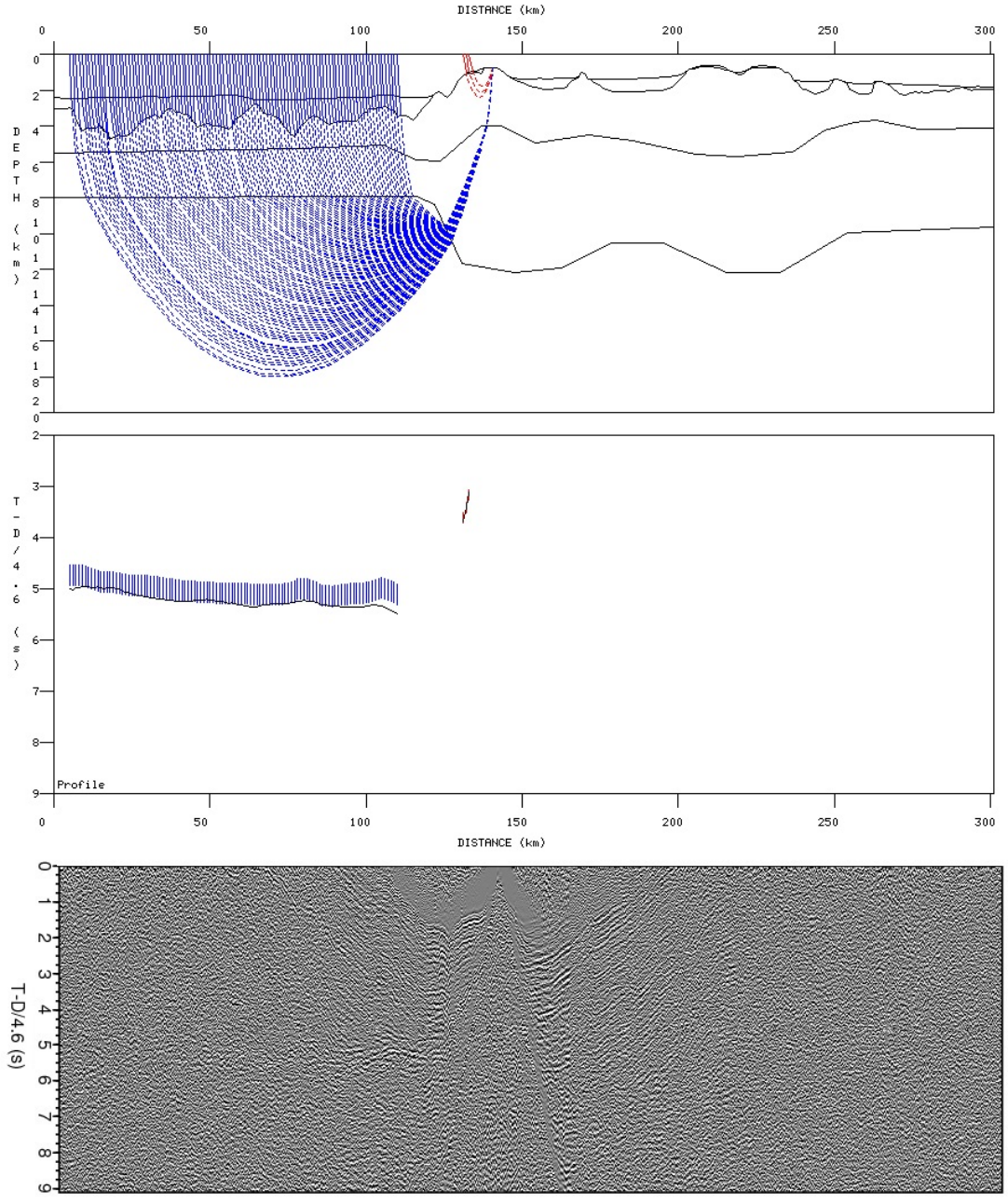

Figure B.12: Model 1: Picked PSS-wave phases and traced rays of OBS 4.

PPS-wave modeling

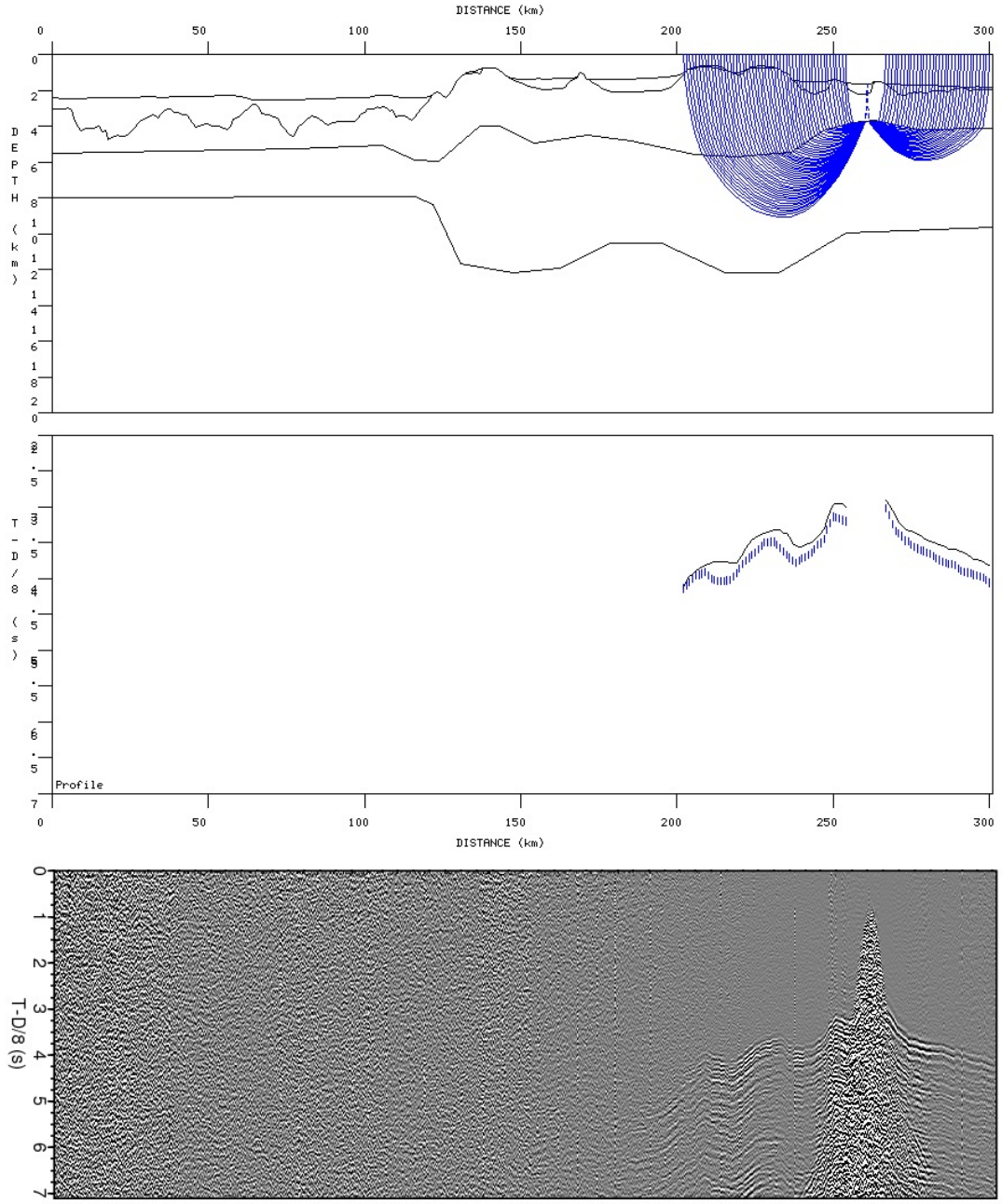

Figure B.13: Model 1: Picked PPS-wave phases and traced rays of OBS 1.

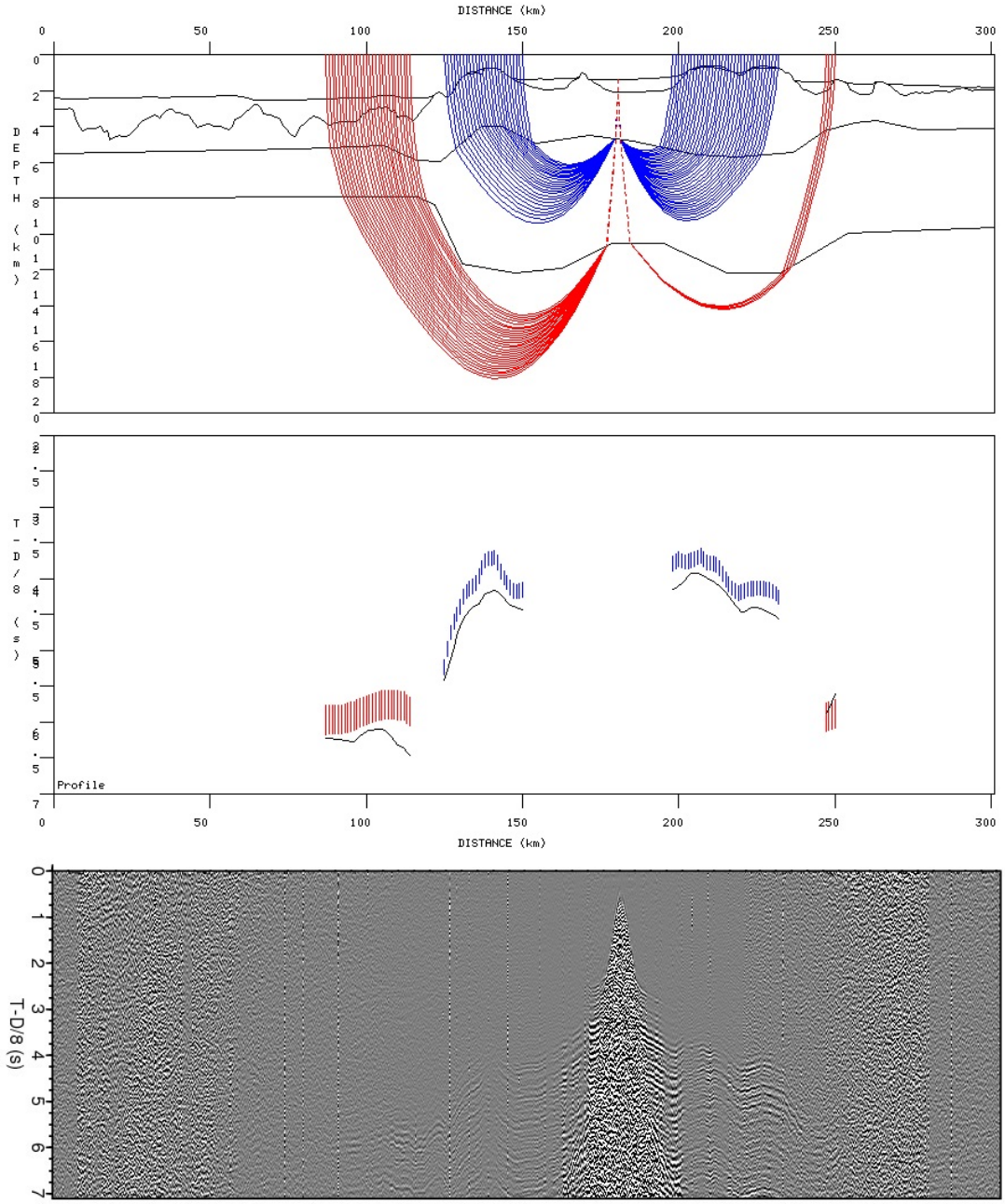

Figure B.14: Model 1: Picked PPS-wave phases and traced rays of OBS 3.

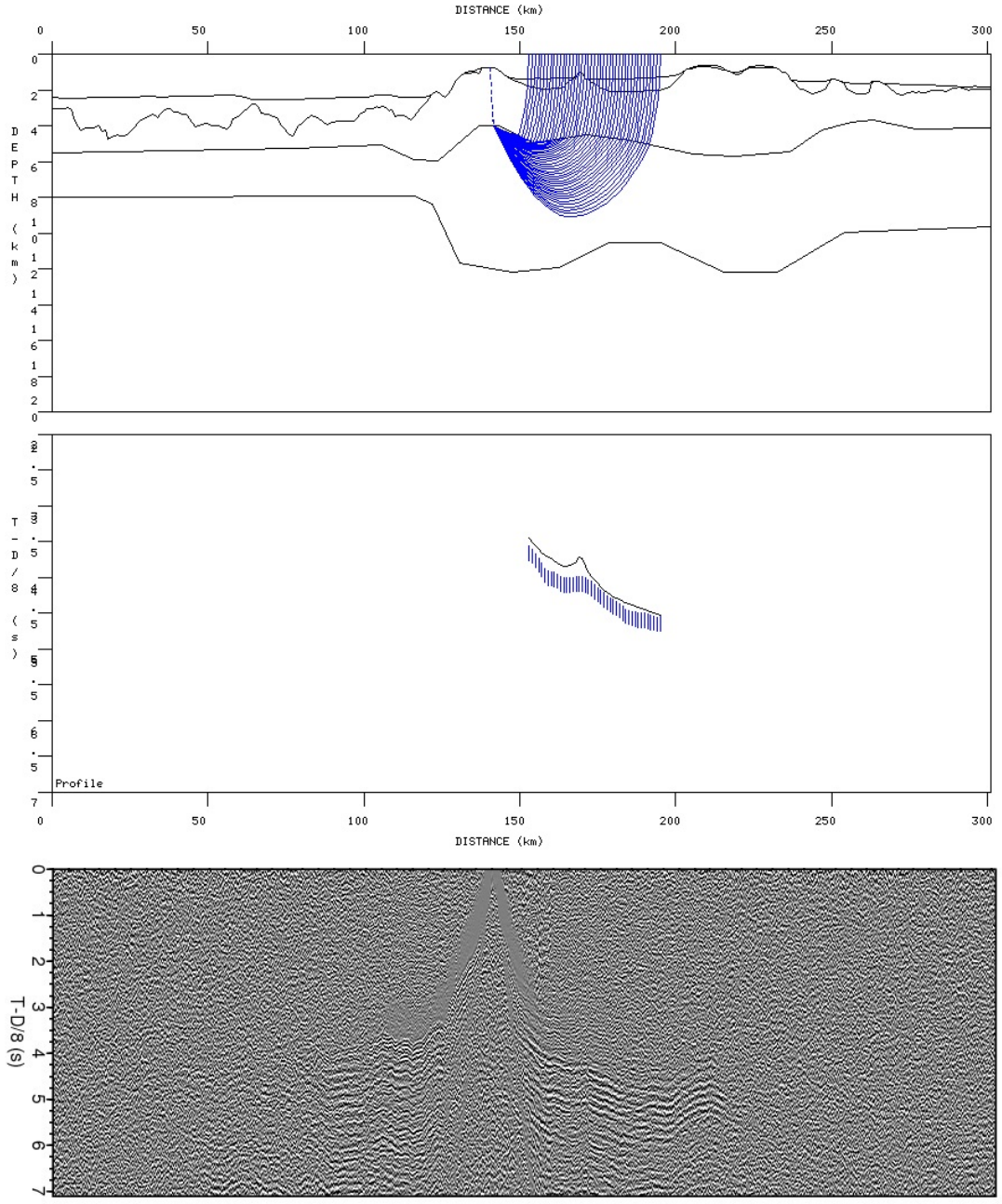

Figure B.15: Model 1: Picked PPS-wave phases and traced rays of OBS 4.

B.2.2 Model 2

PSS-wave forward modeling

```
Number of data points used:     2159
RMS traveltime residual:       0.258
Normalized chi-squared:        4.020
```

phase	npts	Trms	chi-squared
PSS_q	39	0.173	3.068
PSS_s	57	0.202	4.156
PSS_c	1084	0.244	5.942
PSmS	49	0.267	1.822
PSS_n	729	0.283	2.003
PSS_n*	201	0.262	1.720

shot	dir	npts	Trms	chi-squared
260.871	-1	201	0.134	1.806
260.871	1	192	0.214	3.229
220.742	-1	215	0.343	10.742
220.742	1	266	0.353	11.743
180.568	-1	385	0.206	1.559
180.568	1	354	0.206	1.765
140.503	-1	546	0.275	1.953

PPS-wave forward modeling

```
Number of data points used:     1386
RMS traveltime residual:       0.170
Normalized chi-squared:        2.317
```

phase	npts	Trms	chi-squared
PPS_s	112	0.114	1.301
PPS_c	630	0.097	2.719
PPS_c*	383	0.134	1.812
PPS_n	160	0.398	3.985
PPS_n*	101	0.054	0.295

shot	dir	npts	Trms	chi-squared
260.871	-1	243	0.091	3.333
260.871	1	169	0.100	4.044
180.568	-1	375	0.268	2.303
180.568	1	280	0.156	2.181
140.503	1	319	0.089	0.797

PSS-wave modeling

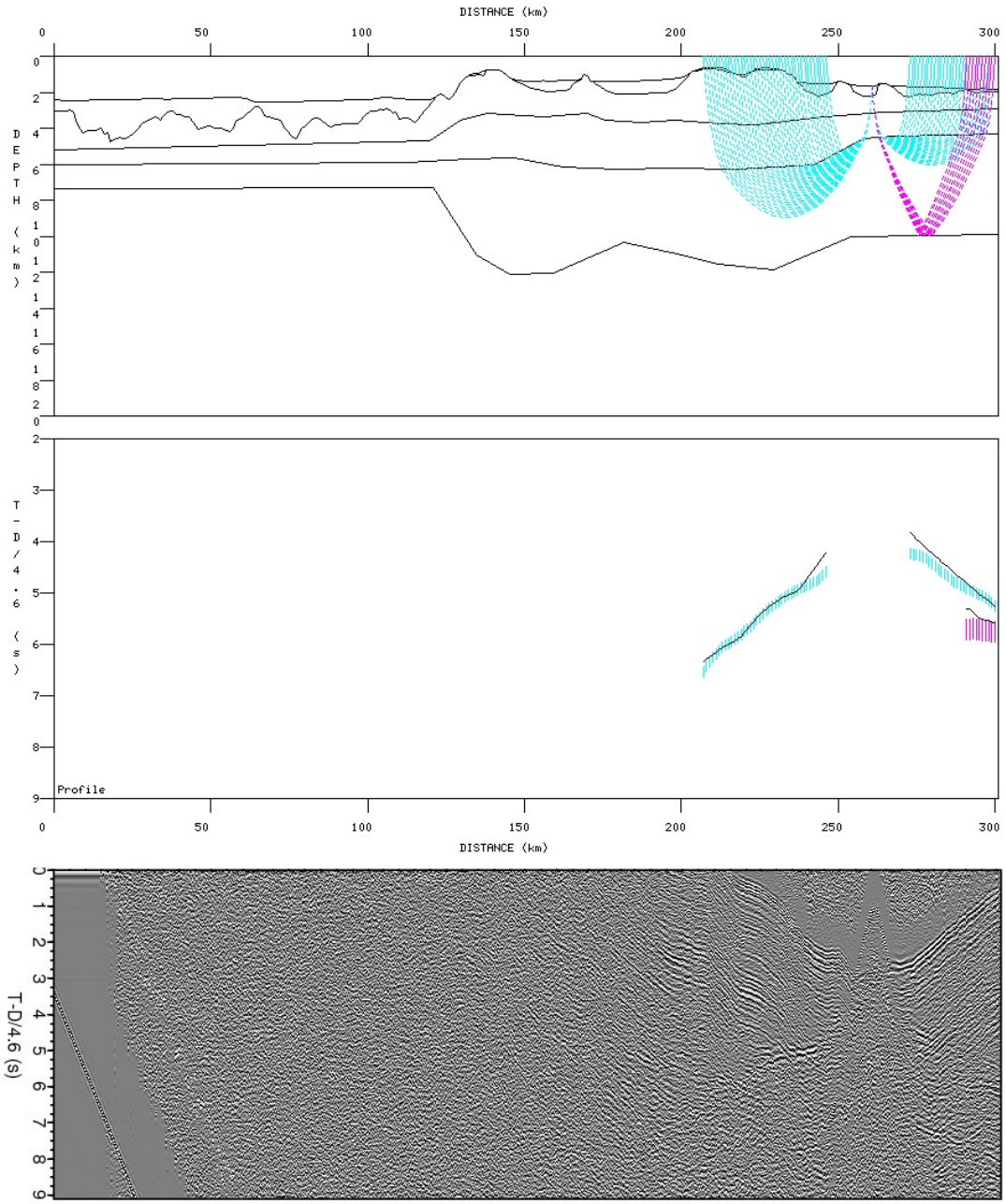

Figure B.16: Model 2: Picked PSS-wave phases and traced rays of OBS 1.

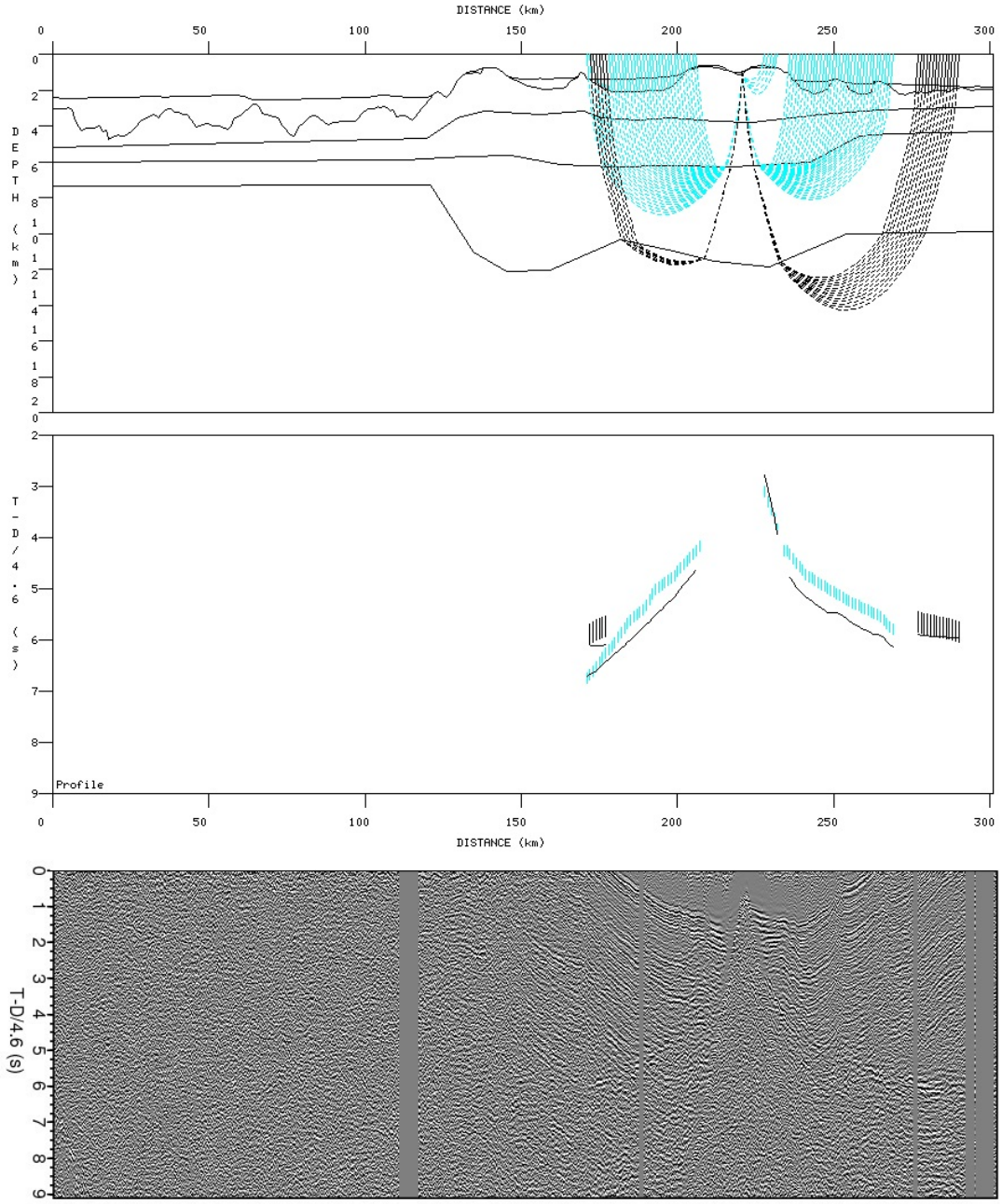

Figure B.17: Model 2: Picked PSS-wave phases and traced rays of OBS 2.

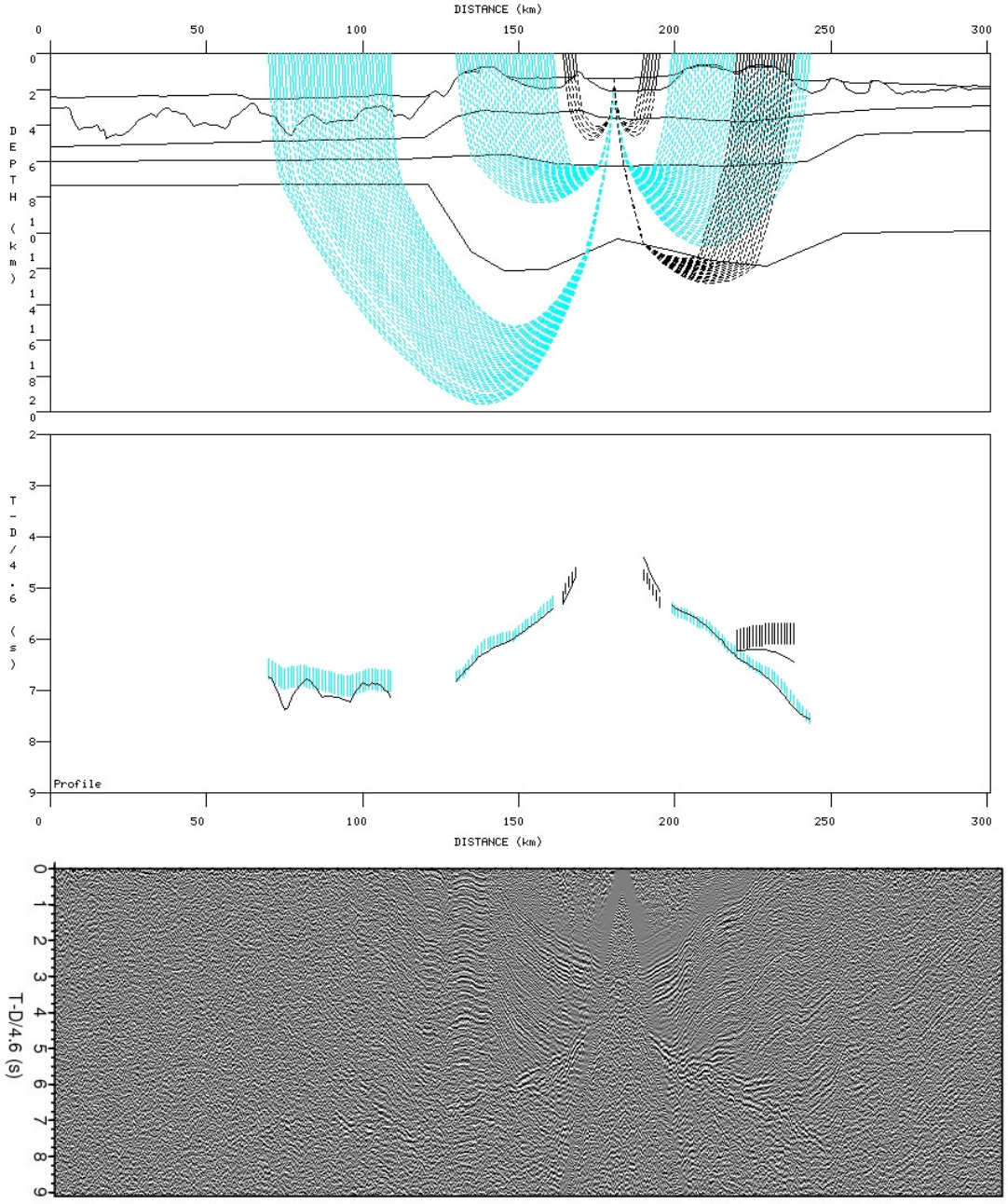

Figure B.18: Model 2: Picked PSS-wave phases and traced rays of OBS 3.

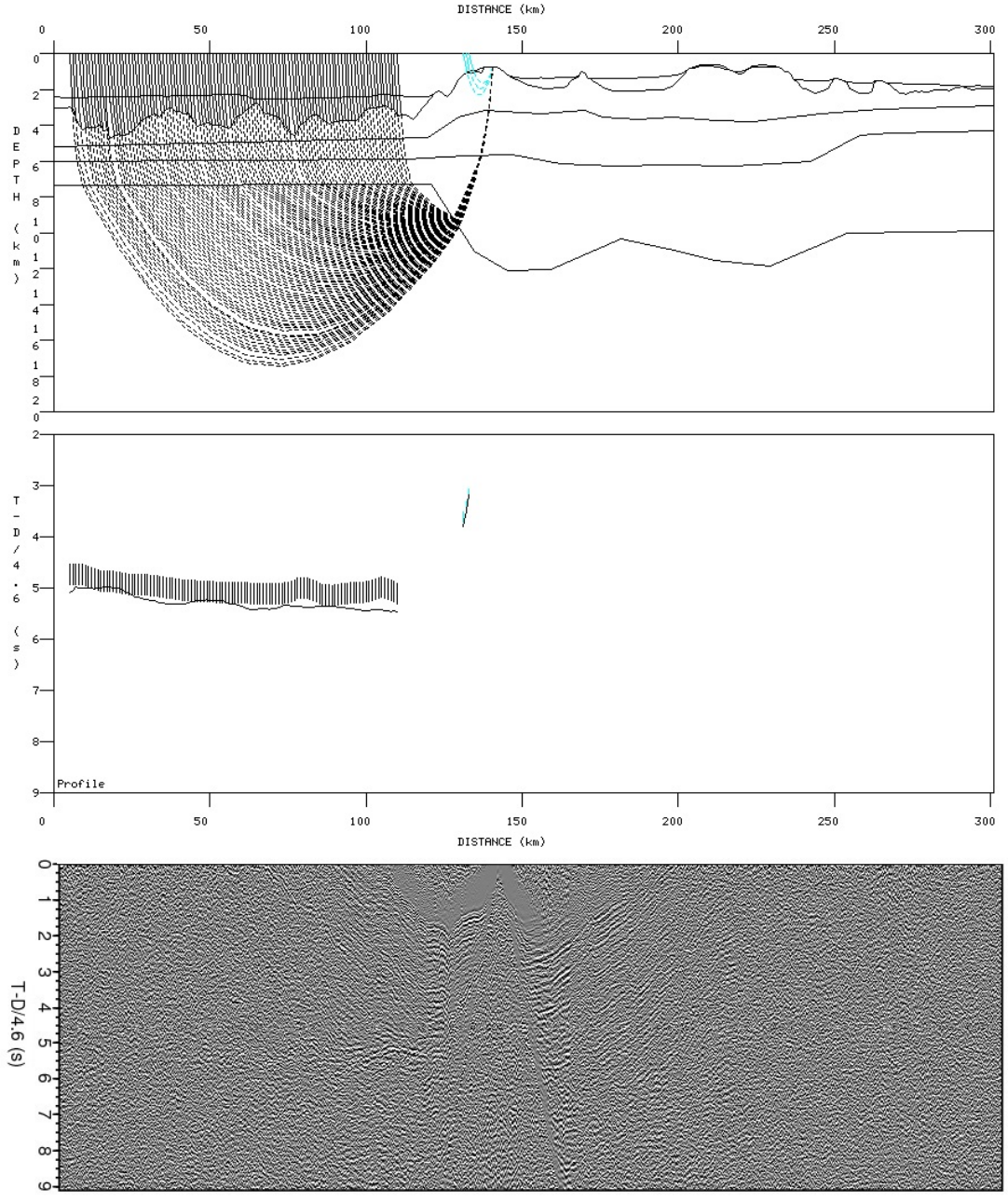

Figure B.19: Model 2: Picked PSS-wave phases and traced rays of OBS 4.

PPS-wave modeling

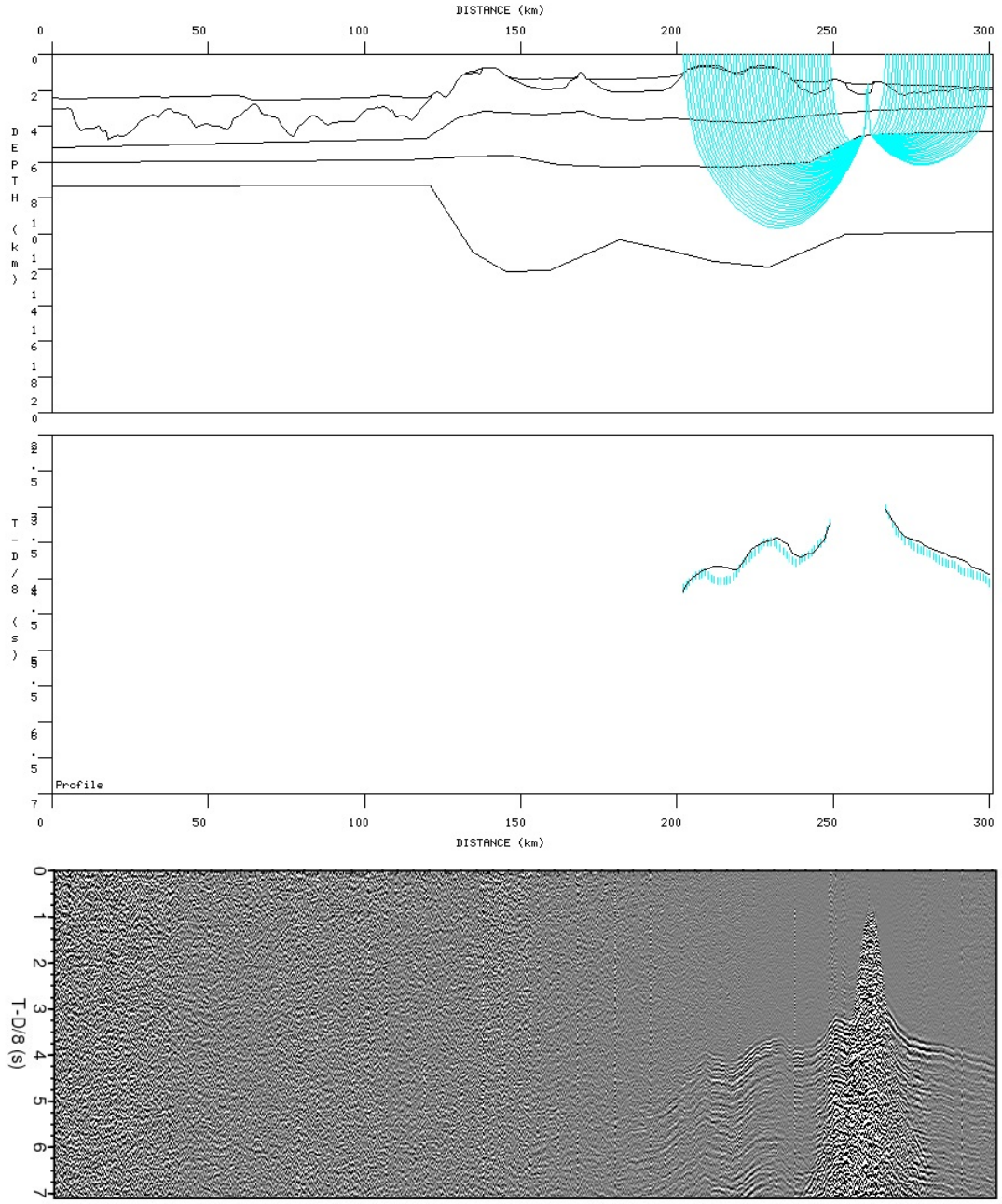

Figure B.20: Model 2: Picked PPS-wave phases and traced rays of OBS 1.

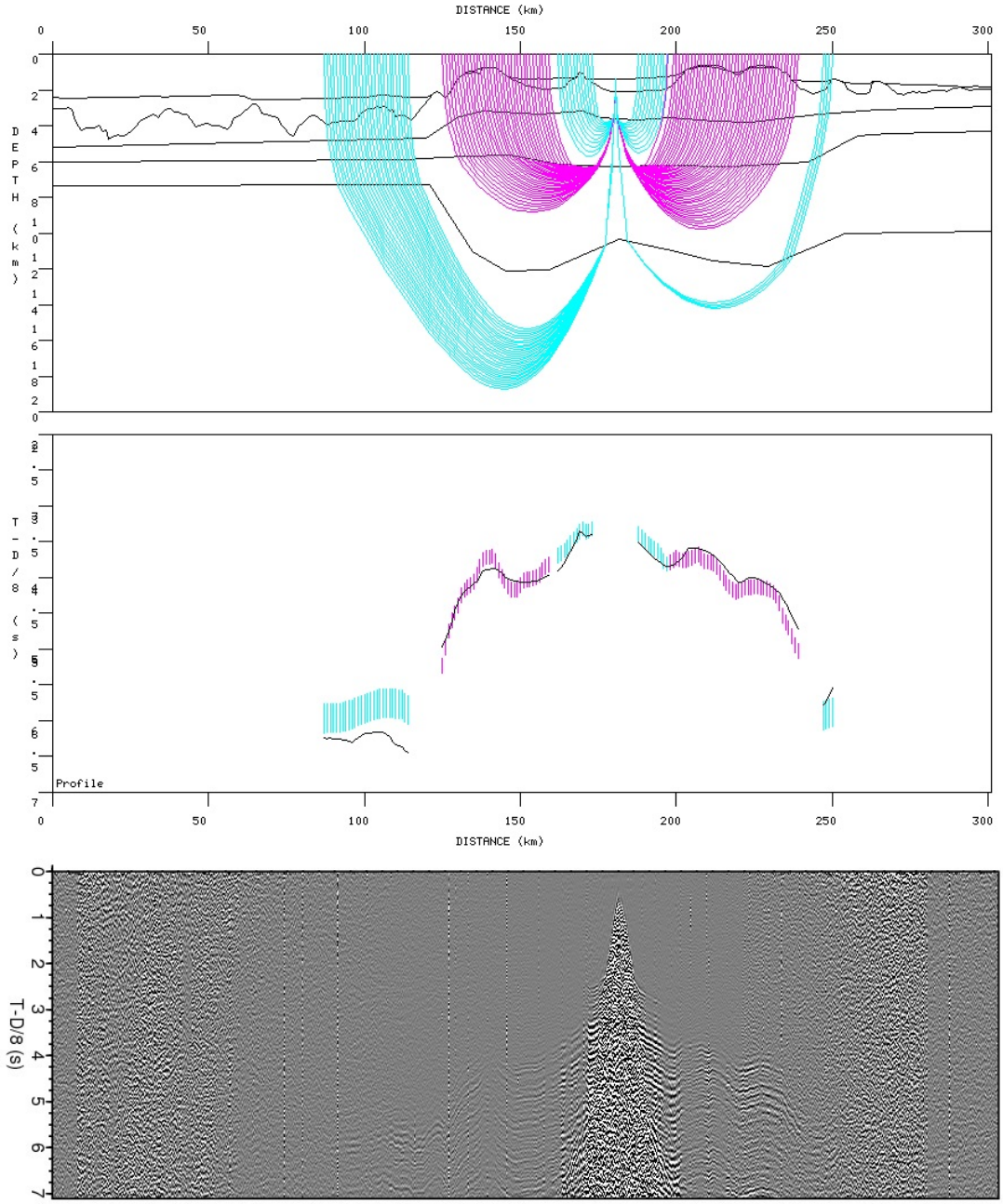

Figure B.21: Model 2: Picked PPS-wave phases and traced rays of OBS 3.

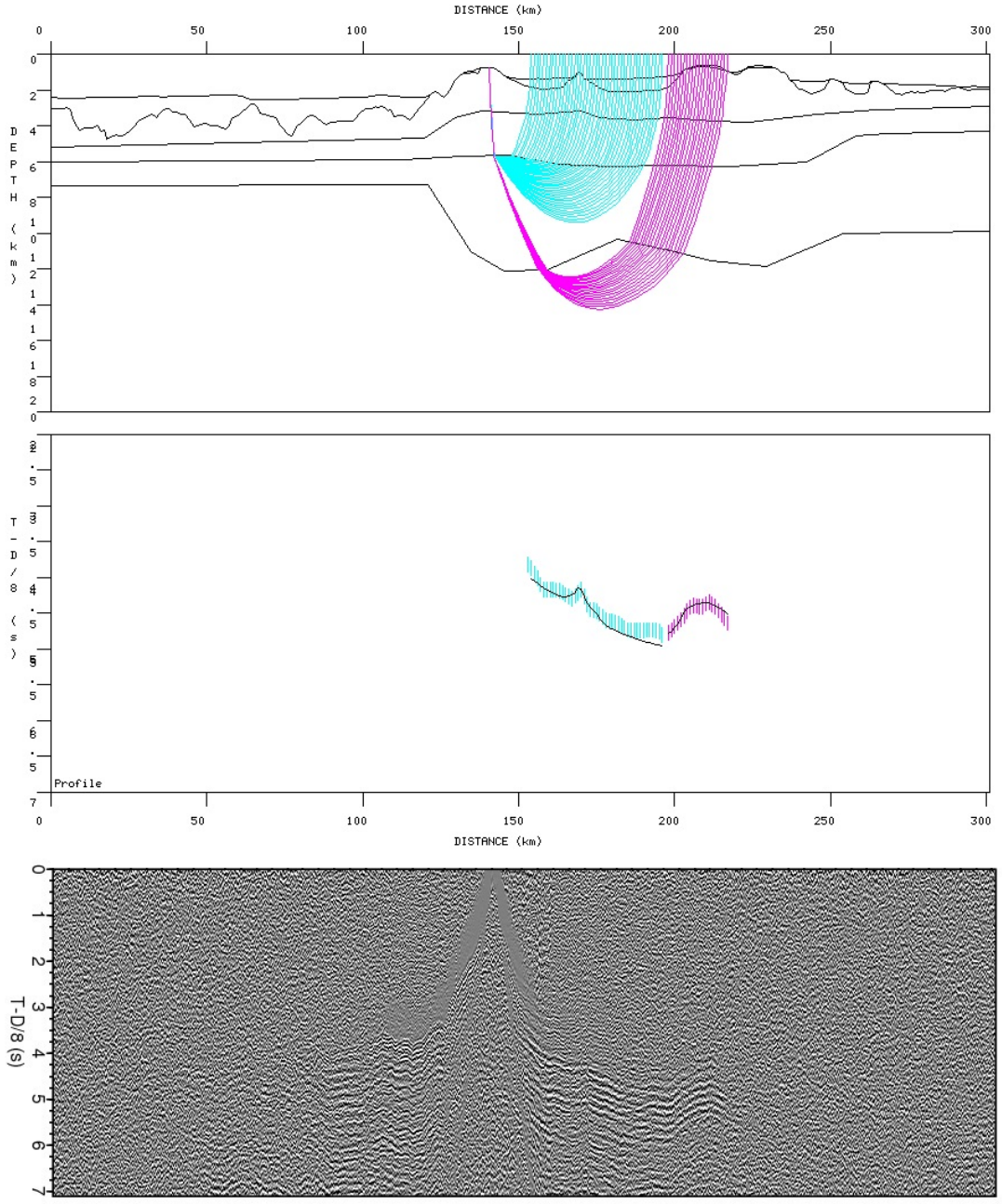

Figure B.22: Model 2: Picked PPS-wave phases and traced rays of OBS 4.